

Hardware-Tailored Diagonalization Circuits

Daniel Miller,^{*} Laurin E. Fischer, Igor O. Sokolov, Panagiotis Kl. Barkoutsos, and Ivano Tavernelli[†]
IBM Quantum, IBM Research Europe – Zurich, Säumerstrasse 4, CH-8803 Rüschlikon, Switzerland

A central building block of many quantum algorithms is the diagonalization of Pauli operators. Although it is always possible to construct a quantum circuit that simultaneously diagonalizes a given set of commuting Pauli operators, only resource-efficient circuits are reliably executable on near-term quantum computers. Generic diagonalization circuits can lead to an unaffordable SWAP-gate overhead on quantum devices with limited hardware connectivity. A common alternative is excluding two-qubit gates, however, this comes at the cost of restricting the class of diagonalizable sets of Pauli operators to tensor product bases (TPBs). In this Letter, we introduce a theoretical framework for constructing hardware-tailored (HT) diagonalization circuits. We apply our framework to group the Pauli operators occurring in the decomposition of a given Hamiltonian into jointly-HT-diagonalizable sets. We investigate several classes of popular Hamiltonians and observe that our approach requires a smaller number of measurements than conventional TPB approaches. Finally, we experimentally demonstrate the practical applicability of our technique, which showcases the great potential of our circuits for near-term quantum computing.

Introduction. Since first-generation quantum computers were made publicly available a few years ago, the technological frontier is expanding at an impressive pace. Nevertheless, decoherence and hardware errors still limit the applicability of these early-stage quantum devices, and practical quantum advantage yet remains to be demonstrated. To go beyond what is possible now, it is crucial to operate both classical and quantum computers in an orchestrated manner that exploits their respective strengths. For example, in the *variational quantum eigensolver* (VQE) algorithm [1–3], a classical computer optimizes the parameters of a trial quantum state $|\psi\rangle$ to find the minimal eigenvalue of an observable O , e.g., the Hamiltonian of a molecule. The tasks performed by the quantum processor are preparing $|\psi\rangle$ and gathering measurement data from which the expectation value $\langle O \rangle = \langle \psi | O | \psi \rangle$ can be estimated. In practice, O cannot be measured directly as this would require a quantum circuit that diagonalizes it, i.e., a circuit that rotates the unknown eigenbasis of O to the computational basis. A common approach to circumvent this problem is to express O as a linear combination of n -qubit Pauli operators $P_i \in \{I, X, Y, Z\}^{\otimes n}$ with real coefficients $c_i \in \mathbb{R}$, as in

$$O = \sum_{i=1}^M c_i P_i. \quad (1)$$

Since a given Pauli operator can be diagonalized using single-qubit Clifford gates, it is straightforward to individually measure its expectation value $\langle P_i \rangle$. Once all $\langle P_i \rangle$ are obtained, $\langle O \rangle$ is calculated from Eq. (1). Although the number M of Pauli operators for molecular Hamiltonians has a nominal scaling of up to $\mathcal{O}(n^4)$, measuring all Pauli expectation values individually would require a large number of quantum circuit executions (“shots”) [3].

To keep resource requirements minimal, one can make use of simultaneous measurements of commuting Pauli operators. For example, with a diagonalization circuit that only contains single-qubit gates, one can measure a *tensor product basis* (TPB), i.e., a set of Pauli operators that are *qubit-wise commuting* (QWC) [4]. For typical problems, it is possible to group an average number of three Pauli operators into a common TPB [5]. To further reduce the number of required diagonalization circuits from $\mathcal{O}(n^4)$ to $\mathcal{O}(n^3)$, grouping the Pauli operators into *general commuting* (GC) sets was suggested [6–8]. Under ideal circumstances, such GC groupings would significantly decrease the number of shots required to estimate $\langle O \rangle$ to a desired accuracy [9]. Unfortunately, the corresponding diagonalization circuits consist of up to $\frac{n(n-1)}{2}$ two-qubit gates and, if the connectivity of the device is limited, a large number of additional SWAP-gates. As a compromise, one can consider Pauli groupings with diagonalization circuits that feature a single layer of two-qubit gates [10, 11]. As of today, the best method to experimentally estimate an expectation value $\langle O \rangle$ is unclear. Besides Pauli grouping [4–13], there is active research in addressing this problem with classical shadows [14–17], unitary partitioning [18, 19], low-rank factorization [20], adaptive estimators [21–23], and decision diagrams [24].

In this Letter, we introduce a theoretical framework for constructing diagonalization circuits whose two-qubit gates are tailored to meet the connectivity restrictions imposed by most current quantum computing architectures, e.g., super- and semiconducting qubits [25–27]. Our flexible approach can be applied to any hardware connectivity. We demonstrate the viability of our techniques for a large class of paradigmatic Hamiltonians in the context of the Pauli grouping problem. Finally, we experimentally confirm the theoretically predicted advantage on IBM Quantum hardware [28].

Graph-Based Diagonalization Circuits. The purpose of our theoretical framework is the construction of HT Clifford circuits that diagonalize a given set of commut-

^{*} dmi@zurich.ibm.com

[†] ita@zurich.ibm.com

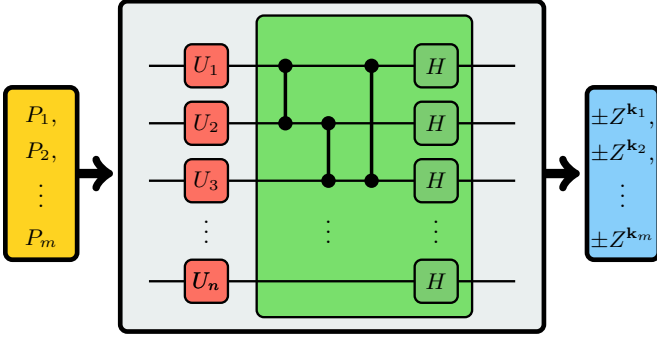


FIG. 1. Graph-based diagonalization circuit. A set of commuting Pauli operators P_1, \dots, P_m (yellow) is diagonalized in two steps: first, a layer of single-qubit Clifford gates $U = U_1 \otimes \dots \otimes U_n$ (red) rotates them into a set of the form $\mathcal{S} = \{\pm X^{\mathbf{k}} Z^{\Gamma \mathbf{k}} \mid \mathbf{k} \in \mathbb{F}_2^n\}$, where $\Gamma \in \mathbb{F}_2^{n \times n}$ is an adjacency matrix. Afterwards, \mathcal{S} is rotated to the computational basis (blue) by uncomputing the graph state $|\Gamma\rangle$ (green). The existence of U and Γ is guaranteed because every stabilizer state is LC-equivalent to a graph state [33]. We call a graph-based diagonalization circuit *hardware-tailored* if Γ is a subgraph of the connectivity graph of the considered quantum device.

ing n -qubit Pauli operators P_1, \dots, P_m . After possibly replacing some of the P_j by $-P_j$, we can assume that the group they generate, which is denoted by $\langle P_1, \dots, P_m \rangle$, does not contain $-I^{\otimes n}$. Then, it is possible to extend $\langle P_1, \dots, P_m \rangle$ to the *stabilizer group* \mathcal{S} of some *stabilizer state* $|\psi_{\mathcal{S}}\rangle$ (see the Supplementary Material (SM) for a constructive proof [29, I]), where $|\psi_{\mathcal{S}}\rangle$ is defined as the common $+1$ -eigenstate of all operators $S \in \mathcal{S}$ [30, 31]. Then, *uncomputing* the state $|\psi_{\mathcal{S}}\rangle$, i.e., applying some Clifford circuit $U_{\mathcal{S}}^{\dagger}$ with the property $|\psi_{\mathcal{S}}\rangle = U_{\mathcal{S}} |0\rangle^{\otimes n}$, will diagonalize P_1, \dots, P_m [31].

An important class of stabilizer states is the class of graph states [32]. A graph with n vertices is defined in terms of its *adjacency matrix* $\Gamma = (\gamma_{i,j}) \in \mathbb{F}_2^{n \times n}$, where \mathbb{F}_2 is the binary field; a pair (i, j) of vertices is connected via an edge if and only if $\gamma_{i,j} = 1$. In this Letter, we do not distinguish between a graph and its adjacency matrix, and we follow the convention $\gamma_{i,j} = \gamma_{j,i}$ and $\gamma_{i,i} = 0$ for all $i, j \in \{1, \dots, n\}$. Every graph Γ defines a *graph state* $|\Gamma\rangle = U_{\Gamma} |0\rangle^{\otimes n}$ whose preparation circuit

$$U_{\Gamma} = \left(\prod_{i < j} \text{CZ}_{i,j}^{\gamma_{i,j}} \right) H^{\otimes n} \quad (2)$$

consists of a layer of Hadamard gates, followed by one CZ-gate between every pair of connected vertices, where $H = \frac{1}{\sqrt{2}}(X+Z)$ and $\text{CZ} = \text{diag}(1, 1, 1, -1)$. The stabilizer group of $|\Gamma\rangle$ is $\mathcal{S}_{\Gamma} = \{X^{\mathbf{k}} Z^{\Gamma \mathbf{k}} (-1)^{\sum_{i < j} k_i \gamma_{i,j} k_j} \mid \mathbf{k} \in \mathbb{F}_2^n\}$, where $X^{\mathbf{k}} = X^{k_1} \otimes \dots \otimes X^{k_n}$ and similarly for Z [32]. Hence, U_{Γ}^{\dagger} would diagonalize our operators P_1, \dots, P_m if they were of the form $\pm X^{\mathbf{k}} Z^{\Gamma \mathbf{k}}$.

Every stabilizer state $|\psi_{\mathcal{S}}\rangle$ is local-Clifford (LC) equivalent to a graph state [33]. Thus, there exist single-qubit Clifford gates U_1, \dots, U_n and a graph Γ such that

TABLE I. Binary representation of the single-qubit Clifford group \mathcal{C}_1 . Every $U \in \mathcal{C}_1$ is a product of H and $S = \text{diag}(1, i)$. The six matrices $A \in GL(\mathbb{F}_2^2)$ isomorphically correspond to the permutations of $\{X, Y, Z\}$.

U	I	H	S	HSH	HS	SH
UXU^{\dagger}	X	Z	iXZ	X	$-iXZ$	Z
UZU^{\dagger}	Z	X	Z	$-iXZ$	X	iXZ
$\alpha(0, 1)$	0	0	0	3	0	1
$\alpha(1, 0)$	0	0	1	0	3	0
$A = \begin{bmatrix} a^{xx} & a^{xz} \\ a^{zx} & a^{zz} \end{bmatrix}$	$\begin{bmatrix} 1 & 0 \\ 0 & 1 \end{bmatrix}$	$\begin{bmatrix} 0 & 1 \\ 1 & 0 \end{bmatrix}$	$\begin{bmatrix} 1 & 0 \\ 1 & 1 \end{bmatrix}$	$\begin{bmatrix} 1 & 1 \\ 0 & 1 \end{bmatrix}$	$\begin{bmatrix} 1 & 1 \\ 1 & 0 \end{bmatrix}$	$\begin{bmatrix} 0 & 1 \\ 1 & 1 \end{bmatrix}$

$(U_1 \otimes \dots \otimes U_n) |\psi_{\mathcal{S}}\rangle = |\Gamma\rangle$. We conclude that every set of commuting Pauli operators can be simultaneously diagonalized by a layer of single-qubit Clifford gates followed by a circuit of the form U_{Γ}^{\dagger} . We refer to this procedure as a *graph-based diagonalization circuit* (see Fig. 1).

The *connectivity graph* Γ_{con} of a quantum computer is the graph whose vertices and edges, respectively, are given by the qubits and pairs of qubits for which a CZ-gate can be physically implemented. For quantum devices with a limited connectivity, general graph-based diagonalization circuits require up to $\mathcal{O}(n^2)$ SWAP-gates [34]. This overhead renders unconstrained graph-based diagonalization circuits infeasible for near-term applications. However, if $\Gamma \subset \Gamma_{\text{con}}$ is a subgraph of the connectivity graph, SWAP-gates are avoided completely. We refer to graph-based diagonalization circuits that are designed to meet this condition as *hardware-tailored* (HT).

Diagonalizability Criterion. We now derive a technical condition for the existence of graph-based diagonalization circuits. For this, we exploit the fact that every n -qubit Clifford gate U defines a symplectic matrix

$$A = \begin{bmatrix} A^{xx} & A^{xz} \\ A^{zx} & A^{zz} \end{bmatrix} \in GL(\mathbb{F}_2^{2n}) \quad (3)$$

with the property that

$$UX^{\mathbf{r}} Z^{\mathbf{s}} U^{\dagger} = i^{\alpha(\mathbf{r}, \mathbf{s})} X^{A^{xx} \mathbf{r} + A^{xz} \mathbf{s}} Z^{A^{zx} \mathbf{r} + A^{zz} \mathbf{s}} \quad (4)$$

holds for all vectors $\mathbf{r}, \mathbf{s} \in \mathbb{F}_2^n$ (see Tab. I for details of the single-qubit case [31]). Hereby, a matrix A is called *symplectic* if $A \begin{bmatrix} 0 & 1 \\ 1 & 0 \end{bmatrix} = \begin{bmatrix} 0 & 1 \\ 1 & 0 \end{bmatrix} A$, with $GL(\mathbb{F}_2^{2n})$ denoting the general linear group of \mathbb{F}_2^{2n} . For the time being, we can neglect the global phases given by $\alpha(\mathbf{r}, \mathbf{s}) \in \{0, 1, 2, 3\}$ and focus on the irreducible representation

$$\mathcal{C}_n \longrightarrow GL(\mathbb{F}_2^{2n}), \quad U \longmapsto A \quad (5)$$

of the n -qubit Clifford group \mathcal{C}_n . If $U = U_1 \otimes \dots \otimes U_n$ is a single-qubit Clifford-gate layer, the blocks in Eq. (3) are diagonal, i.e., $A^{xx} = \text{diag}(a_1^{xx}, \dots, a_n^{xx})$, and similarly for A^{xz} , A^{zx} , and A^{zz} . Hereby, a_1^{xx} is given by the xx -entry of the binary representation of U_1 , etc.

To construct a single-qubit Clifford-gate layer that rotates P_1, \dots, P_m into the set $\{\pm X^{\mathbf{k}} Z^{\Gamma \mathbf{k}}\}$ for a graph

Γ , we write $P_j = i^{q_j} X^{\mathbf{r}_j} Z^{\mathbf{s}_j}$. By Eq. (4), the application of U , which is represented by A , transforms the operator P_j into $P'_j = X^{\mathbf{k}_j} Z^{A^{zx}\mathbf{r}_j + A^{zz}\mathbf{s}_j}$, up to a global phase, where we have introduced the notation $\mathbf{k}_j = A^{xx}\mathbf{r}_j + A^{xz}\mathbf{s}_j$. Thus, $P'_j \in \{\pm X^{\mathbf{k}} Z^{\Gamma\mathbf{k}}\}$ is equivalent to $\Gamma\mathbf{k}_j = A^{zx}\mathbf{r}_j + A^{zz}\mathbf{s}_j$. These equivalent conditions can be phrased for all $j \in \{1, \dots, m\}$ simultaneously as a matrix equation

$$\Gamma A^{xx} R + \Gamma A^{xz} S = A^{zx} R + A^{zz} S, \quad (6)$$

where $R = (\mathbf{r}_1 \dots \mathbf{r}_m)$ and $S = (\mathbf{s}_1 \dots \mathbf{s}_m)$ are the two matrices that store the exponent vectors of P_1, \dots, P_m as their columns.

Constructing HT Circuits. We have reduced the task of constructing a HT graph-based diagonalization circuit to the problem of solving Eq. (6) for a subgraph $\Gamma \subset \Gamma_{\text{con}}$ and a symplectic, invertible matrix A whose blocks in Eq. (3) are diagonal. In our case, it is sufficient that A is invertible because every $A_i \in GL(\mathbb{F}_2^2)$, which represents U_i in $U = U_1 \otimes \dots \otimes U_n$, is necessarily also symplectic (see Tab. I). Because $a = 1$ is the only non-zero element $a \in \mathbb{F}_2$ and $\det(A) = \prod_{i=1}^n \det(A_i)$, the invertibility of A is equivalent to $\det(A_1) = \dots = \det(A_n) = 1$. These n quadratic constraints make solving Eq. (6) difficult.

For the case of a fixed graph Γ , we restate Eq. (6) as the feasibility problem of a *mixed integer quadratically constrained program* (MIQCP), which can be tackled by numerical optimizers. Furthermore, we devise an exact, algebraic solver that never fails to find a solution A if one exists; it does so by solving up to 6^k linear systems of size $4k \times d$ via Gaussian elimination over \mathbb{F}_2 , where both $4k$ and d are upper-bounded by $4n$. If no solution to Eq. (6) exists, an efficient test can sometimes verify this; in the worst case, our exact, algebraic solver has to pass through all 6^k iterations. If a solution does exist, it finishes after having found a solution to any such linear system, as this immediately yields a solution A (for details on our solvers for Eq. (6), see SM [29, II]).

By iterating through all 2^e subgraphs $\Gamma \subset \Gamma_{\text{con}}$, where $e \leq \binom{n}{2}$ is the number of edges in Γ_{con} , and applying our exact solver for Eq. (6), we can conclusively answer the question whether or not a graph-based diagonalization circuit for a given set of Pauli operators exists. Therefore, establishing *non-existence* has, in the worst case, runtime $f(n) = \mathcal{O}(2^e n^2 6^n)$, which is only feasible for small problem sizes. In practice, however, we are interested in the opposite case of constructively establishing the *existence* of graph-based diagonalization circuits. We find that the following efficient modification of our algorithm succeeds at this task with a sufficiently high probability: instead of iterating through all 2^e subgraphs, we restrict upfront to a polynomial number of subgraphs, e.g., to a random subset. Similarly, we replace our exact, algebraic solver by a restricted one that only probes a polynomial number of linear systems (see SM [29, II C]).

Pauli Groupings. Grouping the Pauli operators of an observable O into jointly-HT-diagonalizable subsets enables access to hardware-efficient building blocks for

quantum algorithms, e.g., *Hamiltonian exponentiation* (see SM [29, III]). In this Letter, we focus on *grouped Pauli measurements* (GPMs) which are more efficient than *individual Pauli measurements* (IPMs) [4–13]. To quantify this advantage, Crawford et al. [9] introduce a figure of merit, called \hat{R} , which approximates the difficulty to compute quantity $R = N_{\text{IPM}}^{\text{shots}} / N_{\text{GPM}}^{\text{shots}}$, where $N_{\text{IPM}}^{\text{shots}}$ is the total number of shots that IPMs would require to estimate $\langle O \rangle$ to a desired accuracy and similarly for $N_{\text{GPM}}^{\text{shots}}$. Furthermore, they show how the $N_{\text{GPM}}^{\text{shots}}$ shots should be distributed among the readout circuits to ensure optimal convergence (also see SM [29, IV]).

To implement our techniques for constructing HT circuits, we adapt the *Sorted Insertion* (SI) algorithm of Ref. [9], which constructs *Pauli groupings* (PGs) of the operators P_1, \dots, P_M in Eq. (1) with a near-optimal value of \hat{R} (for details, see SM [29, V]). Our modifications ensure that each subset, into which P_1, \dots, P_M are grouped, can be simultaneously diagonalized with a HT quantum circuit. While SI has a runtime of $\mathcal{O}(M^2 n)$, the runtime of our adaptation is given by $\mathcal{O}(M^2 f(n))$, where $f(n)$ is the complexity of the selected solver for Eq. (6), e.g., $f(n) = \mathcal{O}(2^e n^2 6^n)$ for the exact solver in the worst case. For our efficient solver, we empirically find $f(n) = \mathcal{O}(n^{2.5})$ whilst maintaining high-quality *hardware-tailored Pauli groupings* (HTPGs). As a benchmark, we compare our HTPGs with the PGs constructed by the SI-QWC algorithm. The latter arises verbatim from SI, except for replacing “commuting” with “QWC”. To our knowledge, there is no algorithm better than SI-QWC, which can be directly compared to our approach, for grouping P_1, \dots, P_M into TPBs [35].

We group the Pauli operators of randomly generated Hamiltonians into TPBs and jointly-HT-measurable sets by applying SI-QWC and our HTPG algorithm, respectively, and present the resulting values of $\hat{R}_{\text{HT}} / \hat{R}_{\text{TPB}}$ in Fig. 2. In all cases, we clearly observe $\hat{R}_{\text{HT}} / \hat{R}_{\text{TPB}} > 1$. Hence, our HTPGs outperform the hitherto best available PGs implementable in near-term quantum hardware. Notably, this advantage is amplified when the number M of Pauli operators is increased (see SM [29, VI A] for further elaborations on random Hamiltonians). To corroborate these results, we conduct an extensive investigation of HTPGs for the Hubbard model and for molecular Hamiltonians (see SM [29, VI]). In the non-trivial cases, we generally succeed in constructing HTPGs with $\hat{R}_{\text{HT}} / \hat{R}_{\text{TPB}} \gtrsim 2$. For small problem sizes, we can still apply the inefficient but exact algebraic solver, which yields HTPGs approximately maximizing \hat{R} . Although our efficient, restricted solvers fail to recognize some of the existing readout circuits, the abundance of HTPGs permits a remarkable reduction in the time needed to find a near-optimal HTPG. Computing a HTPG for which \hat{R} is as large as possible in the shortest amount of time is achievable by balancing the hyperparameters of our restricted solver. Executing this task is worthwhile because every constructed HTPG has vast reusability potential. For example, to map out a section of the energy surface

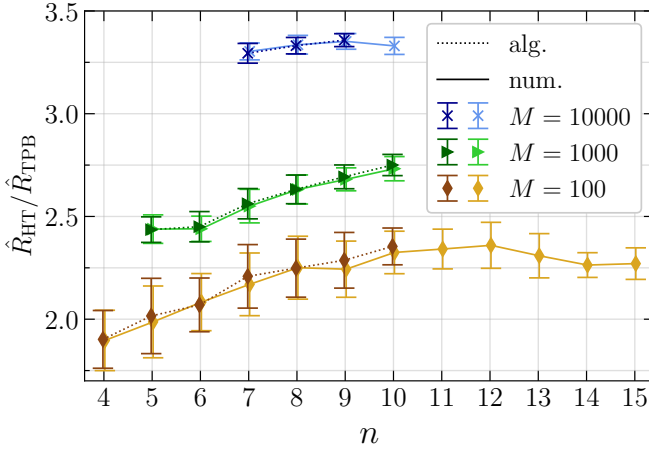


FIG. 2. Estimated shot reduction of hardware-tailored (HT) Pauli groupings over tensor product bases (TPB) for random Hamiltonians on n qubits with M different Pauli operators. Here, we tailor the readout circuits to a linear hardware connectivity by exploiting our exact, algebraic (alg.) and numerical (num.) solver, respectively, in combination with an exhaustive search over all circuit templates $\Gamma \subset \Gamma_{\text{linear}}$. Every data point is an average over twenty random Hamiltonians O as in Eq. (1), for each of which the coefficients $c_i \in [-1, 1]$ and Pauli operators $P_i \in \{I, X, Y, Z\}^{\otimes n}$ (excluding $I^{\otimes n}$) are sampled uniformly at random.

of a given molecule in the Born-Oppenheimer approximation via VQE, it is sufficient to precompute a single HTPG. Hereby, the continuous dependence of \hat{R} on the nuclear coordinates guarantees that the HTPG's quality does not deteriorate abruptly (see SM [29, VII]). Note that it is possible to scale up the construction of HTPGs to relevant problem sizes (see SM [29, VIII]).

Experimental Demonstration. The techniques introduced in this Letter are immediately applicable to today's state-of-the-art quantum computers. As a concrete example, we consider the electronic structure problem of a linear hydrogen chain with four sites, which is mapped to an eight-qubit Hamiltonian O . We group the corresponding $M = 184$ Pauli operators into $N_{\text{TPB}} = 35$ and $N_{\text{HT}} = 10$ jointly-HT-measurable sets by applying SI-QWC and our algorithm, respectively. Coincidentally, 2 HT sets coincide with 2 TPBs from SI-QWC, sharing the same readout circuits. To reveal the differences between TPB and HT, we therefore consider the observable O' that arises from O after removing the Pauli operators of the shared sets. For our experiment, we select a random, separable state $|\psi\rangle$ to maximally reduce preparation errors. We estimate the partial energy E'_{exp} for the experimental state and compute $\epsilon = |E'_{\text{exp}} - E'_{\text{theo}}|$, where $E'_{\text{theo}} = \langle \psi | O' | \psi \rangle \approx -28.6$ mHa. The error ϵ arises from shot noise due to a finite total number N^{shots} of circuit executions, in addition to a bias b stemming from noisy diagonalization circuits and qubit readouts. In the left panel of Fig. 3, we plot ϵ as a function of N^{shots} for both TPB (blue circles) and HT (green diamonds)

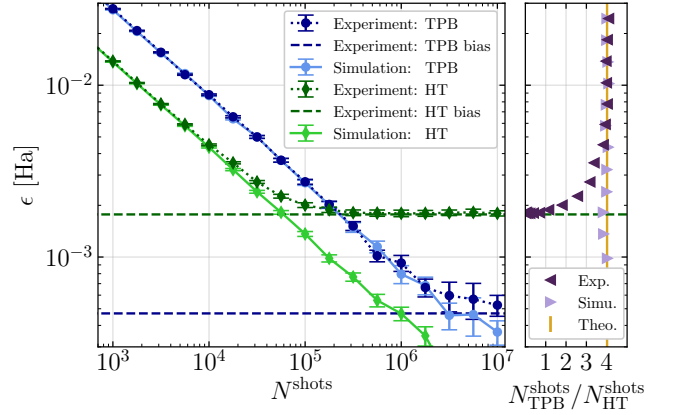


FIG. 3. The experimentally achieved shot reduction of hardware-tailored (HT) readout circuits over tensor product bases (TPBs) for measuring E' (see main text) up to an error of ϵ . The experiment is conducted with eight superconducting qubits on *ibm_washington* and compared to an ideal Qiskit simulation [36]. **(left)** Error $\epsilon = |E'_{\text{exp}} - E'_{\text{theo}}|$ as a function of the total number of optimally-allocated (see SM [29, IV]) circuit executions N^{shots} . Error bars show the error on the mean of ϵ averaged over $[5 \times 10^7 / N^{\text{shots}}]$ independent repetitions of the experiment. **(right)** The ratio $N^{\text{shots}}_{\text{TPB}} / N^{\text{shots}}_{\text{HT}}$ of shots needed to estimate E' up to ϵ . In an idealized setting, this ratio is independent of ϵ and given by $R_{\text{HT}} / R_{\text{TPB}} \approx 4.02$ [9].

and compare the experimental results (dark) to classical, noise-free simulations (bright). For a low shot budget, the experimental data agree with the simulation because sampling errors dominate. While the simulated errors generally decrease as $1/\sqrt{N^{\text{shots}}}$, the experimental errors eventually saturate at b . Unsurprisingly, $b_{\text{HT}} \approx 1.8$ mHa is larger than $b_{\text{TPB}} \approx 0.5$ mHa because HT readout circuits contain two-qubit gates, which are more noisy than single-qubit gates. Note that there exist practical use cases for which this is not an issue (see SM [29, IX]). The right panel of Fig. 3 features the corresponding shot reduction ratio $N^{\text{shots}}_{\text{TPB}} / N^{\text{shots}}_{\text{HT}}$ that can be achieved with the proposed HT readout circuits compared to conventional TPBs. For instance, to estimate E' with an accuracy of $\epsilon > 4$ mHa, our technique is four times more efficient than the hitherto best available Pauli grouping approach (for further details, see SM [29, X]).

Conclusion. In this Letter, we introduce a theoretical framework for the construction of diagonalization circuits that are tailored to any given hardware connectivity. We exploit the fact that every set of commuting Pauli operators can be cast into the stabilizer group of a stabilizer state which is local-Clifford equivalent to a graph state. The Pauli operators can thus be diagonalized with a quantum circuit that completely circumvents SWAP-gates whenever this graph state matches the connectivity of the quantum computer. We derive an algebraic criterion for the existence of such hardware-tailored diagonalization circuits and introduce solvers for their construction. An important empirical observation is that in many cases it

is not necessary to apply unconstrained diagonalization circuits because also hardware-tailored circuits exist.

Our contribution opens up new possibilities to alleviate limited device connectivities from which many quantum computing architectures suffer. We are confident that the tools developed in this Letter will find widespread application for the synthesis of hardware-tailored quantum circuits. As an exemplary use case, we apply our framework to the Pauli grouping problem for the optimization of readout processes, e.g., operator measurements in VQE experiments. For a broad selection of Hamiltonians that are relevant for quantum chemistry simulations, we observe that our approach can outperform the hitherto most promising near-term Pauli grouping techniques both in theory and experiment.

Acknowledgements. We are thankful to Libor Caha,

Kenny Jing Hui Choo, Felix Huber, Seyed Sajjad Nezhadi, Max Rossmannek, Maria Spethmann, David Sutter, Stefan Woerner, James Robin Wootton, and Nikolai Wyderka for stimulating discussions. This research is part of two projects that have received funding from the European Union’s Horizon 2020 research and innovation programme under the Marie Skłodowska-Curie grant agreements No. 847471 and No. 955479. This research was supported by the NCCR SPIN, funded by the Swiss National Science Foundation (SNF). I.O.S. acknowledges the financial support from the SNF through the grant No. 200021-179312. We acknowledge the use of IBM Quantum services for this work. The views expressed are those of the authors, and do not reflect the official policy or position of IBM or the IBM Quantum team.

-
- [1] A. Peruzzo, J. McClean, P. Shadbolt, M. Yung, X. Zhou, P. J. Love, A. Aspuru-Guzik, and J. L. O’Brien, A variational eigenvalue solver on a photonic quantum processor, *Nat. Commun.* **5** (2014).
 - [2] J. R. McClean, J. Romero, R. Babbush, and A. Aspuru-Guzik, The theory of variational hybrid quantum-classical algorithms, *New J. Phys.* **18** (2016).
 - [3] S. McArdle, S. Endo, A. Aspuru-Guzik, S. C. Benjamin, and X. Yuan, Quantum computational chemistry, *Rev. Mod. Phys.* **92**, 015003 (2020).
 - [4] A. Kandala, A. Mezzacapo, K. Temme, M. Takita, M. Brink, J. M. Chow, and J. M. Gambetta, Hardware-efficient variational quantum eigensolver for small molecules and quantum magnets, *Nature* **549**, 242 (2017).
 - [5] V. Verteletskyi, T.-C. Yen, and A. F. Izmaylov, Measurement optimization in the variational quantum eigensolver using a minimum clique cover, *J. Chem. Phys.* **152** (2020).
 - [6] P. Gokhale, O. Angiuli, Y. Ding, K. Gui, T. Tomesh, M. Suchara, M. Martonosi, and F. T. Chong, $O(N^3)$ Measurement Cost for Variational Quantum Eigensolver on Molecular Hamiltonians, *IEEE Trans. Quantum Eng.* **1**, 1 (2020).
 - [7] T.-C. Yen, V. Verteletskyi, and A. F. Izmaylov, Measuring All Compatible Operators in One Series of Single-Qubit Measurements Using Unitary Transformations, *J. Chem. Theory Comput.* **16**, 2400 (2020).
 - [8] A. Jena, S. Genin, and M. Mosca, Pauli Partitioning with Respect to Gate Sets, [arXiv:1907.07859 \[quant-ph\]](https://arxiv.org/abs/1907.07859) (2019).
 - [9] O. Crawford, B. v. Straaten, D. Wang, T. Parks, E. Campbell, and S. Brierley, Efficient quantum measurement of Pauli operators in the presence of finite sampling error, *Quantum* **5**, 385 (2021).
 - [10] I. Hamamura and T. Imamichi, Efficient evaluation of quantum observables using entangled measurements, *npj Quantum Inf.* **6** (2019).
 - [11] F. Escudero, D. Fernández-Fernández, G. Jaumà, G. F. Peñas, and L. Pereira, Hardware-efficient entangled measurements for variational quantum algorithms, [arXiv:2202.06979 \[quant-ph\]](https://arxiv.org/abs/2202.06979) (2022).
 - [12] B. Wu, J. Sun, Q. Huang, and X. Yuan, Overlapped grouping measurement: A unified framework for measuring quantum states, [arXiv:2105.13091 \[quant-ph\]](https://arxiv.org/abs/2105.13091) (2021).
 - [13] T.-C. Yen, A. Ganeshram, and A. F. Izmaylov, Deterministic improvements of quantum measurements with grouping of compatible operators, non-local transformations, and covariance estimates, [arXiv:2201.01471 \[quant-ph\]](https://arxiv.org/abs/2201.01471) (2022).
 - [14] H.-Y. Huang, R. Kueng, and J. Preskill, Predicting many properties of a quantum system from very few measurements, *Nat. Phys.* **16**, 1050 (2020).
 - [15] C. Hadfield, S. Bravyi, R. Raymond, and A. Mezzacapo, Measurements of Quantum Hamiltonians with Locally-Biased Classical Shadows, *Comm. Math. Phys.* **391**, 951 (2022).
 - [16] H.-Y. Huang, R. Kueng, and J. Preskill, Efficient Estimation of Pauli Observables by Derandomization, *Phys. Rev. Lett.* **127**, 030503 (2021).
 - [17] C. Hadfield, Adaptive Pauli Shadows for Energy Estimation, [arXiv:2105.12207 \[quant-ph\]](https://arxiv.org/abs/2105.12207) (2021).
 - [18] A. F. Izmaylov, T.-C. Yen, R. A. Lang, and V. Verteletskyi, Unitary Partitioning Approach to the Measurement Problem in the Variational Quantum Eigensolver Method, *J. Chem. Theory Comput.* **16**, 190 (2020).
 - [19] A. Zhao, A. Tranter, W. M. Kirby, S. F. Ung, A. Miyake, and P. J. Love, Measurement reduction in variational quantum algorithms, *Phys. Rev. A* **101**, 062322 (2020).
 - [20] W. J. Huggins, J. R. McClean, N. C. Rubin, Z. Jiang, N. Wiebe, K. B. Whaley, and R. Babbush, Efficient and noise resilient measurements for quantum chemistry on near-term quantum computers, *npj Quantum Inf.* **7** (2021).
 - [21] G. García-Pérez, M. A. Rossi, B. Sokolov, F. Tacchino, P. K. Barkoutsos, G. Mazzola, I. Tavernelli, and S. Maniscalco, Learning to Measure: Adaptive Informationally Complete Generalized Measurements for Quantum Algorithms, *PRX Quantum* **2**, 040342 (2021).
 - [22] A. Shlosberg, A. J. Jena, P. Mukhopadhyay, J. F. Haase, F. Leditzky, and L. Dellantonio, Adaptive estimation of quantum observables, [arXiv:2110.15339 \[quant-ph\]](https://arxiv.org/abs/2110.15339) (2021).
 - [23] L. E. Fischer, D. Miller, F. Tacchino, P. K. Barkoutsos,

- D. J. Egger, and I. Tavernelli, Ancilla-free implementation of generalized measurements for qubits embedded in a qudit space, *Phys. Rev. Research* **4**, 033027 (2022).
- [24] S. Hillmich, C. Hadfield, R. Raymond, A. Mezzacapo, and R. Wille, Decision Diagrams for Quantum Measurements with Shallow Circuits, *IEEE Transactions on Quantum Engineering* **2**, 24 (2021).
- [25] A. Sigillito, J. Loy, D. Zajac, M. Gullans, L. Edge, and J. Petta, Site-Selective Quantum Control in an Isotopically Enriched $^{28}\text{Si}/\text{Si}_{0.7}\text{Ge}_{0.3}$ Quadruple Quantum Dot, *Phys. Rev. Applied* **11**, 061006 (2019).
- [26] C. Chamberland, G. Zhu, T. J. Yoder, J. B. Hertzberg, and A. W. Cross, Topological and Subsystem Codes on Low-Degree Graphs with Flag Qubits, *Phys. Rev. X* **10**, 011022 (2020).
- [27] C. K. Andersen, A. Remm, S. Lazar, S. Krinner, N. Lacroix, G. J. Norris, M. Gabureac, C. Eichler, and A. Wallraff, Repeated quantum error detection in a surface code, *Nat. Phys.* **16**, 875 (2020).
- [28] IBM, the IBM logo, and ibm.com are trademarks of International Business Machines Corp., registered in many jurisdictions worldwide. Other product and service names might be trademarks of IBM or other companies. The current list of IBM trademarks is available at <https://www.ibm.com/legal/copytrade>.
- [29] See Supplemental Material for details on the theoretical derivations, experimental results, and further findings supporting the main results.
- [30] D. Gottesman, *Stabilizer Codes and Quantum Error Correction* (1997).
- [31] J. Dehaene and B. De Moor, Clifford group, stabilizer states, and linear and quadratic operations over $\text{GF}(2)$, *Phys. Rev. A* **68**, 042318 (2003).
- [32] M. Hein, J. Eisert, and H. J. Briegel, Multiparty entanglement in graph states, *Phys. Rev. A* **69**, 062311 (2004).
- [33] M. Van den Nest, J. Dehaene, and B. De Moor, Graphical description of the action of local Clifford transformations on graph states, *Phys. Rev. A* **69**, 022316 (2004).
- [34] D. Maslov, Linear depth stabilizer and quantum fourier transformation circuits with no auxiliary qubits in finite-neighbor quantum architectures, *Phys. Rev. A* **76**, 052310 (2007).
- [35] Recently, Pauli grouping algorithms that dedicate exactly one readout circuit to every operator, e.g., SI-QWC, have been outperformed by exploiting the fact that some of the Pauli operators can be measured with more than one of the available readout circuits [13]. In this work, we compare our results with SI-QWC because our approach is complementary to that of Ref. [13] and we expect that it is possible to combine both of them.
- [36] *Qiskit: An Open-source Framework for Quantum Computing* (2021).
- [37] D. A. Lidar and T. A. Brun, *Quantum Error Correction* (Cambridge University Press, 2013).
- [38] C. H. Bennett, G. Brassard, C. Crépeau, R. Jozsa, A. Peres, and W. K. Wootters, Teleporting an unknown quantum state via dual classical and Einstein-Podolsky-Rosen channels, *Phys. Rev. Lett.* **70**, 1895 (1993).
- [39] F. Huber and S. Severini, Some Ulam’s reconstruction problems for quantum states, *J. Phys. A Math. Theor.* **51**, 435301 (2018).
- [40] D. Miller, D. Loss, I. Tavernelli, H. Kampermann, D. Bruß, and N. Wyderka, Sector length distributions of graph states, [arXiv:2207.07665 \[quant-ph\]](https://arxiv.org/abs/2207.07665) (2022).
- [41] D. Cox, J. Little, and D. O’Shea, *Ideals, varieties, and algorithms: an introduction to computational algebraic geometry and commutative algebra* (Springer Science & Business Media, 2013).
- [42] D. C. McKay, C. J. Wood, S. Sheldon, J. M. Chow, and J. M. Gambetta, Efficient Z gates for quantum computing, *Phys. Rev. A* **96**, 022330 (2017).
- [43] M. A. Nielsen and I. L. Chuang, *Quantum Computation and Quantum Information* (Cambridge University Press, 2000).
- [44] H. F. Trotter, On the product of semi-groups of operators, *Proc. Amer. Math. Soc.* **10**, 545 (1959).
- [45] J. M. Kübler, A. Arrasmith, L. Cincio, and P. J. Coles, An adaptive optimizer for measurement-frugal variational algorithms, *Quantum* **4**, 263 (2020).
- [46] R. Sweke, F. Wilde, J. Meyer, M. Schuld, P. K. Faehrmann, B. Meynard-Piganeau, and J. Eisert, Stochastic gradient descent for hybrid quantum-classical optimization, *Quantum* **4**, 314 (2020).
- [47] A. Arrasmith, L. Cincio, R. D. Somma, and P. J. Coles, Operator sampling for shot-frugal optimization in variational algorithms, [arXiv preprint arXiv:2004.06252](https://arxiv.org/abs/2004.06252) (2020).
- [48] N. C. Rubin, R. Babbush, and J. McClean, Application of fermionic marginal constraints to hybrid quantum algorithms, *New J. Phys.* **20**, 053020 (2018).
- [49] D. Wecker, M. B. Hastings, and M. Troyer, Progress towards practical quantum variational algorithms, *Phys. Rev. A* **92**, 042303 (2015).
- [50] A. Heckel, The chromatic number of dense random graphs, *Random Struct. Algorithms* **53**, 140 (2018).
- [51] P.-L. Dallaire-Demers, M. Stechly, J. F. Gonthier, N. T. Bashige, J. Romero, and Y. Cao, An application benchmark for fermionic quantum simulations, [arXiv:2003.01862 \[quant-ph\]](https://arxiv.org/abs/2003.01862) (2021).
- [52] B. T. Gard and A. M. Meier, Classically efficient quantum scalable Fermi-Hubbard benchmark, *Phys. Rev. A* **105**, 042602 (2022).
- [53] F. H. L. Essler, H. Frahm, F. Göhmann, A. Klümper, and V. E. Korepin, *The One-Dimensional Hubbard Model* (Cambridge University Press, 2005).
- [54] C. Cade, L. Mineh, A. Montanaro, and S. Stanisic, Strategies for solving the Fermi-Hubbard model on near-term quantum computers, *Phys. Rev. B* **102**, 235122 (2020).
- [55] E. van den Berg and K. Temme, Circuit optimization of Hamiltonian simulation by simultaneous diagonalization of Pauli clusters, *Quantum* **4**, 322 (2020).
- [56] W. Dobrutz, H. Luo, and A. Alavi, Compact numerical solutions to the two-dimensional repulsive Hubbard model obtained via nonunitary similarity transformations, *Phys. Rev. B* **99**, 075119 (2019).
- [57] S. McArdle and D. P. Tew, Improving the accuracy of quantum computational chemistry using the transcorrelated method, [arXiv:2006.11181 \[quant-ph\]](https://arxiv.org/abs/2006.11181) (2020).
- [58] I. O. Sokolov, W. Dobrutz, H. Luo, A. Alavi, and I. Tavernelli, Orders of magnitude reduction in the computational overhead for quantum many-body problems on quantum computers via an exact transcorrelated method, [arXiv:2201.03049 \[quant-ph\]](https://arxiv.org/abs/2201.03049) (2022).
- [59] Q. Sun, T. C. Berkelbach, N. S. Blunt, G. H. Booth, S. Guo, Z. Li, J. Liu, J. D. McClain, E. R. Sayfutyarova, S. Sharma, S. Wouters, and G. K.-L. Chan, PySCF: the Python-based simulations of chemistry framework, *Wiley*

- Interd. Rev.: Comput. Mol. Sci.* **8**, e1340 (2018).
- [60] S. B. Bravyi and A. Y. Kitaev, Fermionic Quantum Computation, *Ann. Phys. (N. Y.)* **298**, 210 (2002).
 - [61] N. Moll, A. Fuhrer, P. Staar, and I. Tavernelli, Optimizing qubit resources for quantum chemistry simulations in second quantization on a quantum computer, *J. Phys. A* **49**, 295301 (2016).
 - [62] S. Bravyi, J. M. Gambetta, A. Mezzacapo, and K. Temme, Tapering off qubits to simulate fermionic Hamiltonians, *arXiv:1701.08213 [quant-ph]* (2017).
 - [63] K. Setia and J. D. Whitfield, Bravyi-Kitaev Superfast simulation of electronic structure on a quantum computer, *J. Chem. Phys.* **148**, 164104 (2018), 1712.00446.
 - [64] M. Miller and D. Miller, GraphStateVis: Interactive Visual Analysis of Qubit Graph States and their Stabilizer Groups, *IEEE Trans. Quantum Eng.* **1**, 378 (2021).
 - [65] M. Motta, C. Genovese, F. Ma, Z.-H. Cui, R. Sawaya, G. K.-L. Chan, N. Chepiga, P. Helms, C. Jiménez-Hoyos, A. J. Millis, U. Ray, E. Ronca, H. Shi, S. Sorella, E. M. Stoudenmire, S. R. White, and S. Zhang (Simons Collaboration on the Many-Electron Problem), Ground-State Properties of the Hydrogen Chain: Dimerization, Insulator-to-Metal Transition, and Magnetic Phases, *Phys. Rev. X* **10**, 031058 (2020).
 - [66] M. Motta, D. M. Ceperley, G. K.-L. Chan, J. A. Gomez, E. Gull, S. Guo, C. A. Jiménez-Hoyos, T. N. Lan, J. Li, F. Ma, A. J. Millis, N. V. Prokof'ev, U. Ray, G. E. Scuseria, S. Sorella, E. M. Stoudenmire, Q. Sun, I. S. Tupitsyn, S. R. White, D. Zgid, and S. Zhang (Simons Collaboration on the Many-Electron Problem), Towards the Solution of the Many-Electron Problem in Real Materials: Equation of State of the Hydrogen Chain with State-of-the-Art Many-Body Methods, *Phys. Rev. X* **7**, 031059 (2017).
 - [67] R. Muller, *Pyquante: Python quantum chemistry* (accessed 25 February 2022).
 - [68] W. Kirby, B. Fuller, C. Hadfield, and A. Mezzacapo, Second-Quantized Fermionic Operators with Polylogarithmic Qubit and Gate Complexity, *PRX Quantum* **3**, 020351 (2022).
 - [69] K. Temme, S. Bravyi, and J. M. Gambetta, Error mitigation for short-depth quantum circuits, *Phys. Rev. Lett.* **119**, 180509 (2017).
 - [70] S. Bravyi, S. Sheldon, A. Kandala, D. C. McKay, and J. M. Gambetta, Mitigating measurement errors in multiqubit experiments, *Phys. Rev. A* **103**, 042605 (2021).
 - [71] P. D. Nation, H. Kang, N. Sundaresan, and J. M. Gambetta, Scalable mitigation of measurement errors on quantum computers, *PRX Quantum* **2**, 040326 (2021).

Supplemental Material

CONTENTS

I. Completing a Stabilizer Group	9
II. Constructing Hardware-Tailored Diagonalization Circuits	10
A. Geometric Description of the Solution Space	10
B. Algebraic Description of the Solution Space	10
C. Cutoff for Restricting the Search Space	12
D. Numerical Optimization	14
E. Further Insights and Open Problems	14
III. Hardware-Tailored Hamiltonian Exponentiation	15
IV. Optimally Allocating Shots to Readout Circuits	16
V. Pauli Grouping Algorithms	17
VI. Examples of Hardware-Tailored Pauli Groupings	19
A. Random Hamiltonians	19
B. One-Dimensional Hubbard Model	22
C. Selected Molecules	26
D. Hydrogen Chains	27
VII. Reusability of Pauli Groupings	28
VIII. Pre-Processing Time VS. Runtime Savings for a 52-Qubit Example	30
IX. Anticipated Use Cases	32
X. Details about the Experiment	33

I. COMPLETING A STABILIZER GROUP

In this section, we explain how to extend a set of m commuting Pauli operators $P_1, \dots, P_m \in \{I, X, Y, Z\}^{\otimes n}$ to a stabilizer group \mathcal{S} of a stabilizer state $|\psi_{\mathcal{S}}\rangle$. Our method is an alternative to a well-known approach based on the Gram-Schmidt procedure [37]. We use our subroutine to apply the algorithm in Ref. [6] for computing general diagonalization circuits. Every Pauli operator is of the form $P_i = i^{q_i} X^{\mathbf{r}^{(i)}} Z^{\mathbf{s}^{(i)}}$ with $q_i \in \{0, 1, 2, 3\}$ and $\mathbf{r}^{(i)}, \mathbf{s}^{(i)} \in \mathbb{F}_2^n$. Since the stabilizer group \mathcal{S} must not contain $-I^{\otimes n}$, some of the operators P_i may have to be replaced by $-P_i$. This does not interfere with our goal because we are only interested in the phase-free part, which is given by the matrix

$$\begin{bmatrix} R \\ S \end{bmatrix} = \begin{bmatrix} \mathbf{r}^{(1)} & \dots & \mathbf{r}^{(m)} \\ \mathbf{s}^{(1)} & \dots & \mathbf{s}^{(m)} \end{bmatrix} \in \mathbb{F}_2^{2n \times m}. \quad (7)$$

Using Gaussian elimination over \mathbb{F}_2 it is straightforward to find a matrix of row-operations $M \in \mathbb{F}_2^{2n \times 2n}$ such that

$$B = M \begin{bmatrix} R \\ S \end{bmatrix} \quad (8)$$

is the reduced-row echelon form of the matrix in Eq. (7). By deleting all non-pivot columns of B , we can assume without loss of generality that the operators P_1, \dots, P_m are independent, i.e.,

$$B = \begin{bmatrix} \mathbb{1}_m \\ 0 \end{bmatrix} \in \mathbb{F}_2^{2n \times m}. \quad (9)$$

The intricate part of completing these operators to \mathcal{S} is to find an operator $P_{m+1} \in \{I, X, Y, Z\}^{\otimes n}$ that simultaneously is independent from and commuting with all previous operators. By the symplectic nature of the Pauli group, an operator $X^{\mathbf{j}} Z^{\mathbf{k}}$ commutes with P_1, \dots, P_m if and only if (iff)

$$\begin{bmatrix} R \\ S \end{bmatrix}^T \begin{bmatrix} 0 & \mathbb{1}_n \\ \mathbb{1}_n & 0 \end{bmatrix} \begin{bmatrix} \mathbf{j} \\ \mathbf{k} \end{bmatrix} = 0, \quad (10)$$

i.e., iff $(\mathbf{j}, \mathbf{k}) \in \ker([S^T, R^T])$ [31]. Furthermore, $X^{\mathbf{j}} Z^{\mathbf{k}}$ is independent from P_1, \dots, P_m iff appending the vector $(\mathbf{j}, \mathbf{k})^T$ as a final column to the matrix in Eq. (7) increases the rank by one. By comparing to Eq. (9), we find that this is the case iff the vector $\mathbf{v} = M(\mathbf{j}, \mathbf{k})^T$ fulfills $v_i = 1$ for at least one index $i > m$. Therefore, the set of binary vectors that are independent of $(\mathbf{r}^{(1)}, \mathbf{s}^{(1)}), \dots, (\mathbf{r}^{(m)}, \mathbf{s}^{(m)})$ is given by $M^{-1}\mathcal{L}$, where

$$\mathcal{L} = \{\mathbf{v} \in \mathbb{F}_2^{2n} \mid \exists i > m : v_i = 1\}. \quad (11)$$

Combining both properties, we need to find a vector in the intersection

$$\begin{aligned} & \ker([S^T, R^T]) \cap M^{-1}\mathcal{L} \\ &= M^{-1}(\ker([S^T, R^T]M^{-1}) \cap \mathcal{L}). \end{aligned} \quad (12)$$

To achieve this, we first apply Gaussian elimination to compute a basis $\mathbf{v}^{(1)}, \dots, \mathbf{v}^{(2n-m)} \in \mathbb{F}_2^{2n}$ of the matrix

$$\begin{bmatrix} S \\ R \end{bmatrix}^T M^{-1} \in \mathbb{F}_2^{m \times 2n}. \quad (13)$$

Next, we select a vector $\mathbf{v}^{(i)}$ with $v_j^{(i)} = 1$ for at least one index $j > m$ (which exists because of $m < n$). In particular, we have $\mathbf{v}^{(i)} \in \ker([S^T, R^T]M^{-1}) \cap \mathcal{L}$ and Eq. (12) shows that $P_{m+1} = \pm X^{\mathbf{r}^{(m+1)}} Z^{\mathbf{s}^{(m+1)}}$ with

$$\begin{bmatrix} \mathbf{r}^{(m+1)} \\ \mathbf{s}^{(m+1)} \end{bmatrix} = M^{-1}\mathbf{v}^{(i)} \quad (14)$$

extends the set $\{P_1, \dots, P_m\}$ in the desired way. We can repeat all these steps until we finally reach $m = n$.

II. CONSTRUCTING HARDWARE-TAILORED DIAGONALIZATION CIRCUITS

In this section, we develop the mathematical backbone of our theoretical framework. We introduce techniques for constructing the layer of single-qubit Clifford gates in a hardware-tailored (HT) graph-based diagonalization circuit (see main text, Fig. 1). In Sec. II A, we illustrate the geometric nature of the solution space to Eq. (6) from the main text. The corresponding algebraic formulae are explicitly stated in Sec. II B. In Sec. II C, we introduce a cutoff that enables us to efficiently examine a restricted section of the full solution space. As we show in Sec. II D, Eq. (6) can be restated as the feasibility problem of a mixed integer quadratically constrained program. Finally, we provide practical insights and ideas for further improvements in Sec. II E.

A. Geometric Description of the Solution Space

Equation (6) is linear in A and, for a fixed graph Γ , a basis of the solution vector space is readily available via Gaussian elimination over the binary field \mathbb{F}_2 . A solution A , however, only corresponds to a layer of single-qubit Clifford gates U , if it is non-singular, i.e., if $\det(A) \neq 0$. This condition is equivalent to $\prod_{i=1}^n \det(A_i) = 1$, where $A_i \in GL(\mathbb{F}_2^2)$ represents the i -th single-qubit gate in $U = U_1 \otimes \dots \otimes U_n$. As we will show in Sec. II B, these determinants can be written as quadratic forms

$$\det(A_i) = \lambda^T Q_i \lambda, \quad (15)$$

where $\lambda \in \mathbb{F}_2^d$ is parameterizing the aforementioned linear solution space of Eq. (6), which has dimension $d \leq 4n$. Geometrically, $\lambda^T Q_i \lambda = 1$ defines a quadric hypersurface $\mathcal{L}_i \subset \mathbb{F}_2^d$. As a consequence, the final solution space, which is defined by $\det(A_1) = \dots = \det(A_n) = 1$, is the intersection $\mathcal{L} = \bigcap_{i=1}^n \mathcal{L}_i$. The points of \mathcal{L} are in one-to-one correspondence with the single-qubit Clifford-gate layers that transform the Pauli operators P_1, \dots, P_m into stabilizer operators of the graph state $|\Gamma\rangle$ (up to a global phase). In particular, \mathcal{L} is non-empty if and only if it is possible to diagonalize P_1, \dots, P_m with a circuit based on Γ (see main text, Fig. 1). Cases with $\mathcal{L} = \emptyset$ do exist, e.g., there is no single-qubit-gate layer $U_1 \otimes U_2$ for which $P = X \otimes I$ becomes diagonal after the application of a graph-based circuit that involves exactly one CZ-gate.

If $Q_i = 0$ for one of the qubits $i \in \{1, \dots, n\}$, we can immediately conclude that \mathcal{L} is empty. Another important special case is $\text{rank}_{\mathbb{F}_2}(Q_i) = 1$, in which a convenient coincidence (see Sec. II B) leads to \mathcal{L}_i being an affine subspace; a case we can efficiently deal with. In general, however, we have $\text{rank}_{\mathbb{F}_2}(Q_i) = 2$, and the quadric hypersurface \mathcal{L}_i happens to be a union of four affine subspaces, whose number we denote by $k \leq n$. The intersection of the other $n - k$ affine spaces with $\text{rank}_{\mathbb{F}_2}(Q_i) = 1$ is again just an affine subspace. The intersection of the k spaces

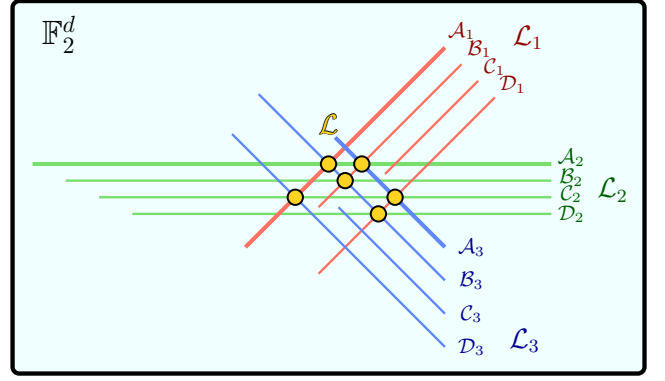


FIG. 4. Illustration of the solution space \mathcal{L} (yellow dots) of Eq. (6) for a hypothetical scenario with $n = 3$ qubits. In this example, \mathcal{L} is the intersection of $k = 3$ quadric hypersurfaces \mathcal{L}_1 (red), \mathcal{L}_2 (green), and \mathcal{L}_3 (blue). Every hypersurface \mathcal{L}_i is the union of the four affine subspaces \mathcal{A}_i , \mathcal{B}_i , \mathcal{C}_i , and \mathcal{D}_i (parallel lines) defined in Eqs. (29)–(32).

\mathcal{L}_i with $\text{rank}_{\mathbb{F}_2}(Q_i) = 2$, however, is the union of 4^k affine subspaces. Therefore, $\mathcal{L} = \bigcap_i \mathcal{L}_i$ is also a union over 4^k (potentially smaller) affine subspaces (see Fig. 4 for an illustration). If we do not want to miss out on any point in \mathcal{L} , we would thus have to probe an exponentially large number of subspaces.

B. Algebraic Description of the Solution Space

For the sake of clarity, we have omitted most of the technical details in the previous subsection. To solve Eq. (6) in practice, we now bring $\det(A) = 1$ into a form a classical computer can deal with. First, we exploit the fact that the blocks of A as in Eq. (3) are diagonal in our case. Thus, we can replace A by the vector

$$\mathbf{a} = \begin{bmatrix} \mathbf{a}^{xx} \\ \mathbf{a}^{xz} \\ \mathbf{a}^{zx} \\ \mathbf{a}^{zz} \end{bmatrix} \in \mathbb{F}_2^{4n} \quad (16)$$

where the vector $\mathbf{a}^{xx} = (a_1^{xx}, \dots, a_n^{xx}) \in \mathbb{F}_2^n$ defines the xx -block via $A^{xx} = \text{diag}(\mathbf{a}^{xx})$, and likewise for \mathbf{a}^{xz} , \mathbf{a}^{zx} , and \mathbf{a}^{zz} . In this notation, Eq. (6) reads $M\mathbf{a} = 0$, where the $(mn \times 4n)$ -matrix

$$M = \begin{bmatrix} \Gamma \text{diag}(\mathbf{r}^{(1)}) & \Gamma \text{diag}(\mathbf{s}^{(1)}) & \text{diag}(\mathbf{r}^{(1)}) & \text{diag}(\mathbf{s}^{(1)}) \\ \vdots & \vdots & \vdots & \vdots \\ \Gamma \text{diag}(\mathbf{r}^{(m)}) & \Gamma \text{diag}(\mathbf{s}^{(m)}) & \text{diag}(\mathbf{r}^{(m)}) & \text{diag}(\mathbf{s}^{(m)}) \end{bmatrix} \quad (17)$$

is defined by the exponent vectors $\mathbf{r}^{(1)}, \dots, \mathbf{s}^{(m)}$ of the Pauli operators that we want to diagonalize with a circuit based on Γ . Exploiting Gaussian elimination over \mathbb{F}_2 , we can efficiently compute a basis $\mathbf{v}^{(1)}, \dots, \mathbf{v}^{(d)} \in \mathbb{F}_2^{4n}$ of the null space of M . Thus, every $\mathbf{a} \in \mathbb{F}_2^{4n}$ with $M\mathbf{a} = 0$ is of

the form

$$\mathbf{a} = \sum_{j=1}^d \lambda_j \mathbf{v}^{(j)} \quad (18)$$

for some $\boldsymbol{\lambda} \in \mathbb{F}_2^d$. In order to correspond to a physical solution, the vector \mathbf{a} also needs to fulfill

$$\det(A_i) = a_i^{xx} a_i^{zz} + a_i^{zx} a_i^{xz} = 1 \quad (19)$$

for every $i \in \{1, \dots, n\}$ as this will allow us to invert the irreducible representation $\mathcal{C}_n \rightarrow GL(\mathbb{F}_2^{2n}), U \mapsto A$. Based on Ansatz (18), we find

$$a_i^{xx} a_i^{zz} = \sum_{j,j'=1}^d \lambda_j v_i^{xx,(j)} v_i^{zz,(j')} \lambda_{j'} = \boldsymbol{\lambda}^T (\mathbf{x}_i \mathbf{z}_i^T) \boldsymbol{\lambda} \quad (20)$$

and $a_i^{zx} a_i^{xz} = \boldsymbol{\lambda}^T (\mathbf{w}_i \mathbf{y}_i^T) \boldsymbol{\lambda}$, where we have defined

$$\mathbf{x}_i = (v_i^{xx,(1)}, \dots, v_i^{xx,(d)}), \quad (21)$$

$$\mathbf{z}_i = (v_i^{zz,(1)}, \dots, v_i^{zz,(d)}), \quad (22)$$

$$\mathbf{w}_i = (v_i^{xz,(1)}, \dots, v_i^{xz,(d)}), \quad (23)$$

$$\text{and } \mathbf{y}_i = (v_i^{zx,(1)}, \dots, v_i^{zx,(d)}). \quad (24)$$

Inserting this into Eq. (19), we obtain the expression $\det(A_i) = \boldsymbol{\lambda}^T (\mathbf{x}_i \mathbf{z}_i^T + \mathbf{w}_i \mathbf{y}_i^T) \boldsymbol{\lambda}$ and, by defining

$$Q_i = \mathbf{x}_i \mathbf{z}_i^T + \mathbf{w}_i \mathbf{y}_i^T \in \mathbb{F}_2^{d \times d}, \quad (25)$$

we finally arrive at Eq. (15). Since the image of Q_i is contained in the span of \mathbf{x}_i and \mathbf{w}_i , the rank of Q_i cannot be larger than two. In order to solve Eq. (15), we distinguish the values that $\boldsymbol{\lambda}^T \mathbf{x}_i$, $\boldsymbol{\lambda}^T \mathbf{z}_i$, $\boldsymbol{\lambda}^T \mathbf{w}_i$, and $\boldsymbol{\lambda}^T \mathbf{y}_i$ can take. We find that exactly six of the 2^4 possible choices lead to $\boldsymbol{\lambda}^T Q_i \boldsymbol{\lambda} = 1$. Indeed, we have $\det(A_i) = 1$ if and only if

$$\begin{bmatrix} \boldsymbol{\lambda}^T \mathbf{x}_i \\ \boldsymbol{\lambda}^T \mathbf{z}_i \\ \boldsymbol{\lambda}^T \mathbf{w}_i \\ \boldsymbol{\lambda}^T \mathbf{y}_i \end{bmatrix} \in \{\mathbf{b}_1, \dots, \mathbf{b}_6\}, \quad (26)$$

where we have introduced the notation

$$\mathbf{b}_1 = \begin{bmatrix} 0 \\ 0 \\ 1 \\ 1 \end{bmatrix}, \mathbf{b}_2 = \begin{bmatrix} 0 \\ 1 \\ 1 \\ 1 \end{bmatrix}, \mathbf{b}_3 = \begin{bmatrix} 1 \\ 1 \\ 0 \\ 0 \end{bmatrix}, \mathbf{b}_4 = \begin{bmatrix} 1 \\ 1 \\ 0 \\ 1 \end{bmatrix}, \quad (27)$$

$$\mathbf{b}_5 = \begin{bmatrix} 1 \\ 0 \\ 1 \\ 1 \end{bmatrix}, \quad \text{and} \quad \mathbf{b}_6 = \begin{bmatrix} 1 \\ 1 \\ 1 \\ 0 \end{bmatrix}. \quad (28)$$

For example, if $\boldsymbol{\lambda}^T \mathbf{x}_i = 0$, we would need $\boldsymbol{\lambda}^T \mathbf{w}_i = 1$ and $\boldsymbol{\lambda}^T \mathbf{y}_i = 1$ to obtain $\det(A_i) = 1$, where the value of $\boldsymbol{\lambda}^T \mathbf{z}_i$ can be either zero or one. These are the two cases that correspond to \mathbf{b}_1 and \mathbf{b}_2 , respectively. By defining affine

subspaces $\mathcal{X}_i^{(c)} = \{\boldsymbol{\lambda} \in \mathbb{F}_2^d \mid \boldsymbol{\lambda}^T \mathbf{x}_i = c\}$ for $c \in \mathbb{F}_2$, and similarly $\mathcal{Z}_i^{(c)}$, $\mathcal{W}_i^{(c)}$, and $\mathcal{Y}_i^{(c)}$, we can rephrase these two cases as $\boldsymbol{\lambda}$ being contained in the set

$$\mathcal{A}_i = \mathcal{X}_i^{(0)} \cap \mathcal{W}_i^{(1)} \cap \mathcal{Y}_i^{(1)}. \quad (29)$$

For \mathbf{b}_3 and \mathbf{b}_4 , the roles of (x, z) and (w, y) are reversed, i.e., for them Eq. (26) is equivalent to $\boldsymbol{\lambda}$ being contained in the set

$$\mathcal{B}_i = \mathcal{W}_i^{(0)} \cap \mathcal{X}_i^{(1)} \cap \mathcal{Z}_i^{(1)}. \quad (30)$$

Similarly, the remaining two cases \mathbf{b}_5 and \mathbf{b}_6 lead to

$$\mathcal{C}_i = \mathcal{X}_i^{(1)} \cap \mathcal{Z}_i^{(0)} \cap \mathcal{W}_i^{(1)} \cap \mathcal{Y}_i^{(1)} \quad (31)$$

$$\text{and } \mathcal{D}_i = \mathcal{X}_i^{(1)} \cap \mathcal{Z}_i^{(1)} \cap \mathcal{W}_i^{(1)} \cap \mathcal{Y}_i^{(0)}, \quad (32)$$

respectively. By defining

$$\mathcal{L}_i = \mathcal{A}_i \cup \mathcal{B}_i \cup \mathcal{C}_i \cup \mathcal{D}_i, \quad (33)$$

we finally obtain that $\det(A_i) = 1$ is equivalent to $\boldsymbol{\lambda} \in \mathcal{L}_i$.

In the special case where one of the four vectors in Eq. (25) vanishes, say $\mathbf{x}_i = 0$, we need $\boldsymbol{\lambda}^T \mathbf{w}_i \mathbf{y}_i^T \boldsymbol{\lambda} = 1$, which is equivalent to $\boldsymbol{\lambda}^T \mathbf{w}_i = \boldsymbol{\lambda}^T \mathbf{y}_i = 1$. Thus, this case is degenerate and the hypersurface collapses to an affine subspace,

$$\mathcal{L}_i = \mathcal{W}_i^{(1)} \cap \mathcal{Y}_i^{(1)}. \quad (34)$$

Let us explain in greater detail how the intersection in Eq. (34) can be treated computationally. We can assume that neither \mathbf{w}_i nor \mathbf{y}_i are equal to zero because otherwise we would be in the trivial case of $\mathcal{L}_i = \emptyset$. Hence, the linear map $\mathbb{F}_2^d \rightarrow \mathbb{F}_2$, $\boldsymbol{\lambda} \mapsto \boldsymbol{\lambda}^T \mathbf{w}_i$ is surjective, and, by the rank-nullity theorem, its null space $\mathcal{W}_i^{(0)}$ has dimension $d - 1$. Let $j_1 \in \{1, \dots, d\}$ denote a position where $w_{i,j_1} = 1$. For every other index $j \neq j_1$, we obtain a basis vector for $\mathcal{W}_i^{(0)}$, which stores the value 1 in position j , the value of $w_{i,j}$ in position j_1 , and 0 in every other position. The elements of $\mathcal{W}_i^{(0)}$ and $\mathcal{W}_i^{(1)}$ are in one-to-one correspondence to each other via the addition of a support vector $\mathbf{w}'_i \in \mathcal{W}_i^{(1)}$. For the latter, we can pick the standard basis vector $\mathbf{e}_{j_1} = (0, \dots, 0, 1, 0, \dots, 0) \in \mathbb{F}_2^d$, where the 1 is in position j_1 . Analogously, we can find a basis and a support vector for $\mathcal{Y}_i^{(1)}$. As we show next, the intersection \mathcal{L}_i of the two affine subspaces $\mathcal{W}_i^{(1)}$ and $\mathcal{Y}_i^{(1)}$ is indeed an affine subspace.

For pedagogical reasons, we now explain how to computationally carry out the intersection $\mathcal{U} \cap \tilde{\mathcal{U}}$ of two affine subspaces $\mathcal{U}, \tilde{\mathcal{U}} \subset \mathbb{K}^d$, where \mathbb{K} can be any field. Let $\mathbf{u}_1, \dots, \mathbf{u}_m$, and $\tilde{\mathbf{u}}_1, \dots, \tilde{\mathbf{u}}_{\tilde{m}}$ be bases of \mathcal{U} and $\tilde{\mathcal{U}}$, respectively. Furthermore, pick $\mathbf{u}' \in \mathcal{U}$ and $\tilde{\mathbf{u}}' \in \tilde{\mathcal{U}}$. This yields a parametrization $\mathcal{U} = \{\mathbf{u}' + \sum_{i=1}^m \mu_i \mathbf{u}_i \mid \mu_i \in \mathbb{K}\}$ and similarly for $\tilde{\mathcal{U}}$. To compute a basis and a support vector of $\mathcal{U} \cap \tilde{\mathcal{U}}$, we define two matrices $U \in \mathbb{K}^{d \times m}$, $\tilde{U} \in \mathbb{K}^{d \times \tilde{m}}$, whose columns are given by the basis vectors of \mathcal{U} and

$\tilde{\mathcal{U}}$, respectively. Via Gaussian elimination over \mathbb{K} , we can bring the matrix $U' = (U, -\tilde{U}, \mathbf{u}' - \tilde{\mathbf{u}}') \in \mathbb{K}^{d \times (m+\tilde{m}+1)}$ to its reduced row-echelon form (RREF) and read off a basis $\mathbf{t}_1, \dots, \mathbf{t}_\ell \in \mathbb{K}^{m+\tilde{m}}$ of the null space of $(U, -\tilde{U})$. If we denote the truncation of these basis vectors to the first m rows by $\bar{\mathbf{t}}_i = (t_{i,1}, \dots, t_{i,m})$ for all $i \in \{1, \dots, \ell\}$, a basis of $\mathcal{U} \cap \tilde{\mathcal{U}}$ is given by $U\bar{\mathbf{t}}_1, \dots, U\bar{\mathbf{t}}_\ell \in \mathbb{K}^d$. Finally, if the last column of U' is a non-pivot column, i.e., $\text{rank}(U') = \text{rank}(U, -\tilde{U})$, then the last column of the RREF of U' is a support vector for $\mathcal{U} \cap \tilde{\mathcal{U}}$. Otherwise, $\mathcal{U} \cap \tilde{\mathcal{U}}$ is empty.

In our search for a point $\lambda \in \mathcal{L}$, we first compute the intersection of all hypersurfaces \mathcal{L}_i with $\text{rank}_{\mathbb{F}_2}(Q_i) = 1$. After potentially relabelling some of the qubits, we can assume $Q_i = \mathbf{x}_i \mathbf{z}_i^T$ and $Q_j = \mathbf{w}_j \mathbf{y}_j^T$ for all $i \in \{1, \dots, l\}$ and $j \in \{l+1, \dots, n-k\}$. Then, the intersection of all rank-1 quadric hypersurfaces is given by

$$\bigcap_{i=1}^{n-k} \mathcal{L}_i = \left\{ \lambda \in \mathbb{F}_2^d \mid \begin{array}{l} \lambda^T \mathbf{x}_i = \lambda^T \mathbf{z}_i = \lambda^T \mathbf{y}_j = \lambda^T \mathbf{w}_j = 1 \\ \text{for all } 1 \leq i \leq l < j \leq n-k \end{array} \right\} \quad (35)$$

$$= \left\{ \lambda \in \mathbb{F}_2^d \mid C\lambda = \mathbf{1} \right\}, \quad (36)$$

where $C = (\mathbf{x}_1, \mathbf{z}_1, \dots, \mathbf{x}_l, \mathbf{z}_l, \mathbf{y}_{l+1}, \mathbf{w}_{l+1}, \dots, \mathbf{y}_{n-k}, \mathbf{w}_{n-k})^T$ is the $(2(n-k) \times d)$ -matrix whose rows are given by the row vectors \mathbf{x}_i^T etc., and $\mathbf{1} = (1, \dots, 1)$. Using Gaussian elimination over \mathbb{F}_2 , we can compute the RREF of the extended matrix $(C, \mathbf{1}) \in \mathbb{F}_2^{2(n-k) \times (d+1)}$. If the last column of the RREF is a pivot column, we are in the solutionless case $\mathcal{L} = \emptyset$. This is what is meant with the statement “If no solution to Eq. (6) exists, an efficient test can sometimes verify this.” from the main text. Otherwise, this column is an offset vector for $\mathcal{L}_1 \cap \dots \cap \mathcal{L}_{n-k}$, while every non-pivot column of the RREF of C yields a basis vector in the standard way of linear algebra.

Let us finally turn to the computationally most demanding part that deals with the rank-2 hypersurfaces $\mathcal{L}_{n-k+1}, \dots, \mathcal{L}_n$. Similar to the matrix C in Eq. (36), we introduce a $(4k \times d)$ -matrix

$$C' = (\mathbf{x}_{n-k+1}, \dots, \mathbf{x}_n, \mathbf{z}_n, \mathbf{w}_n, \mathbf{y}_n)^T, \quad (37)$$

i.e., for every $j \in \{1, \dots, k\}$, the four rows of C' from row $4j-3$ to row $4j$ are given by $\mathbf{x}_{n-k+j}^T, \mathbf{z}_{n-k+j}^T, \mathbf{w}_{n-k+j}^T$, and \mathbf{y}_{n-k+j}^T . Then, a vector $\lambda \in \mathbb{F}_2^d$ is contained in $\mathcal{L}_{n-k+1} \cap \dots \cap \mathcal{L}_n$ if and only if $C'\lambda = \mathbf{b}_{i_1} \oplus \dots \oplus \mathbf{b}_{i_k}$ for some $i_1, \dots, i_k \in \{1, \dots, k\}$, where the vectors $\mathbf{b}_1, \dots, \mathbf{b}_k$ in the direct sum

$$\mathbf{b}_{i_1} \oplus \dots \oplus \mathbf{b}_{i_k} = \begin{bmatrix} \mathbf{b}_{i_1} \\ \vdots \\ \mathbf{b}_{i_k} \end{bmatrix} \quad (38)$$

have been introduced earlier in Eqs. (27)–(28). If it is our goal to unambiguously ascertain whether or not \mathcal{L} is empty, we have to check an exponential number of cases. This is only feasible for small qubit numbers n or

for graphs with small components, as we will explain in Sec. II E. To save computing time, we treat all combinations of the vectors \mathbf{b}_i at once by introducing (4×6^j) -matrices

$$B_j = (\underbrace{\mathbf{b}_1, \dots, \mathbf{b}_1}_{6^{j-1} \text{ times}}, \dots, \underbrace{\mathbf{b}_6, \dots, \mathbf{b}_6}_{6^{j-1} \text{ times}}) \quad (39)$$

for $j \in \{1, \dots, k\}$ and using them as blocks for enlarging C' to a matrix $B \in \mathbb{F}_2^{4k \times (d+6^k)}$. Hereby, the four rows from row $4j-3$ to row $4j$ are given by

$$\begin{bmatrix} \mathbf{x}_{n-k+j}^T \\ \mathbf{z}_{n-k+j}^T \\ \mathbf{w}_{n-k+j}^T \\ \mathbf{y}_{n-k+j}^T, \quad \underbrace{B_j, \dots, B_j}_{6^{k-j} \text{ times}} \end{bmatrix} \in \mathbb{F}_2^{4 \times (d+6^k)}. \quad (40)$$

In other words, B is the matrix that arises from C' by appending all vectors of the form $\mathbf{b}_{i_1} \oplus \dots \oplus \mathbf{b}_{i_k}$ as additional columns. Next, we use Gaussian elimination to bring B to a row-echelon form; here, time can be saved as it is not necessary to compute the RREF of B . This reveals the non-pivot columns of B . Every non-pivot column of the form $\mathbf{b}_{i_1} \oplus \dots \oplus \mathbf{b}_{i_k}$ indicates the existence of at least one vector $\lambda \in \mathcal{L}_{n-k+1} \cap \dots \cap \mathcal{L}_n$. However, we are looking for a λ that also lies in the affine space $\mathcal{L}_1 \cap \dots \cap \mathcal{L}_{n-k}$. To accomplish this, we start by computing a basis and an offset vector of the entire affine space

$$\{\lambda \in \mathbb{F}_2^d \mid C'\lambda = \mathbf{b}_{i_1} \oplus \dots \oplus \mathbf{b}_{i_k}\}. \quad (41)$$

Then, we use the procedure explained before to compute the intersection of the two affine subspaces in Eqs. (36) and (41). Since this results in a subset of \mathcal{L} , we can finish if we find a non-pivot column $\mathbf{b}_{i_1} \oplus \dots \oplus \mathbf{b}_{i_k}$ in the right part of B for which this intersection is not empty. Otherwise, if this approach fails for all non-pivot columns, we can finally infer $\mathcal{L} = \emptyset$. In any case, we obtain a conclusive answer whether or not a layer of single-qubit Clifford gates exists such that the corresponding graph-based circuit (see main text, Fig. 1) diagonalizes the given set of commuting Pauli operators.

C. Cutoff for Restricting the Search Space

In the approach of the previous subsection to algebraically solve Eq. (6) from the main text, we iterate through a number of affine subspaces that grows exponentially in the number $k \leq n$ of qubits i for which \mathcal{L}_i is a rank-2 quadric hypersurface. For large problem sizes, this is infeasible and it is beneficial to restrict the exhaustive part of the search to a smaller number $c \leq k$ of rank-2 quadric hypersurfaces. For example, we can work with a constant cutoff

$$c = \text{const.} \quad (42)$$

or with a logarithmically growing cutoff

$$c = \text{const.} \times \lfloor \log(n) \rfloor \quad (43)$$

in order to turn the subroutine of attempting to find a solution $\lambda \in \mathcal{L}$ into an efficient algorithm. If we do not find a solution in this way, it can be advantageous to treat this case as if \mathcal{L} was empty, i.e., we skip the current subgraph in our Pauli grouping algorithm. We integrate the cutoff into our subroutine by replacing the matrix $B \in \mathbb{F}_2^{4k \times (d+6^k)}$ [recall Eq. (40)] by a smaller matrix $B' \in \mathbb{F}_2^{(4c+3(k-c)) \times (d+6^c)}$. The first $4c$ rows of B' are again given by Eq. (40), but with 6^{c-j} instead of 6^{k-j} blocks of the form B_j . For the remaining part, we dispose of the \mathbf{z} -row and set the three rows from row $4c+3j-2$ to row $4c+3j$ to

$$\begin{bmatrix} \mathbf{x}_{n-k+c+j}^T & 0 & \cdots & 0 \\ \mathbf{w}_{n-k+c+j}^T & 1 & \cdots & 1 \\ \mathbf{y}_{n-k+c+j}^T & 1 & \cdots & 1 \end{bmatrix} \in \mathbb{F}_2^{3 \times (d+6^c)} \quad (44)$$

for all $j \in \{1, \dots, k-c\}$. In this way, we have efficiently combined the two cases that correspond to \mathbf{b}_1 and \mathbf{b}_2 from Eq. (27). The remainder of our approach stays unchanged. By restricting from B to B' , we will only be able to find solutions $\lambda \in \mathcal{L}_{n-k} \cap \dots \cap \mathcal{L}_n$ which are contained in the subspace

$$\left(\bigcap_{i=n-k+1}^{n-k+c} \underbrace{\mathcal{A}_i \cup \mathcal{B}_i \cup \mathcal{C}_i \cup \mathcal{D}_i}_{=\mathcal{L}_i} \right) \cap \bigcap_{i=n-k+c+1}^n \underbrace{\mathcal{A}_i}_{\subset \mathcal{L}_i}. \quad (45)$$

Note that the space in Eq. (45) is a union of only 4^c affine subspaces. In Fig. 4, we have highlighted the subspaces $\mathcal{A}_i \subset \mathcal{L}_i$ with an increased line width. In the depicted example, there are $k=3$ rank-2 hyper-surfaces. Hence, there are four possible choices for the cutoff $c \in \{0, \dots, k\}$. For $c=k$, we recover the original approach and are able to find all $|\mathcal{L}|=6$ depicted solutions. For $c=2$, the restricted search space $\mathcal{L}_1 \cap \mathcal{L}_2 \cap \mathcal{A}_3$ only contains two elements. For $c=1$, there is a single solution $\lambda \in \mathcal{L}_1 \cap \mathcal{A}_2 \cap \mathcal{A}_3$. Note that neither $\mathcal{A}_1 \cap \mathcal{A}_2$ nor $\mathcal{A}_1 \cap \mathcal{A}_3$ nor $\mathcal{A}_2 \cap \mathcal{A}_3$ is empty, but $\mathcal{A}_1 \cap \mathcal{A}_2 \cap \mathcal{A}_3$ is. Therefore, we would not be able to find any solution for $c=0$.

To get a glimpse of how much information is lost when the cutoff is applied, we consider a quantum device with $n=5$ linearly connected qubits such as the superconducting quantum computer *ibmq-santiago*. The associated connectivity graph possesses four edges and 2^4 subgraphs. Every subgraph corresponds to a template that can be complemented with a layer of single-qubit Clifford gates to a HT circuit (see main text, Fig. 1). For every subgraph, we investigate how many of the $4^n = 1024$ Pauli operators can be **individually** diagonalized with such a circuit. If we succeed in finding a solution $\lambda \in \mathcal{L}$ for a given cutoff c , the corresponding Pauli operator P is identified as being *diagonalizable*. In Fig. 5, we plot

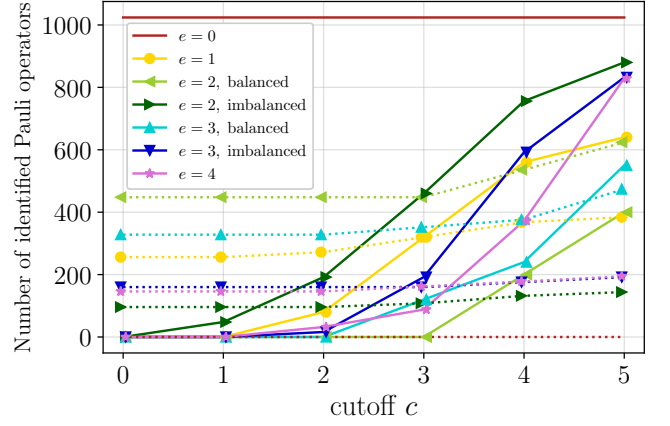


FIG. 5. Number of Pauli operators that are identified as diagonalizable (solid lines) or non-diagonalizable (dotted lines) by a graph-based circuit as in Fig. 1 for the 6 subgraph classes of a 5-vertex path graph as a function of the cutoff c . Each circuit only needs to diagonalize a single operator. The colors and markers indicate the number e of the subgraphs' edges and, for the ambiguous cases, whether all edges belong to the same connected component (connected) or not (disconnected). For the subgraph with $e=0$ edges (red, no markers), we did not apply the cutoff because individual Pauli operators can be trivially diagonalized by single-qubit Clifford gates.

the number of Pauli operators identified as diagonalizable as a function of c (solid lines). Hereby, different lines correspond to different subgraphs. Furthermore, we plot the number of operators P that can be identified as *non-diagonalizable* (dotted lines), i.e., the cases where $\mathcal{L}_1 \cap \dots \cap \mathcal{L}_k = \emptyset$ or where $Q_i = 0$ for one of the qubits i . For completeness, we include the trivial case $e=0$, in which every Pauli operator can be individually diagonalized with the standard, qubit-wise diagonalization circuit (H for X , HS^\dagger for Y , and I for I and Z). For the other cases (with $e > 0$), we consistently observe the following behavior: for the most drastic cutoff of $c=0$, a considerable portion of the set of non-diagonalizable operators is recognized, whereas not a single diagonalizable operator can be identified. As expected, the number of identifiable Pauli operators monotonically increases when the cutoff c is enlarged. Eventually, when no cutoff is applied ($c=n$), we are able to classify the entire set of Pauli operators. Let us now compare curves corresponding to different subgraphs. Since the considered problem is symmetric under graph isomorphisms, the (yellow) curves for all graphs with $e=1$ coincide. For subgraphs with $e=2$ (green) and $e=3$ (blue), respectively, there are two classes which we call *balanced* ($\textcircled{1}-\textcircled{2} \textcircled{3}-\textcircled{4} \textcircled{5}$ for $e=2$ and $\textcircled{1}-\textcircled{2}-\textcircled{3} \textcircled{4}-\textcircled{5}$ for $e=3$) and *imbalanced* ($\textcircled{1}-\textcircled{2}-\textcircled{3} \textcircled{4} \textcircled{5}$ for $e=2$ and $\textcircled{1}-\textcircled{2}-\textcircled{3}-\textcircled{4} \textcircled{5}$ for $e=3$), referring to the sizes of the subgraphs' connected components. For every choice of $c > 0$, the largest number of Pauli operators can be diagonalized with the HT circuit corresponding to an imbalanced subgraph with $e=2$ edges (dark green), whereas the fewest number

of Pauli operators is diagonalizable with circuits based on a balanced subgraph with $e = 2$ (bright green). A similar but less pronounced behavior is observed for the templates with $e = 3$ edges. As we are going to explain below, this is due to the existence of lone edges, i.e., connected components of the subgraph of size two. Finally note that, with the exception of ①–② ③–④ ⑤, every subgraph allows us to diagonalize the majority of the Pauli operators. This abundance of HT-diagonalizable operators is an important ingredient for improving on previous Pauli groupings (see Sec. VI).

To understand why lone edges in a given subgraph lead to a large number of non-diagonalizable Pauli operators, we first explain the simpler case of two-qubit HT circuits that feature exactly one CZ-gate (see Fig. 1). If followed by a qubit-wise readout, such a circuit U realizes a Bell measurement, which is a crucial building block of the well-known quantum teleportation protocol [38]. Note that U can only rotate an entangled basis to the computational basis. In other words, if U transforms P_1, P_2 , and P_3 into $I \otimes Z, Z \otimes I$, and $Z \otimes Z$, then every P_i must have a Pauli weight of two, i.e., $P_i \in \{X, Y, Z\}^{\otimes 2}$ up to a global phase. In summary, among all $4^2 = 16$ two-qubit Pauli operators the six weight-one operators are not diagonalizable, while $I \otimes I$ as well as the nine weight-two operators are diagonalizable by a circuit based on the graph ①–②. Next, consider the disconnected four-qubit graph ①–② ③–④. A Pauli operator of the form $P = P^{(1)} \otimes \dots \otimes P^{(4)}$ is non-diagonalizable if and only if the same is true either for $P^{(1)} \otimes P^{(2)}$ and ①–②, for $P^{(3)} \otimes P^{(4)}$ and ③–④, or for both. If $P^{(1)} \otimes P^{(2)}$ is non-diagonalizable (6 cases), the choice of $P^{(3)} \otimes P^{(4)}$ is irrelevant (16 cases); if, however, $P^{(1)} \otimes P^{(2)}$ is diagonalizable (10 cases), $P^{(3)} \otimes P^{(4)}$ has to be non-diagonalizable (6 cases). This gives a total amount of $6 \times 16 + 10 \times 6 = 156$ non-diagonalizable Pauli operators for the graph ①–② ③–④. It follows that there exist exactly $156 \times 4 = 624$ non-diagonalizable Pauli operators for the graph ①–② ③–④ ⑤ because the choice of the fifth operator is irrelevant. This explains why the bright green, dotted curve ($e = 2$, disconnected) in Fig. 5 takes the comparatively large value of 624 for $c = 5$. More generally, we can state that a graph will have a large amount of non-diagonalizable Pauli operators if it possesses a lot of two-vertex components (lone edges). Even more generally, we expect a drop in diagonalizable operators for every component with the property *every vertex has an odd number of neighbors* as this will make it impossible to diagonalize odd-weight Pauli operators on the subset of qubits that belong to such a component [39, 40].

D. Numerical Optimization

So far, we have only discussed algebraic strategies to solve Eq. (6) from the main text. Our exhaustive approach (see Sec. II B) has the theoretical advantage of leading to a conclusive answer whether or not there ex-

ists a solution $\lambda \in \mathcal{L}$ but the practical disadvantage of a worst-case exponential runtime scaling. By introducing a cutoff c (see Sec. II C), we obtain a modification with the theoretical advantage of being computationally efficient but the practical disadvantage of potentially being unable to find a solution if c is too small. Here, we reformulate the problem as a numerical optimization problem, which performs well in practice.

In Sec. II B, we have stated the problem in the following form: find $\lambda \in \mathbb{F}_2^d$ such that

$$\lambda^T Q_i \lambda = 1 \quad (46)$$

for all $i \in \{1, \dots, n\}$. Note that Eq. (46) is an equation in the binary field $\mathbb{F}_2 = \{0, 1\}$, in which all arithmetic operations are defined modulo 2. By introducing integer slack variables μ_1, \dots, μ_n , we obtain an equivalent problem: find $\lambda \in \{0, 1\}^d \subset \mathbb{Z}^d$ and $\mu \in \mathbb{Z}^n$ such that

$$\lambda^T Q_i \lambda + 2\mu_i = 1. \quad (47)$$

The matrix Q_i was defined in Eq. (25) and is considered a matrix over \mathbb{F}_2 in Eq. (46). In Eq. (47), however, we regard Q_i as a matrix with entries in $\{0, 1\} \subset \mathbb{R}$, and, by replacing it with $(Q_i + Q_i^T)/2$, we can assume that Q_i is a real, symmetric matrix. Therefore, solving Eq. (6) is equivalent to solving the feasibility problem of the (non-convex) mixed integer quadratically constrained program (MIQCP)

$$\min_{\lambda, \mu} 0 \quad \text{s.t.} \quad \text{Eq. (47) holds for every } i. \quad (48)$$

We point out that the general class of MIQCP is NP-hard and leave a detailed investigation about the complexity of the problem instances occurring in Eq. (48) for future research.

E. Further Insights and Open Problems

As discussed in length before, the bottleneck of grouping a set of Pauli operators into jointly-HT-diagonalizable subsets is solving Eq. (6) from the main text. To reduce the computational cost of this subroutine, we have dedicated this subsection to share some tricks. Furthermore, we present a few ideas for potential future research.

1. Treat $\Gamma = 0$ as a special case.

For the trivial subgraph, there is no need to apply the machinery developed in Sec. II B. Instead, we can simply check if the Pauli operators P_1, \dots, P_m belong to a tensor product basis (TPB) by testing whether or not these operators are qubit-wise commuting (QWC).

2. Treat every component of the subgraph individually.

For subgraphs Γ with multiple connected components, we can enormously speed up the search for a solution λ by breaking down the problem, individually solving it for each component, and finally combining the solutions of the subproblems. Indeed, if $\Gamma = \Gamma_1 \oplus \Gamma_2$ is the direct sum

of two adjacency matrices Γ_1 and Γ_2 with k and $n - k$ qubits, respectively, the left-hand side of Eq. (6) becomes

$$\begin{bmatrix} \Gamma_1 & \\ & \Gamma_2 \end{bmatrix} \left(\begin{bmatrix} A_1^{xx} & \\ & A_2^{xx} \end{bmatrix} \begin{bmatrix} R_1 \\ R_2 \end{bmatrix} + \begin{bmatrix} A_1^{xz} & \\ & A_2^{xz} \end{bmatrix} \begin{bmatrix} S_1 \\ S_2 \end{bmatrix} \right), \quad (49)$$

where we have defined $A_1^{xx} = \text{diag}(a_1^{xx}, \dots, a_k^{xx})$, $A_2^{xx} = \text{diag}(a_{k+1}^{xx}, \dots, a_n^{xx})$, and similarly for A^{xz} . Furthermore, R_1 and R_2 are given by the first k and last $n - k$ rows of R , respectively, and likewise for S . By multiplying out expression (49) in a block-wise manner, we find that Eq. (6) is equivalent to

$$\begin{bmatrix} \Gamma_1(A_1^{xx}R_1 + A_1^{xz}S_1) \\ \Gamma_2(A_2^{xx}R_2 + A_2^{xz}S_2) \end{bmatrix} = \begin{bmatrix} A_1^{zx}R_1 + A_1^{zz}S_1 \\ A_2^{zx}R_2 + A_2^{zz}S_2 \end{bmatrix}. \quad (50)$$

While the original problem had a worst-case scaling that was exponential in n , solving the two decoupled equations in Eq. (50) has a worst-case scaling of $\exp(\min(k, n - k))$. We emphasize that this breaking of the exponential scaling guarantees the efficient construction (if they exist) of single-qubit Clifford-gate layers for graphs for which the size of the largest connected component grows at most logarithmically in n .

3. Develop warm-starting methods.

The definition of the solution space \mathcal{L} from Sec. II A depends on the Pauli operators P_1, \dots, P_m , for which we attempt to construct a diagonalization circuit. In our new Pauli grouping algorithm, we successively increase the number of Pauli operators. To speed up the attempt to compute a circuit for P_1, \dots, P_m , it may be possible to recycle information that has been obtained during construction of the circuit for P_1, \dots, P_{m-1} . As a first step, one could investigate how the null space of the matrix M defined in Eq. (17) changes when a new Pauli operator is added.

4. Apply elimination theory.

The equations, that we encounter when constructing HT diagonalization circuits, are polynomial equations in multiple variables over a field. Thus, they belong into the realm of algebraic geometry and can, at least in principle, be solved by applying elimination theory [41]. This would require to compute a Gröbner basis of the ideal $\mathfrak{a} \subset \mathbb{F}_2[\lambda_1, \dots, \lambda_d]$, which is generated by the quadratic polynomials $\lambda^T Q_1 \lambda + 1, \dots, \lambda^T Q_n \lambda + 1$, with respect to the lexicographical order. In a similar manner as the Gaussian algorithm yields a basis of the null space of a given matrix, Buchberger's algorithm yields a Gröbner basis of \mathfrak{a} . Although, in general, Buchberger's algorithm is inefficient, it could still be that it is feasible for certain instances of our problem.

5. Exploit small circuits as building blocks.

To facilitate the construction of HT diagonalization circuits with qubit numbers exceeding the ones reported in this paper, it is desirable to investigate how to combine multiple small-scale HT circuits into a larger one.

III. HARDWARE-TAILORED HAMILTONIAN EXPONENTIATION

In this section, we address a fundamental aspect of quantum computation that could potentially benefit from hardware-tailored (HT) Pauli groupings: decomposing unitary gates. The phase-gate $\exp(i c Z)$ with $c \in \mathbb{R}$, for example, is a basic single-qubit gate, which can be directly implemented on most quantum hardware [42]. Similarly, $\text{CNOT} = |0\rangle\langle 0| \otimes I + |1\rangle\langle 1| \otimes X$ is a basic two-qubit gate that flips the state of the second (target) qubit, depending on the state of the first (control) qubit. It is well known that every unitary gate is of the form $\exp(iO)$ for some Hermitian operator O [43]. Furthermore, $\exp(iO)$ can be decomposed into a sequence of CNOT-gates, Hadamard gates $H = \frac{1}{\sqrt{2}}(X + Z)$, and phase-gates $\exp(i c Z)$ with $c \in \mathbb{R}$, e.g., $\exp(i c Z \otimes Z) = \text{CNOT}(I \otimes \exp(i c Z))\text{CNOT}$. Likewise, the n -qubit gate

$$\exp(i c Z^{\mathbf{s}}) = \left(\prod_{j=1}^{n-1} \text{CNOT}_{j,n}^{s_j} \right) \left(I^{\otimes(n-1)} \otimes \exp(i c Z) \right) \left(\prod_{j=1}^{n-1} \text{CNOT}_{j,n}^{s_j} \right), \quad (51)$$

can be implemented with the quantum circuit depicted in Fig. 6, where the binary vector $\mathbf{s} \in \mathbb{F}_2^n$ determines the involved qubits, and we assumed $s_n = 1$ to ease notation. Next, let $P \in \{I, X, Y, Z\}^{\otimes n}$ be a Pauli operator and U a quantum circuit diagonalizing it, i.e., $UPU^\dagger = \pm Z^{\mathbf{s}}$ for some $\mathbf{s} \in \mathbb{F}_2^n$ (see main text, Fig. 1). Then, an expansion of the exponential series yields

$$\exp(i c P) = U^\dagger \exp(\pm i c Z^{\mathbf{s}}) U. \quad (52)$$

Hence, the gate $\exp(i c P)$ can be implemented by first

applying U , then $\exp(\pm i c Z^{\mathbf{s}})$, then U^\dagger .

Finally, consider the most general case in which O is a linear combination of Pauli operators $P_i \in \{I, X, Y, Z\}^{\otimes n}$ with coefficients $c_i \in \mathbb{R}$. As thoroughly discussed in this paper, applying a Pauli grouping algorithm decomposes O into a sum $O = \sum_{i=1}^N O_i$ of operators

$$O_i = \sum_{j=1}^{m_i} c_{i,j} P_{i,j}. \quad (53)$$

By construction, the Pauli operators $P_{i,1}, \dots, P_{i,m_i}$ can

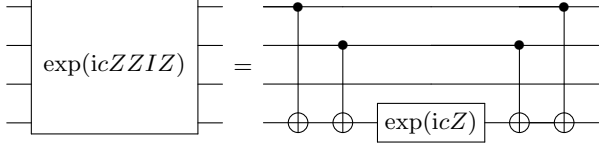


FIG. 6. Example of the circuit identity in Eq. (51) for $n = 4$ qubits and $\mathbf{s} = (1, 1, 0, 1)$. Note that the outer CNOT-gates could alternatively target qubit 2 instead of qubit 4, which would require fewer SWAP-gates on a quantum chip with linear hardware connectivity.

be simultaneously diagonalized with a Clifford circuit U_i , i.e., there exist binary vectors $\mathbf{s}^{(i,j)}$ such that

$$U_i P_{i,j} U_i^\dagger = \pm Z^{\mathbf{s}^{(i,j)}} \quad (54)$$

for every $i \in \{1, \dots, N\}$ and $j \in \{1, \dots, m_i\}$. In particular, the operators $P_{i,1}, \dots, P_{i,m_i}$ commute, which yields the decomposition

$$\exp(iO_i) = \prod_{j=1}^{m_i} \exp(ic_{i,j} P_{i,j}). \quad (55)$$

By inserting Eqs. (54)–(53) into Eq. (55) and cancelling avoidable basis-change circuits of the form $U_i^\dagger U_i$, we find

$$\exp(iO_i) = U_i^\dagger \left(\prod_{j=1}^{m_i} \exp(\pm ic_{i,j} Z^{\mathbf{s}^{(i,j)}}) \right) U_i. \quad (56)$$

We point out that by carefully selecting the ordering of the commuting gates $\exp(\pm ic_{i,j} Z^{\mathbf{s}^{(i,j)}})$, it might be possible to cancel some of the CNOT-gates stemming from Eq. (51). In order to finally decompose the gate $\exp(iO)$, we have to be careful because, in general, the operators O_1, \dots, O_N do not commute. In theory, $\exp(iO)$ can be exactly implemented with an infinitely long quantum circuit

$$\exp(iO) = \lim_{k \rightarrow \infty} \left(\prod_{i=1}^N \exp\left(\frac{iO_i}{k}\right) \right)^k, \quad (57)$$

known as the Lie-Trotter product formula [44]. In practice, however, Eq. (57) is truncated at a finite value of k , which yields the approximation

$$\exp(iO) \approx \left(\prod_{i=1}^N U_i^\dagger \left(\prod_{j=1}^{m_i} \exp\left(\pm i \frac{c_{i,j}}{k} Z^{\mathbf{s}^{(i,j)}}\right) \right) U_i \right)^k. \quad (58)$$

Thus, the resulting quantum circuit contains $2Nk$ gates for diagonalization (U_i and U_i^\dagger) as well as Mk rotations of the form $\exp(icZ^{\mathbf{s}})$. For applications in quantum chemistry, where O is the Hamiltonian of a molecule, the number M of Pauli operators scales with the fourth power of

number n of qubits [3]. The complexity of the diagonalization circuits and their number N depends on the Pauli grouping algorithm in place. If the Pauli operators are grouped into tensor product bases, every U_i is just a layer of single-qubit Clifford gates but, typically, there are as many as $N_{\text{TPB}} \approx M/3 = \mathcal{O}(n^4)$ of them [5]. On the other extreme, empirically [6, 7], only $N_{\text{GC}} = \mathcal{O}(n^3)$ diagonalization circuits are needed if the Pauli operators are grouped into general commuting sets. In this case, however, the diagonalization circuits U_i require up to $n(n-1)/2$ two-qubit gates and an additional number of SWAP-gates [34]. Finally, for HT Pauli groupings, the diagonalization circuits have a constant depth and are tailored to the hardware connectivity. We leave the question of which connectivities are needed such that N_{HT} scales better than $\mathcal{O}(n^4)$ as an open problem.

Note added: In every iteration of our Pauli grouping algorithm (Algorithm 1 in Sec. V), multiple diagonalization circuits are created and only the “best” one is kept. If the purpose of the constructed Pauli grouping is to speed up estimating $\langle O \rangle$, “best” is heuristically quantified by the number of jointly-measurable Pauli operators (weighted with coefficients), see Eq. (66) in Sec. V. If, however, its purpose is a resource-efficient implementation of the Trotter-step circuit in Eq. (58), such a heuristic is likely suboptimal: even though such a Pauli grouping would approximately minimize the number N of basis-change circuit components $U_{i+1} U_i^\dagger$ in Eq. (58), the problem of resource-efficiently implementing $\exp(\pm i \frac{c_{i,j}}{k} Z^{\mathbf{s}^{(i,j)}})$ would remain unaddressed. Since we need to implement Mk circuits of the form $\exp(icZ^{\mathbf{s}})$ but only $Nk < Mk$ basis-change circuits, implementing the former is the true bottleneck. Note that the support of the exponent vectors $\mathbf{s}^{(i,j)}$ influences the number of CNOT- and SWAP-gates in the trees of CNOT-gates that are needed for the implementation of $\exp(\pm i \frac{c_{i,j}}{k} Z^{\mathbf{s}^{(i,j)}})$ as in Fig. 6. Algorithm 1 is flexible and would allow us to incorporate such information as we could replace the notion of “best” from Eq. (66) by a figure of merit that punishes choices of U_i for which $\mathbf{s}^{(i,1)}, \dots, \mathbf{s}^{(i,m_i)}$ leads to a large overhead in SWAP-gates. We believe that such an approach would enable access to resource-efficient HT Hamiltonian exponentiation and encourage the community to explore this opportunity in future research.

IV. OPTIMALLY ALLOCATING SHOTS TO READOUT CIRCUITS

In this section, we review the well-known strategy for optimally distributing a fixed number N^{shots} of shots among the readout circuits of a given Pauli grouping [9]. Building on this, we then propose a shot-allocation heuristic, which does not require any knowledge about the state that is measured. This appendix is intended to motivate Eq. (66), which was used for the construction of the hardware-tailored Pauli groupings throughout this work.

Consider a decomposition of $O = \sum_{i=1}^M c_i P_i$ into fragments $O_i = \sum_{j=1}^{m_i} c_{i,j} P_{i,j}$ as in Eq. (68), for each of which the Pauli operators $P_{i,1}, \dots, P_{i,m_i}$ can be measured with a single quantum circuit. For a fixed shot budget, it is important to know how the number of available shots should be distributed over the different measurement circuits. The selected shot allocation has an influence on the resulting estimator $\langle O \rangle$ of the true expectation value $\langle O \rangle$. The optimal shot allocation minimizes the variance $\epsilon^2 = \text{Var}[\langle O \rangle]$ under the constraint $N^{\text{shots}} = \sum_{i=1}^N n_i$, where n_i denotes the number of shots assigned for the measurement of fragment O_i . In an experiment, the samples for measuring different fragments are obtained independently. This manifests itself in $\text{Cov}[\langle O_i \rangle, \langle O_j \rangle] = 0$ for all $i \neq j$. Thus, we obtain

$$\epsilon^2 = \sum_{i=1}^N \text{Var}[\langle O_i \rangle]. \quad (59)$$

Since the variances $\text{Var}[\langle O_i \rangle] = \text{Var}[O_i]/n_i$ directly follow from the standard error on the sample mean, we find

$$\epsilon^2 = \sum_{i=1}^N \frac{1}{n_i} \sum_{j,j'=1}^{m_i} c_{i,j} c_{i,j'} \text{Cov}[P_{i,j}, P_{i,j'}]. \quad (60)$$

It is therefore evident that the covariances of the Pauli operators within a given fragment can strongly influence the final accuracy [2].

In Ref. [9], Crawford et al. exploit Lagrange multipliers to show that Eq. (60) is minimized for

$$n_i \propto \sqrt{\text{Var}[O_i]}, \quad (61)$$

where the proportionality constant is given by

$$\frac{N^{\text{shots}}}{\sum_{j=1}^N \sqrt{\text{Var}[O_j]}} = \frac{1}{\epsilon^2} \sum_{j=1}^N \sqrt{\text{Var}[O_j]}. \quad (62)$$

This provides the optimal strategy for distributing the available shots among the different readout circuits. Implementing this strategy in practice, however, requires knowledge about $\text{Var}[O_1], \dots, \text{Var}[O_N]$. There exist several approaches to address this problem: one possibility is to approximate these variances by performing a classically tractable calculation [20]. For certain quantum algorithms, one can exploit an adaptive shot-allocation strategy [45–47]. Finally, one can experimentally obtain an estimator $\widehat{\text{Var}[O_i]}$ from the same measurement data that is gathered for the estimation of $\langle O_i \rangle$ [6].

When implementing the latter approach, one has to acquire data by executing the measurement circuit for O_i . In the beginning, the optimal shot allocation is still unknown since any information about $\text{Var}[O_i]$ is not yet available. Thus, one has to rely on heuristics, such as simply allocating the same number of shots to each of the circuits. As an alternative, we can introduce a slightly

more sophisticated shot-allocation heuristic. Writing out Eq. (61) yields

$$n_i = N^{\text{shots}} \frac{\sqrt{\sum_{j,j'=1}^{m_i} c_{i,j} c_{i,j'} \text{Cov}(P_{i,j}, P_{i,j'})}}{\sum_{k=1}^N \sqrt{\sum_{j,j'=1}^{m_k} c_{k,j} c_{k,j'} \text{Cov}(P_{k,j}, P_{k,j'})}}. \quad (63)$$

Borrowing an idea from Ref. [9], we replace the covariances in Eq. (63) by their average over the spherical measure, which is given by $\mathbb{E}[\text{Cov}[P, P']] = \delta_{P,P'}/(1 + 2^{-n})$ for all commuting operators $P, P' \in \{I, X, Y, Z\}^{\otimes n}$ (see Ref. [6, Thm. 3] and Ref. [9, Eq. (45)]). This yields our a-priori shot-allocation heuristic, which only depends on the observable O and its Pauli grouping,

$$n_i^{\text{heuristic}} = \frac{N^{\text{shots}} \sqrt{m_i \sum_{j=1}^{m_i} c_{i,j}^2}}{\sum_{k=1}^N \sqrt{m_k \sum_{j=1}^{m_k} c_{k,j}^2}}. \quad (64)$$

Note that Eq. (64) recovers the asymptotically-optimal shot allocation $n_i \propto |c_i|$ in the ungrouped case [48, 49]. We leave investigating the performance of our heuristic shot allocation strategy as an open problem.

V. PAULI GROUPING ALGORITHMS

In quantum simulation experiments, it is necessary to estimate the expectation value $\langle O \rangle$ of a given observable O [3]. This can be accomplished, for instance, by first measuring the Pauli operators P_1, \dots, P_M occurring in the decomposition of O , and then computing $\langle O \rangle$ in a classical post-processing step via Eq. (1). Here, the first step can be carried out more efficiently if multiple Pauli operators are measured simultaneously. Prior to an experiment, it is thus desirable to group P_1, \dots, P_M into jointly-measurable collections; we refer to this challenge as the *Pauli-grouping problem*. In July 2019, three groups of researchers pointed out in a number of pre-prints ([arXiv:1907.03358](#), [arXiv:1907.07859](#), [arXiv:1907.09386](#), and [arXiv:1907.13623](#)) that the Pauli-grouping problem is equivalent to the clique-cover problem of the commutativity graph of O and, dually, to the coloring problem of the non-commutativity graph of O [5–8]. This important insight implies that the number N of jointly-measurable collections is upper-bounded by the chromatic number of the non-commutativity graph of O . Furthermore, groupings that minimize N were investigated in these seminal papers. Later, it was recognized that $\langle O \rangle$ can be estimated even more efficiently if not only N is kept small, but also if the coefficients c_i in Eq. (1) are taken into account [9].

Algorithm 1

Parallel algorithm for grouping a list of Pauli operators, `paulis`, into a list of collections, `out`. Every collection in `out` can be measured with a hardware-tailored (HT) readout circuit as in Fig. 1 of the main text. Hereby, a pre-defined list of `subgraphs` specifies templates for the readout circuits. Note that `subgraphs` must contain $\Gamma = 0$ to ensure that the algorithm will terminate. As in Sorted Insertion [9], the operators in `paulis` are sorted with respect to their coefficients in Eq. (1). To construct HT circuits, any solver from Sec. II can be exploited. If, for a given subgraph Γ and a collection `col` of Pauli operators, the selected solver succeeds in constructing a circuit, we write `ht_measurable(col, Γ) = True`.

```

1: out  $\leftarrow \emptyset$ ;
2: s  $\leftarrow \text{length}(\text{subgraphs})$ ;
3: remaining_paulis  $\leftarrow \text{paulis}$ ;
4: while remaining_paulis  $\neq \emptyset$  do
5:   main_pauli  $\leftarrow \text{remaining\_paulis}[0]$ ;
6:   temp_collections  $\leftarrow [\emptyset, \dots, \emptyset]$ ;  $\triangleright$  list of length s
7:   for i in [0, ..., s-1] do  $\triangleright$  parallel loop
8:      $\Gamma \leftarrow \text{subgraphs}[i]$ ;
9:     if ht_measurable([main_pauli],  $\Gamma$ ) then
10:      col  $\leftarrow [\text{main\_pauli}]$ ;
11:      for pauli in remaining_paulis do
12:        if ht_measurable(col  $\cup$  [pauli],  $\Gamma$ ) then
13:          col  $\leftarrow \text{col} \cup [\text{pauli}]$ ;
14:        end if
15:      end for
16:      temp_collections[i]  $\leftarrow \text{col}$ ;
17:    end if
18:  end for
19:  best_collection  $\leftarrow \text{best}(\text{temp\_collections})$ ;
20:  remaining_paulis.remove(best_collection);
21:  out.append(best_collection);
22: end while
23: return out;
```

In this section, we adapt the *Sorted Insertion* (SI) algorithm of Ref. [9] to our purposes. Thus, we briefly review it now. First, the Pauli operators P_1, \dots, P_M are *sorted* such that $|c_1| \geq |c_2| \geq \dots \geq |c_M|$. Then, P_1 is assigned to a first jointly-measurable collection. If P_2 commutes with P_1 , it is assigned to this first collection as well; otherwise, a second collection is created. Similarly, one proceeds with $j \in \{3, \dots, M\}$ by iterating through the existing collections until one is found into which P_j can be *inserted*. In the original version of SI, the insertion condition is given by general commutativity (GC). Accordingly, each of the resulting collections can, in principle, be measured by applying a diagonalization circuit, followed by a readout of the individual qubits. In general, however, these circuits are too demanding for near-term applications (see e.g., Tab. III in Sec. VIB). To remedy this deficiency, one can replace the GC condition with qubit-wise commutativity (QWC). We refer to this minor modification of SI as SI-QWC. The corresponding readout circuits are minimal in their hardware demands; however, only tensor product bases can be measured.

By integrating our approach for the construction of hardware-tailored (HT) readout circuits (see Sec. II), we can improve upon SI-QWC without sacrificing hardware-efficiency. As a straightforward modification of SI, one could simply replace the GC insertion condition by HT-measurability. For the HT Pauli groupings computed throughout this work, however, we implement Algorithm 1, which has the advantage of parallel executability. As in SI, we sort the operators P_1, \dots, P_M by the magnitude of their coefficients. In every iteration of the outer loop (lines 4–22), which is repeated until all operators have been assigned to a jointly-HT-measurable collection, we construct a readout circuit for the operator P_{main} (line 5) that is leading the list of still-unassigned, remaining Pauli operators. Hereby, we strive for a readout circuit that also works for other remaining Pauli operators. To find the circuit with the “best” collection, we loop over a pre-specified list of subgraphs Γ of the connectivity graph Γ_{con} (lines 7–18); this can be executed in parallel. For every subgraph Γ , we first attempt the construction of a Γ -based circuit (see main text, Fig. 1) that diagonalizes P_{main} (line 9). For this, we exploit one of the solvers from Sec. II. By varying the hyperparameters of the selected solver, one can flexibly adjust Algorithm 1; we explore this possibility in Sec. VI. If, for a given Γ , the solver succeeds in constructing a HT readout circuit for P_{main} , we start a collection (line 10) of operators that can be measured with a circuit based on Γ . Then, we successively extend this collection by iterating through the list of remaining operators (lines 11–15) and adding those Pauli operators which can be measured with a Γ -based readout circuit as well. Hereby, we allow updating the single-qubit Clifford-gate layer (SCL) of the Γ -based readout circuit. At this point, Algorithm 1 can be sped up by checking if, by chance, Eq. (6) holds for the previous SCL and the new Pauli operator. In general, however, new SCLs are computed by re-applying the solver to the growing collection of operators. Since the list of remaining Pauli operators is sorted, the collection prioritizes operators P_i for which $|c_i|$ is large; this idea is borrowed from Ref. [9]. By doing all of this, we create one collection for every subgraph Γ under consideration. For those subgraphs Γ for which P_{main} does not admit a Γ -based readout circuit (or the solver fails finding it), the corresponding collection stays empty (line 6), i.e., we simply skip Γ . Among the list of the constructed collections $\{P_{i_1}, \dots, P_{i_m}\}$ containing $P_{i_1} \equiv P_{\text{main}}$, we regard the one which maximizes a suitable value function, e.g.,

$$\text{value}_1(\{P_{i_1}, \dots, P_{i_m}\}) = m \quad (65)$$

$$\text{or } \text{value}_2(\{P_{i_1}, \dots, P_{i_m}\}) = m \sum_{k=1}^m c_{i_k}^2 \quad (66)$$

as the best collection (line 19). In the final Pauli grouping produced by Algorithm 1, the operator P_{main} has to occur only once; we select the best collection (line 21). Finally, we remove the operators in the best collection from the list of remaining Pauli operators (line 20). All of these

steps are repeated until all operators have been grouped into a jointly-HT-measurable collection.

The efficiency of Algorithm 1 depends on the solver that is exploited for constructing the readout circuits. In Sec. VI, we demonstrate that the restricted solver from Sec. II C can construct enough readout circuits to ensure both a polynomial runtime and a high-quality HT Pauli grouping. We discovered an important fact while constructing numerous HT Pauli groupings: in the beginning, the (“best”) collections are comparatively large, but over the course of Algorithm 1 they often become smaller and smaller. Since the important Pauli operators P_i , for which $|c_i|$ is large, are assigned first, it is likely that a considerable amount of computational time can be saved (without greatly deteriorating the result) if, eventually, SI-QWC takes over from Algorithm 1. Investigating this idea in detail is beyond the scope of this work but certainly deserves further investigation.

Note that the objective function in Eq. (66), whose definition is motivated by the enumerator of Eq. (61) in Sec. IV, slightly outperforms the one in Eq. (65) (see Tab. IV in Sec. VI C). In future research, one could study in more detail how the quality of HT Pauli groupings is impacted by the choice of these and other objective functions, e.g., one that penalizes low-fidelity CZ-gates. Another promising use case for such objective functions is the exploration of the set of subgraphs $\Gamma \subset \Gamma_{\text{con}}$; throughout this work, we simply iterate through a pre-specified subset of subgraphs. It is worth investigating if this can be made more efficient, e.g., via simulated annealing or Monte Carlo methods.

VI. EXAMPLES OF HARDWARE-TAILORED PAULI GROUPINGS

In this section, we demonstrate the practicality of our theoretical framework for the construction of hardware-tailored diagonalization circuits. Following Ref. [9], we quantify the quality of a Pauli grouping for an observable O with the corresponding *estimated shot reduction*

$$\hat{R} = \left(\frac{\sum_{i=1}^N \sum_{j=1}^{m_i} |c_{i,j}|}{\sum_{i=1}^N \sqrt{\sum_{j=1}^{m_i} |c_{i,j}|^2}} \right)^2, \quad (67)$$

where $c_{i,1}, \dots, c_{i,m_i}$ are the coefficients in front of the operators in the i -th collection of simultaneously diagonalizable Pauli operators, i.e.,

$$O = \sum_{i=1}^N O_i = \sum_{i=1}^N \sum_{j=1}^{m_i} c_{i,j} P_{i,j}. \quad (68)$$

Note that \hat{R} is believed to approximate the operationally meaningful reduction $R = N_{\text{shots}}^{\text{IPM}} / N_{\text{shots}}^{\text{GPM}}$ in the number of shots needed to reach a targeted statistical accuracy (in the absence of experimental errors). Hereby, R quantifies the shot reduction that is obtained when every operator O_i in Eq. (68) is measured with a single readout

circuit (GPM) instead of measuring every Pauli operator $P_{i,j}$ individually (IPM). In both cases, the shot budget is hereby assumed to be optimally distributed among the readout circuits (see Sec. IV for more details). Note that both R and \hat{R} are independent of the anticipated finite-sample variance ϵ^2 . Since the true shot reduction R is state dependent and, therefore, difficult to evaluate, \hat{R} is a more applicable figure of merit.

We showcase that our Pauli grouping algorithm introduced in Sec. V performs well for the following paradigmatic problems: random Hamiltonians in Sec. VI A, the one-dimensional Hubbard model in Sec. VI B, selected molecules in Sec. VI C, and hydrogen chains in Sec. VI D.

A. Random Hamiltonians

Here we provide background information about Fig. 2 from the main text, in which the estimated shot reduction ratio $\hat{R}_{\text{HT}} / \hat{R}_{\text{TPB}}$ for random Hamiltonians is shown. For every choice of the numbers n and M of qubits and Pauli operators, one sample set containing 20 random Hamiltonians is created. Then, we apply the Sorted Insertion (SI) algorithm, the SI-QWC algorithm, and two variants of the HT Pauli grouping algorithm introduced in Sec. V. For the latter, we tailor the diagonalization circuits to a linear hardware connectivity. The time t that it takes to compute a Pauli grouping depends on n , M , and the selected method for constructing the single-qubit Clifford gates; recall Sec. II. In Fig. 7, we observe an exponential scaling of t in n , irrespective of M and the Clifford-construction method. On the one hand, the exponential scaling can be attributed to the Clifford-construction subroutine; on the other hand, it is due to our choice to loop through the exhaustive list of all 2^{n-1} subgraphs of the n -qubit connectivity graph in every iteration of our Pauli grouping algorithm. Note that, in this subsection, we do not yet use the efficient version of our algorithm because, at this point, we cannot decide whether or not restricting to a polynomially large subset of subgraphs leads to suboptimal Pauli groupings. Here, we only establish that the exhaustive numerical solver performs equally well as the exhaustive algebraic solver. While the latter turns out to be slower than the former, it never fails to identify suitable circuit templates. Later, in Fig. 10, we will see that the efficient algebraic solver can construct a HT Pauli grouping with the same quality as the exhaustive solvers but much faster.

In Fig. 7, we observe that the computation time t scales worst for the algebraic method (dark, dotted lines) from Sec. II B, for which it surpasses the one-hour barrier for $M = 100$ Pauli operators (brown diamonds) already at $n = 9$ qubits. The numerical optimization method (bright, solid lines) from Sec. II D, on the other hand, requires one minute for the same task, and it only exceeds one hour at $n = 14$ qubits. It is unsurprising that the numerical method is faster as it leverages state-of-the-art optimization subroutines, whereas the algebraic

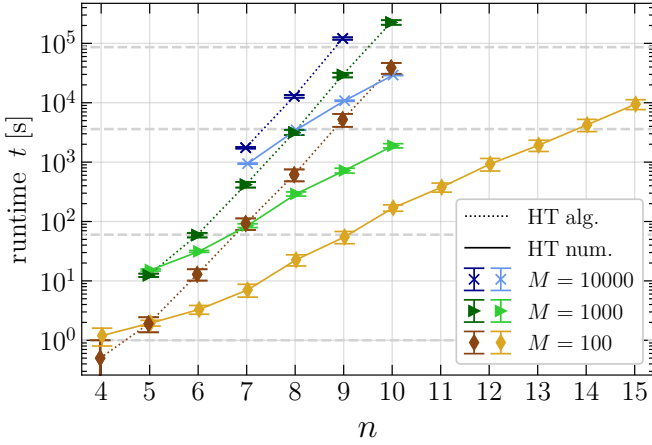


FIG. 7. Required time t for computing the HT Pauli groupings from Fig. 2 (see main text) as a function of the number n of qubits. The approximately optimal HT Pauli groupings were obtained via an exhaustive search over all subgraphs of the n -vertex path graph. For every subgraph, the single-qubit Clifford gates were constructed by solving the corresponding system of algebraic equations either based on Gaussian elimination (HT alg.) or through numerical optimization (HT num.). Colors and markers correspond to the number M of Pauli operators, while shade and line style indicate the utilized Clifford-construction method. Dashed, horizontal lines mark the 1 second, 1 minute, 1 hour, and 1 day barriers. The computations were carried out on an 18 core Intel Xeon CPU E5-2697 v4 @2.30GHz device.^a

^a Intel and Intel Xeon are trademarks or registered trademarks of Intel Corporation or its subsidiaries in the United States and other countries.

solver was first introduced in this work. Since the error bars in Fig. 7 are small, the time it would take to apply our algorithm to a new random Hamiltonian is highly predictable.

While Fig. 2 (see main text) only shows the ratio $\hat{R}_{\text{HT}}/\hat{R}_{\text{TPB}}$, we depict the individual values of \hat{R} in Fig. 8. There, \hat{R}_{GC} is the estimated shot reduction for the Pauli groupings into general commuting (GC) sets, which were obtained by applying the SI algorithm. Similarly, \hat{R}_{TPB} corresponds to the Pauli grouping into tensor product bases (TPBs) computed with the SI-QWC algorithm. As expected, we observe $\hat{R}_{\text{GC}} > \hat{R}_{\text{HT}} > \hat{R}_{\text{TPB}}$ for every fixed value of n and M . Furthermore, \hat{R} increases (decreases) with M (with n) if n (if M) is held constant. To understand the reason for this, recall that every Pauli grouping method for $O = \sum_{i=1}^M c_i P_i$ partitions the set $\mathcal{X} = \{P_1, \dots, P_M\}$ into a disjoint union

$$\mathcal{X} = \bigcup_{i=1}^N \mathcal{X}_i \quad (69)$$

of subsets $\mathcal{X}_i = \{P_{i,1}, \dots, P_{i,m_i}\}$ as in Eq. (68). Hereby, all operators in a given subset \mathcal{X}_i can be simultaneously diagonalized with a general (GC), hardware-tailored (HT), and single-qubit (TPB) Clifford circuit, re-

spectively. We expect that more shots can be saved (bigger \hat{R}) if more operators are simultaneously measurable (bigger m_i). Note that this rule of thumb is only valid because presorting the operators in \mathcal{X} by the magnitude of their coefficients ensures that pathological Pauli groupings with highly suboptimal values of \hat{R} are avoided [9]. As we show in Fig. 9, the average size $\bar{m}_i = M/N$ of the subsets \mathcal{X}_i indeed reproduces the behavior of \hat{R} remarkably well. The curves of \bar{m}_i and, therefore, \hat{R} can be explained by graph-theoretical means. Consider the two graphs $G_{\text{GC}}^{\text{not}}$ and $G_{\text{QWC}}^{\text{not}}$, whose vertex sets are both given by $\mathcal{X} = \{P_1, \dots, P_M\}$. The difference between the two graphs is the set of edges. As the names suggest, two vertices $P_i, P_j \in \mathcal{X}$ are connected by an edge in $G_{\text{GC}}^{\text{not}}$ (in $G_{\text{QWC}}^{\text{not}}$) if the operators P_i and P_j are not GC (QWC). In other words, P_i and P_j are *disconnected* if the set $\{P_i, P_j\}$ is GC (QWC). By definition, a set of operators is GC (QWC) if and only if the same is true for all of its subsets of size two. Therefore, the GC (QWC) subsets $\mathcal{X}_i \subset \mathcal{X}$ are given by the completely disconnected subsets of the vertex set of $G_{\text{GC}}^{\text{not}}$ ($G_{\text{QWC}}^{\text{not}}$), i.e., those which do not contain a single pair of vertices sharing an edge. Thus, a Pauli grouping as in Eq. (69) is what in graph theory is known as a *coloring*: a color is assigned to every vertex in a way that neighboring vertices have different colors. It has been pointed out before that finding a coloring of $G_{\text{GC}}^{\text{not}}$ (of $G_{\text{QWC}}^{\text{not}}$) yields a Pauli grouping of \mathcal{X} into subsets \mathcal{X}_i that can be simultaneously diagonalized with general (with single-qubit) Clifford circuits [5–8]. Unfortunately, this approach cannot be easily generalized to partition \mathcal{X} into subsets \mathcal{X}_i that can be simultaneously diagonalized with HT circuits (see main text, Fig. 1). Consider, for example, the $M = 3$ operators $P_1 = XXZI$, $P_2 = YXYY$, and $P_3 = ZZZZ$ on $n = 4$ qubits whose hardware connectivity is given by the adjacency matrix

$$\Gamma = \begin{bmatrix} 0 & 1 & 1 & 1 \\ 1 & 0 & 0 & 0 \\ 1 & 0 & 0 & 0 \\ 1 & 0 & 0 & 0 \end{bmatrix}. \quad (70)$$

For the sets $\{P_1, P_2\}$, $\{P_1, P_3\}$, and $\{P_2, P_3\}$, there exist HT diagonalization circuits but not for $\{P_1, P_2, P_3\}$. Because of obstructions like this, we focus on explaining the GC- and TPB-curves in Fig. 9 and are satisfied with pointing out that, intuitively, the HT-curves should lie between them, which is indeed the case. The working principle of all three here-considered Pauli grouping algorithms is to grow the subsets \mathcal{X}_i by adding one Pauli operator at a time until no further operators can be added. In this way, the number N of resulting subsets is kept so small that it can approximately attain the *chromatic number* $\chi(G)$, which is defined as the minimal number of colors needed in a coloring of a graph G . This yields

$$\bar{m}_i = \frac{M}{N} \approx \frac{M}{\chi(G)}, \quad (71)$$

where $G = G_{\text{GC}}^{\text{not}}$ or $G = G_{\text{QWC}}^{\text{not}}$, depending on the prob-

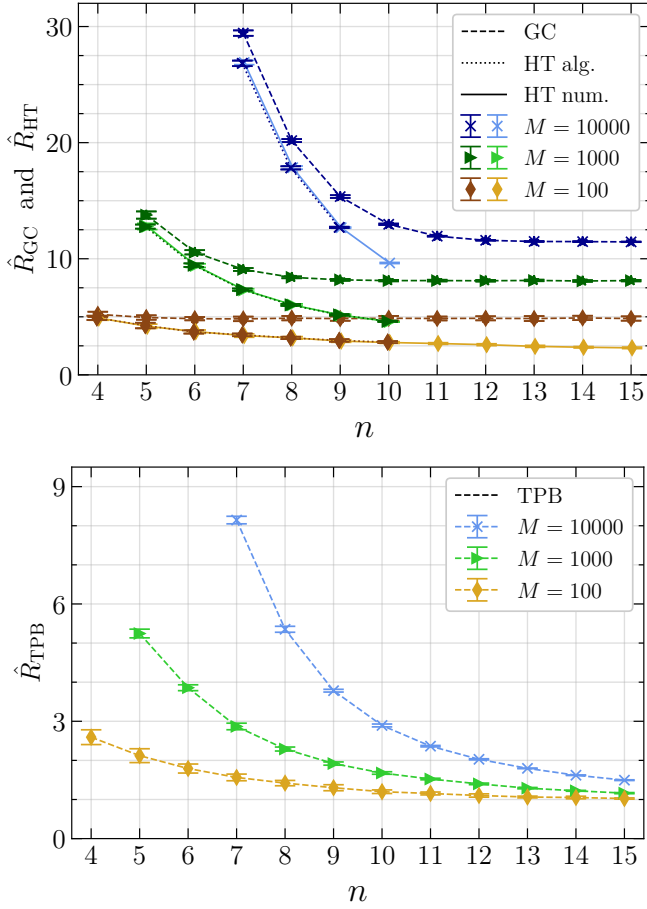


FIG. 8. Estimated shot reduction \hat{R} for various Pauli groupings of the same random Hamiltonians as in Fig. 2 (see main text) as a function of the number n of qubits. Colors and markers correspond to the number M of Pauli operators, while shade and line style indicate the utilized method. **(top)** GC (dark, dashed), HT alg. (dark, dotted), and HT num. (bright, solid). **(bottom)** TPB (bright, dashed).

lem. For every random Hamiltonian $O = \sum_{i=1}^M c_i P_i$, the vertex set $\mathcal{X} = \{P_1, \dots, P_M\}$ of G is created by drawing M operators from $\{I, X, Y, Z\}^{\otimes n}$ at random without replacement. Within the limit of large qubit numbers $n \gg \log_4(M)$, it is irrelevant that the operators are picked without replacement, and it is justifiable to assume that $G_{\text{GC}}^{\text{not}}$ ($G_{\text{QWC}}^{\text{not}}$) is an Erdős-Rényi random graph with M vertices and a vertex-independent edge probability of $\frac{1}{2}$ (of approximately 1) because the probability that two random Pauli operators commute (on every qubit) is given by $\frac{1}{2}$ (is exponentially suppressed in n) [7]. In particular, $\chi(G_{\text{QWC}}^{\text{not}})$ converges to the chromatic number $\chi(K_M) = M$ of the complete graph K_M with M vertices. Therefore, Eq. (71) yields

$$\lim_{n \rightarrow \infty} \bar{m}_{i, \text{TPB}} = 1, \quad (72)$$

which implies $\hat{R}_{\text{TPB}} \rightarrow 1$ and explains the asymptotic behavior of the curves in the lower panel of Fig. 9 and Fig. 8,

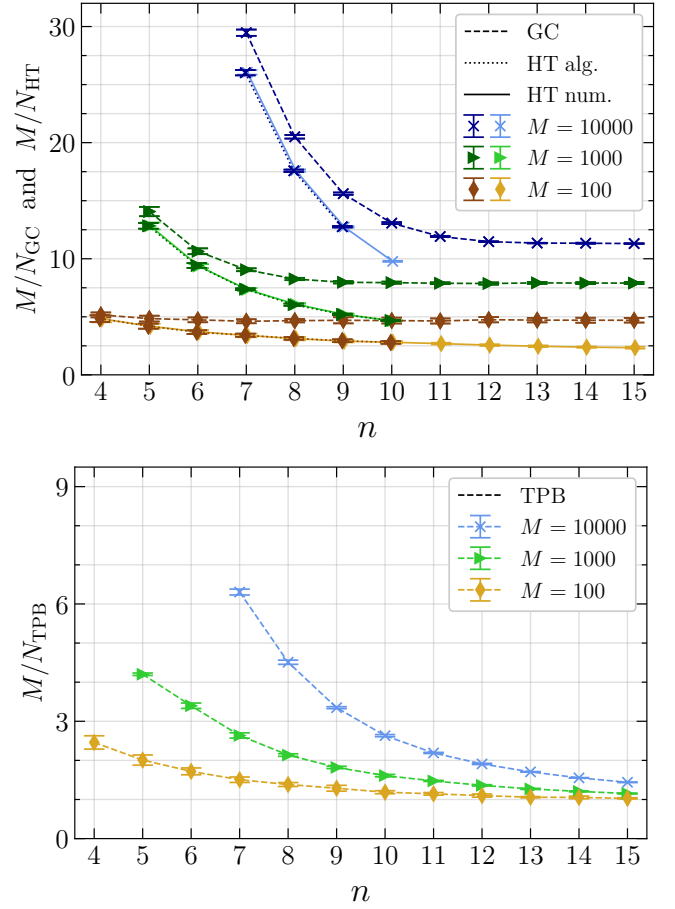


FIG. 9. Average number $M/N = \bar{m}_i$ of commuting Pauli operators $P_{i,1}, \dots, P_{i,m_i}$, which constitute O_i in Eq. (68), for various Pauli groupings of the same random Hamiltonians as in Fig. 2 (see main text) as a function of the number n of qubits. Colors and markers correspond to the number M of Pauli operators, while shade and line style indicate the utilized method.

respectively. Likewise, $\chi(G_{\text{GC}}^{\text{not}})$ converges to the chromatic number of an M -vertex, $\frac{1}{2}$ -edge-probability Erdős-Rényi random graph G_{ran} , which (with high probability) is given by $\chi(G_{\text{ran}}) = M/(\gamma(M) + o(1))$, where

$$\gamma(M) = 2 \log_2(M) - 2 \log_2(\log_2(M)) - 2 \log_2(2) \quad (73)$$

was introduced in Ref. [50]. Therefore, we expect that the asymptotes

$$\lim_{n \rightarrow \infty} \bar{m}_{i, \text{GC}} \approx \gamma(M) + o(1) \quad (74)$$

are logarithmically growing in the number M of Pauli operators. Now that we understand its asymptotic behavior, let us discuss why \bar{m}_i increases when n is decreased while M is held constant. The key difference between G_{ran} and $G_{\text{GC}}^{\text{not}}$ (K_M and $G_{\text{QWC}}^{\text{not}}$) is that G_{ran} can have (K_M only has) vertices $P \in \mathcal{X}$ whose degree

$$\deg_G(P) = |\{P' \in \mathcal{X} \mid P, P' \text{ share an edge in } G\}| \quad (75)$$

reaches the trivial bound $\deg_G(P) \leq M - 1$, whereas for $G_{\text{GC}}^{\text{not}}$ ($G_{\text{QWC}}^{\text{not}}$) it cannot exceed the total number of operators $P' \in \{I, X, Y, Z\}^{\otimes n}$ that do not commute (qubit-wise) with P . In other words,

$$\deg_G(P) \leq \begin{cases} 4^n/2 & \text{if } G = G_{\text{GC}}^{\text{not}} \\ 4^n - 2^k 4^{n-k} & \text{if } G = G_{\text{QWC}}^{\text{not}}, \end{cases} \quad (76)$$

where $k = \text{wt}(P)$ is the *Pauli weight* of P , i.e., its number of non-identity tensor factors. In combination with Brooks' theorem,

$$\chi(G) \leq 1 + \max_{P \in \mathcal{X}} \deg_G(P), \quad (77)$$

Ineq. (76) causes the chromatic number of $G_{\text{GC}}^{\text{not}}$ ($G_{\text{QWC}}^{\text{not}}$) to shrink when n is decreased. From Eq. (71), this in turn gives room for \bar{m}_i to grow, which is indeed what we observe in Fig. 9. Finally, let us explain the dependence of \bar{m}_i on M for fixed n . Assume we have a Pauli grouping as in Eq. (69) and we start to reduce the value of M by randomly removing some operators from \mathcal{X} . It is more likely that these operators are removed from different subsets \mathcal{X}_i (which decreases m_i) than it is that one of the subsets is emptied completely (which would decrease $N = M/\bar{m}_i$). This is why \bar{m}_i increases with M in Fig. 9. For example, the average sizes of GC subsets on $n = 7$ qubits are given by $\bar{m}_i(M = 10^2) \approx 5.2$, $\bar{m}_i(M = 10^3) \approx 14.1$, and $\bar{m}_i(M = 10^4) \approx 29.5$.

Although our graph-theoretical arguments break down in the case of HT Pauli groupings, we see in Fig. 8 that, qualitatively, \hat{R}_{HT} behaves like \hat{R}_{GC} and \hat{R}_{TPB} . In conclusion, readout circuits tailored to a linear hardware connectivity consistently offer an advantage over TPBs. We expect that \hat{R}_{HT} would be even larger for a two-dimensional hardware connectivity, which is typical for super- and semiconducting quantum computers, and we leave an investigation of how close $\hat{R}_{\text{HT},2\text{D}}$ comes to \hat{R}_{GC} as an open problem.

B. One-Dimensional Hubbard Model

The emerging field of quantum simulation is still in its infancy. We expect that in order to reach quantum advantage it will be necessary to reveal and eradicate systematic errors in near-term implementations of quantum algorithms. This problem can be addressed while experimenting with quantum simulations of the Hubbard model, which describes the interaction of electrons residing at discrete lattice sites. The Hubbard model has several features that qualify it as an attractive candidate for early-stage benchmarking experiments:

- The required number of qubits is $n = 2L$, where L is the number of lattice sites. Thus, the problem size can be varied in small steps.
- Experimental demands on hardware connectivity, circuit depth, and number of circuit executions (“shots”) can scale moderately with L [51, 52].

- Simulating the Hubbard model in either its real- or momentum-space representation provides two inequivalent approaches to the same physical system. Disagreeing simulation results might help to identify and subsequently remove systematic errors.
- The theory of the one-dimensional Hubbard model is remarkably well understood [53]. Developing the ability to experimentally reproduce its analytical solutions would be a significant step towards establishing confidence in the correctness of non-trivial quantum simulations.
- We expect that certain techniques for successfully simulating the one-dimensional Hubbard model (not yet fully developed) will be generalizable to the two-dimensional case eventually. Since the latter eludes classical treatments, simulating it on a reliable quantum computer has the potential to enable insights into new physics [54].

The purpose of this section is twofold: as a sanity check of our new Pauli grouping algorithm, we apply it to the (almost trivial) real-space Hubbard Hamiltonians and compare the results to straightforward analytical Pauli groupings. Second, we explore the trade-off between pre-processing time and estimated shot reduction by applying different variants of our algorithm to the (less trivial) momentum-space Hubbard Hamiltonians.

The Hamiltonian $\hat{H} = \hat{T} + U\hat{D}$ of the periodic, one-dimensional Hubbard model consists of a kinetic term

$$\hat{T} = -t \sum_{x=1}^L \sum_{\sigma \in \{\uparrow, \downarrow\}} \hat{a}_{x,\sigma}^\dagger \hat{a}_{x+1 \bmod L, \sigma} + \text{h.c.}, \quad (78)$$

which describes the hopping $t \geq 0$ of electrons with spin σ from site x to a neighboring site, and a potential term

$$U\hat{D} = U \sum_{x=1}^L \hat{n}_{x,\uparrow} \hat{n}_{x,\downarrow}, \quad (79)$$

which accounts for repulsive Coulomb energies $U \geq 0$ stemming from doubly-occupied lattice sites. Hereby, $\hat{a}_{x,\sigma}^\dagger$ and $\hat{n}_{x,\sigma} = \hat{a}_{x,\sigma}^\dagger \hat{a}_{x,\sigma}$ are fermionic creation and number operators, respectively. In the atomic limit ($t \rightarrow 0$), the Hubbard Hamiltonian is diagonal in the number-operator eigenbasis (Wannier basis). In the tight-binding limit ($U \rightarrow 0$), however, it is convenient to introduce new fermionic modes $\hat{c}_{k_j,\sigma}^\dagger = \frac{1}{\sqrt{L}} \sum_{x=1}^L e^{-ik_j x} \hat{a}_{x,\sigma}^\dagger$ with lattice momentum $k_j = 2\pi j/L$, which is defined modulo 2π , and spin σ as this transforms Eq. (78) into

$$\hat{T} = \sum_{j=1}^L \sum_{\sigma \in \{\uparrow, \downarrow\}} \epsilon_{k_j} \hat{c}_{k_j,\sigma}^\dagger \hat{c}_{k_j,\sigma}, \quad (80)$$

where $\epsilon_k = -2t \cos(k)$ is the energy dispersion relation of non-interacting ($U = 0$) fermions. For $U \neq 0$, however, the Hubbard Hamiltonian is no longer diagonal in the

Fourier basis, as the potential-energy term in Eq. (79) is converted into

$$U\hat{D} = \frac{U}{L} \sum_{i,j,l=1}^L \hat{c}_{k_i-k_l,\uparrow}^\dagger \hat{c}_{k_j+k_l,\downarrow}^\dagger \hat{c}_{k_j,\downarrow} \hat{c}_{k_i,\uparrow}. \quad (81)$$

Physically, Eq. (81) describes scattering events in which a spin-up electron with lattice momentum k_i transfers l quanta of lattice momentum to a spin-down electron with lattice momentum k_j .

Prior to a simulation of the Hubbard model on a quantum computer, the electronic modes (in either real or momentum space) need to be mapped to qubits. Here, we consider the block-spin Jordan-Wigner (JW) mapping [3], which is given by

$$\hat{a}_{x,\sigma} = |0\rangle\langle 1|^{(\delta_{\sigma,\downarrow}L+x)} \prod_{j=1}^{\delta_{\sigma,\downarrow}L+x-1} Z^{(j)}, \quad (82)$$

where the notation $|0\rangle\langle 1|^{(\delta_{\sigma,\downarrow}L+x)}$ stands for the operator $|0\rangle\langle 1| = \frac{1}{2}(X + iY)$ acting on qubit $\delta_{\sigma,\downarrow}L + x$ and similarly for $Z^{(j)}$. In particular, qubit $\delta_{\sigma,\downarrow}L + x$ is in state $|0\rangle$ (or $|1\rangle$) if the simulated electronic mode on site x with spin σ is empty (or occupied). Because $\hat{n} = |1\rangle\langle 1| = \frac{1}{2}(I - Z)$, the potential term in Eq. (79) is equal to

$$U\hat{D} = \frac{LU}{4} I^{\otimes 2L} + \frac{U}{4} \sum_{x=1}^L \left[Z^{(x)} Z^{(L+x)} - Z^{(x)} - Z^{(L+x)} \right]. \quad (83)$$

Furthermore, inserting Eq. (82) into Eq. (78) yields

$$\begin{aligned} \hat{T} = & -\frac{t}{2} \sum_{x=1}^{L-1} \left[X^{(x)} X^{(x+1)} + Y^{(x)} Y^{(x+1)} \right. \\ & \left. + X^{(L+x)} X^{(L+x+1)} + Y^{(L+x)} Y^{(L+x+1)} \right] \\ & - \frac{t}{2} (X^{(1)} X^{(L)} + Y^{(1)} Y^{(L)}) \prod_{j=2}^{L-1} Z^{(j)} \\ & - \frac{t}{2} (X^{(L+1)} X^{(2L)} + Y^{(L+1)} Y^{(2L)}) \prod_{j=L+2}^{2L-1} Z^{(j)}. \end{aligned} \quad (84)$$

The $M = 7L$ non-trivial Pauli-operators occurring in the block-spin JW-encoded, real-space Hubbard Hamiltonian $\hat{H} = \hat{T} + U\hat{D}$ can be grouped into a constant number of $N_{\text{TPB}} = 5$ tensor product bases (TPBs): $Z^{\otimes 2L}$, $X^{\otimes 2L}$, $Y^{\otimes 2L}$, $(X \otimes Z^{\otimes L-2} \otimes X)^{\otimes 2}$, and $(Y \otimes Z^{\otimes L-2} \otimes Y)^{\otimes 2}$. In the notation of Eq. (68), the first TPB contains all $m_1 = 3L$ operators in Eq. (83) having coefficient $c_{1,j} = \pm \frac{U}{4}$. The coefficients in front of the Pauli operator in the other four TPBs are all given by $c_{2,j} = \dots = c_{5,j} = -\frac{t}{2}$ and there are $m_2 = m_3 = 2L - 2$ ($X^{\otimes 2L}$ and $Y^{\otimes 2L}$),

$m_4 = m_5 = 2$ of them. Inserting this into Eq. (67) yields

$$\begin{aligned} \hat{R}_{\text{TPB}} &= \left(\frac{\frac{3LU}{4} + \frac{4Lt}{2}}{\sqrt{3L}\frac{U}{4} + 2\sqrt{(2L-2)}\frac{t}{2} + 2\sqrt{2}\frac{t}{2}} \right)^2 \\ &= \left(\frac{3u+2}{\sqrt{3}u + \sqrt{2-\frac{2}{L}} + \sqrt{\frac{2}{L}}} \right)^2 L, \end{aligned} \quad (85)$$

where we have introduced the intrinsic, dimensionless coupling constant $u = \frac{U}{4t}$ [53]. In Eq. (85), we see that \hat{R}_{TPB} scales almost linearly in L for a large number L of lattice sites (or for large u), where the proportionality constant is equal to 2 and 3 in the tight-binding ($u \rightarrow 0$) and atomic ($u \rightarrow \infty$) limit, respectively. This (linear) dependence reflects the linear reduction of the number of readout circuits from $N_{\text{IPM}} = 7L$ for individual Pauli measurements to $N_{\text{TPB}} = 5$ for TPBs.

Next, we compare the analytical Pauli grouping from above with two algorithmically-obtained ones: hardware-tailored (HT) and general commuting (GC). We assume $u > \frac{1}{2}$, i.e., the Z -type operators in Eq. (83) are at the top of the sorted list of Pauli operators. In consequence, our HT algorithm of Sec. V and the SI algorithm of Ref. [9] both select the computational basis ($Z^{\otimes 2L}$) as the first collection of jointly-measurable Pauli operators. The order of the remaining operators in the “sorted” list is arbitrary as all coefficients have the same value ($-\frac{t}{2}$). For simplicity, we consider the ordering provided by Qiskit nature [36]. Then, the remaining list starts with $X \otimes Z^{\otimes L-2} \otimes X \otimes I^{\otimes L}$ and $Y \otimes Z^{\otimes L-2} \otimes Y \otimes I^{\otimes L}$. Although these two operators commute, it is not possible to tailor a readout circuit for both of them to a linear hardware connectivity, and only the SI algorithm groups them together. Our algorithm, however, finds that $I \otimes Y \otimes Y \otimes I^{\otimes 2L-3}$ can be simultaneously HT-diagonalized with $X \otimes Z^{\otimes L-2} \otimes X \otimes I^{\otimes L}$. For $L = 3$, only $I^{\otimes 3} \otimes X \otimes Z \otimes X$ and $I^{\otimes 4} \otimes Y \otimes Y$ can be added as well, yielding a collection of $m_2 = 4$ jointly-measurable Pauli operators. For $L \geq 4$, $I \otimes X \otimes X \otimes I^{\otimes 2L-3}$ can also be added; for $L \geq 5$, $I^{\otimes 3} \otimes Y \otimes Y \otimes I^{\otimes 2L-5}$ also etc. Our algorithm similarly proceeds with the remaining Pauli operators. We summarize the final results in Tab. II, where we assume $U = 4$ and $t = 1$ to obtain concrete values of \hat{R} . Here, we restrict to $L \leq 5$ qubits as this allows us to compute approximately-optimal HT Pauli groupings using the exhaustive algebraic solver from Sec. II B applied to the full list of all subgraphs. Our algorithm accomplishes grouping the Pauli operators into only $N_{\text{HT}} = 4$ jointly-measurable collections, while the SI algorithm even achieves $N_{\text{GC}} \in \{3, 4\}$. We see that \hat{R}_{HT} is comparable to \hat{R}_{GC} and slightly outperforms \hat{R}_{TPB} . Therefore, we can state that our algorithm successfully passes a sanity check of producing equally good Pauli groupings as SI and SI-QWC when applied to real-space Hubbard Hamiltonians. Note that, although our algorithm is constrained to HT circuits, $\hat{R}_{\text{HT}} > \hat{R}_{\text{GC}}$ is possible ($L = 3$) because the SI algorithm also only

TABLE II. Pauli groupings of the real-space Hubbard model with L lattice sites and $u = \frac{U}{4t} = 1$. The $M = 7L$ operators are grouped with three different methods (meth.) to a linear hardware connectivity with $n = 2L$ qubits, leading to different estimated shot reductions \hat{R} and number N_{circs} of diagonalization circuits. The average and maximum number of CZ-gates in the diagonalization circuits are denoted by $N_{\text{CZ}}^{\text{avg}}$ and $N_{\text{CZ}}^{\text{max}}$, respectively. Similarly, $N_{\text{SWAP}}^{\text{avg}}$ and $N_{\text{SWAP}}^{\text{max}}$ stand for the number of SWAP-gates that are introduced when we transpile the GC circuits to linear connectivity.

L	M	meth.	\hat{R}	N_{circs}	$N_{\text{CZ}}^{\text{avg}}$	$N_{\text{CZ}}^{\text{max}}$	$N_{\text{SWAP}}^{\text{avg}}$	$N_{\text{SWAP}}^{\text{max}}$
3	21	TPB	5.47	5	0	0	0	0
		HT	6.39	4	1.5	4	0	0
		GC	6.25	4	4.75	8	7.5	11
4	28	TPB	7.45	5	0	0	0	0
		HT	8.37	4	1.5	4	0	0
		GC	10.1	3	12.0	24	14.0	32
5	35	TPB	9.49	5	0	0	0	0
		HT	10.54	4	2.0	4	0	0
		GC	10.54	4	10.5	19	26.0	48

TABLE III. Pauli groupings of the momentum-space Hubbard model with L lattice sites. The hardware connectivity (con.) of TPBs may be arbitrary (arb.), but for HT and GC circuits we consider linear (lin.), and cyclic (cyc.) connectivity (see Tab. II for the remaining notation).

L	M	meth.	con.	\hat{R}	N_{circs}	$N_{\text{CZ}}^{\text{avg}}$	$N_{\text{CZ}}^{\text{max}}$	$N_{\text{SWAP}}^{\text{avg}}$	$N_{\text{SWAP}}^{\text{max}}$
3	85	TPB	arb.	3.69	33	0	0	0	0
		HT	lin.	6.58	14	2.64	4	0	0
		HT	cyc.	7.61	11	4.73	6	0	0
		GC	lin.	8.04	10	8	10	15.7	22
		GC	cyc.	8.04	10	8	10	11.8	15
4	166	TPB	arb.	4.45	49	0	0	0	0
		HT	lin.	8.80	21	2.48	6	0	0
		HT	cyc.	8.30	23	3.04	8	0	0
		GC	lin.	13.83	10	24.3	38	45.9	78
		GC	cyc.	13.83	10	24.3	38	35.1	57
5	433	TPB	arb.	3.66	177	0	0	0	0
		HT	lin.	10.55	48	3.81	7	0	0
		HT	cyc.	10.71	47	4.21	9	0	0
		GC	lin.	14.39	29	27.38	48	75.79	115
		GC	cyc.	14.39	29	27.38	48	57.21	108

approximately optimizes \hat{R} .

For the GC groupings, we compute diagonalization circuits using a readily available algorithm [6] in combination with the subroutine to complete a stabilizer group, which we introduce in Sec. I. Since the GC approach is very generic, it is unsurprising that the number N_{CZ} of two-qubit gates is significantly larger for GC than for HT. Note that other methods for constructing GC circuits also exist [9, 55]. We transpile the obtained GC circuits to a linear hardware connectivity using a feature of Qiskit [36], which introduces a (not necessarily minimal) number N_{SWAP} of SWAP-gates. In Tab. II, we can see that for GC circuits, the ratio $N_{\text{SWAP}}^{\text{avg}}/N_{\text{CZ}}^{\text{avg}}$ takes values between 1.1 and 2.5, i.e., noisy SWAP-gates could sig-

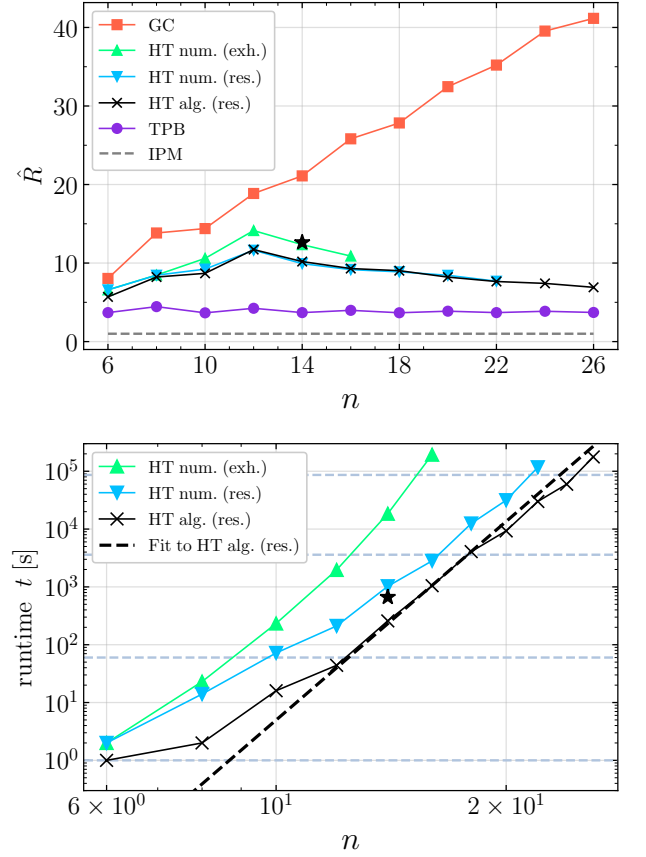


FIG. 10. Estimated shot savings \hat{R} as in Eq. (67) (top) and classical pre-processing time t (bottom) as a function of the number n of qubits for different Pauli groupings of the one-dimensional, periodic Hubbard model in momentum-space representation using block-spin Jordan-Wigner encoding. For the hardware-tailored (HT) Pauli groupings, the single-qubit Clifford gates were constructed by solving the corresponding system of algebraic equations either based on Gaussian elimination (HT alg.) or through numerical optimization (HT num.). For the latter, we carried out both an exhaustive (exh.) search over all 2^{n-1} subgraphs of the n -vertex path graph as well as a restricted (res.) search over $\min\{\frac{3}{2}n^2 - \frac{n}{2}, 2^{n-1}\}$ randomly selected subgraphs. For HT alg. (res.), we only consider $\min\{n^2, 2^{n-1}\}$ random subgraphs and additionally restrict the search space with a cut-off of $\lfloor \log_2(n) \rfloor$ as in Sec. II C. For the data point with the symbol \star at $n = 14$ (also HT alg.), the number of random subgraphs are increased to 1000. All computations were carried out on an 18 core Intel Xeon CPU E5-2697 v4 @2.30GHz device. In the upper panel, we also show the results of SI (\hat{R}_{GC}), SI-QWC (\hat{R}_{TPB}), and $\hat{R}_{\text{IPM}} \equiv 1$ for individual Pauli measurements.

nificantly deteriorate experimental results. For HT and TPB circuits, on the other hand, we have $N_{\text{SWAP}} = 0$ by design. For measuring the real-space Hubbard Hamiltonian, it might be more convenient to simply use the analytical Pauli grouping into $N_{\text{circ}} = 5$ TPBs because $N_{\text{CZ}, \text{TPB}} = 0$ and the estimated shot-reduction ratio $\hat{R}_{\text{HT}}/\hat{R}_{\text{TPB}}$ is only marginally larger than one. This is

not a failure of our approach but due to the simplicity of the problem as evidenced by $\hat{R}_{\text{TPB}} \approx \hat{R}_{\text{HT}} \approx \hat{R}_{\text{GC}}$.

In contrast to real-space Hubbard Hamiltonians, Pauli groupings of their momentum-space analogues clearly exhibit the expected relationship $\hat{R}_{\text{TPB}} < \hat{R}_{\text{HT}} < \hat{R}_{\text{GC}}$ (see Tab. III and Fig. 10). Again, we take the “sorted” list of Pauli operators together with their coefficients from Qiskit nature and use SI to construct GC Pauli groupings. This time, it would be substantially more involved to construct TPBs analytically, so we use SI-QWC instead. For Tab. III, we construct two HT Pauli groupings for each $L \in \{3, 4, 5\}$ by applying our algorithm (no cutoff, all subgraphs) to both linear and cyclic hardware connectivity. When compared to linear connectivity, the availability of an additional two-qubit gate for cyclic connectivity can lead to a better value of \hat{R}_{HT} ($L \in \{3, 5\}$). However, a decrease in \hat{R}_{HT} is also possible ($L = 4$) as our algorithm avoids the problem of maximizing \hat{R} , which is NP-hard in general [9]. For TPBs, hardware connectivity is irrelevant as their readout circuits do not make use of two-qubit gates. For GC Pauli groupings, which are constructed without imposing connectivity constraints, \hat{R} , N_{circs} , and N_{CZ} are independent of the connectivity, whereas N_{SWAP} is smaller for cyclic connectivity because a few SWAP-gates can be saved. For all three methods (TPB, HT, GC), the observations about N_{CZ} and N_{SWAP} from Tab. II are also valid for Tab. III. Furthermore, we see that for a fixed number of qubits \hat{R} and N_{circs} are anti-correlated (see Sec. VIA for a similar observation in the case of random Hamiltonians). It is also worth noting that our algorithm reveals that many subgraphs can be used multiple times (with a varying single-qubit-gate layer). The most striking example is at $L = 3$ and cyclic connectivity, where the Pauli grouping with $N_{\text{circ}} = 11$ readout circuits only makes use of three different readout circuit templates: one TPB ($Z^{\otimes 6}$), four circuits based on the subgraph ①–②–③ ④–⑤–⑥, and six circuits based on the full cyclic connectivity graph. The complete list of ratios $N_{\text{templates}}/N_{\text{circs}}$ is given by 4/14, 10/21, 29/48 for linear and 3/11, 17/23, 32/47 for cyclic connectivity, respectively. This implies that those circuit templates, which are particularly suited for HT readout, are not randomly distributed among the list of 2^e subgraphs of the connectivity graph, where $e_{\text{lin}} = 2L - 1$, $e_{\text{cyc}} = 2L$ is its number of edges. Identifying unsuitable subgraphs beforehand and removing them from the list of considered subgraphs could speed up our algorithm significantly; we leave exploring this idea for future research.

In the upper panel of Fig. 10, we plot the estimated shot reduction \hat{R} for various Pauli groupings of the momentum-space Hubbard Hamiltonian as a function of the number $n = 2L$ of qubits. Hereby, we observe a clear upward trend of \hat{R}_{GC} (red squares) that is roughly linear in n with a slope of 1.6. Whereas earlier in Fig. 8 we noticed a decrease of \hat{R}_{GC} with n , an increase is possible in the present case because the number $M \approx 0.3 \times n^{3.14}$ of Pauli operators is not constant, e.g., $M = 8305$ for $n = 26$. In Fig. 10, we also see that for $n \leq 26$, all values

of \hat{R}_{TPB} (purple circles) lie in the interval [3.6, 4.5]. Thus, the potential gain of GC readout circuits over TPBs is growing with the size of the problem. Unfortunately, the same cannot be said about HT readout circuits if they are tailored to a **linear** hardware connectivity: initially, \hat{R}_{HT} also grows, reaching its maximum at $n = 12$, followed by a modest but steady decline.

We show three different curves for \hat{R}_{HT} because we want to explore the variability of the algorithm introduced in Sec. V. Irrespective of the variant, we again observe the typical relation $\hat{R}_{\text{TPB}} < \hat{R}_{\text{HT}} < \hat{R}_{\text{GC}}$. First, we apply the numerical solver from Sec. IID to an exhaustive list of all 2^{n-1} subgraphs, yielding $\hat{R}_{\text{HT}}^{\text{num-exh}}$ (green upward triangles). Since this approach is computationally feasible only for $n \leq 16$, we also plot $\hat{R}_{\text{HT}}^{\text{num-res}}$ (blue downward triangles) for which the considered readout circuit templates are restricted to $\frac{3}{2}n^2 - \frac{n}{2}$ (if available) randomly selected subgraphs, which is feasible for $n \leq 22$. By further decreasing the number of random subgraphs to n^2 (if available) and switching from the numerical to the algebraic solver from Sec. IIB with a logarithmic cutoff, we get $\hat{R}_{\text{HT}}^{\text{alg-res}}$ (black crosses) for all $n \leq 26$. Based on our findings in Sec. VIA, we are confident that $\hat{R}_{\text{HT}}^{\text{num-exh}}$ almost maximizes \hat{R} under the constraint of a linear hardware connectivity. This comes at the expense of a long time $t_{\text{HT}}^{\text{num-exh}}$ that is needed to compute the Pauli grouping (see lower panel of Fig. 10). By restricting the search space to a polynomial number of subgraphs, the process is sped up, and the additional logarithmic cutoff causes $t_{\text{HT}}^{\text{alg-res}}$ to scale polynomially by design. This scaling manifests itself in a fit through $n \in \{10, 12, 14, 16, 18\}$ where a power-law of $t_{\text{fit}} \approx 10^{-11} n^{11.4}$ s is obtained (black dashed line). Note that we obtain almost coinciding results $\hat{R}_{\text{HT}}^{\text{alg-res}} \approx \hat{R}_{\text{HT}}^{\text{num-res}}$, even though $t_{\text{HT}}^{\text{alg-res}}$ is between two and five times smaller than $t_{\text{HT}}^{\text{num-res}}$. Strikingly, at $n = 14$ (black star) we are able to increase $\hat{R}_{\text{HT}}^{\text{alg-res}}$ from 10.2 to 12.6 (even larger than $\hat{R}_{\text{HT}}^{\text{num-exh}} \approx 12.3$) by raising the number of considered random subgraphs from 196 to 1000. Meanwhile, the runtime $t_{\text{HT}}^{\text{alg-res}}$ increases from four to eleven minutes, which is faster than $t_{\text{HT}}^{\text{num-res}} \approx 17$ min and much faster than $t_{\text{HT}}^{\text{num-exh}} = 5$ h. We are confident that similar trade-offs are achievable in general.

In order to measure the momentum-space Hubbard Hamiltonian \hat{H} in a quantum simulation using $n \leq 26$ linearly connected qubits, we recommend exploiting HT readout circuits because $\hat{R}_{\text{HT}}/\hat{R}_{\text{TPB}}$ lies between 1.8 ($n \in \{6, 26\}$) and 3.3 ($n \in \{12, 14\}$). In other words, one can expect a significant reduction in the number of shots required to estimate $\langle \hat{H} \rangle$ to a target precision by measuring HT Pauli groupings instead of TPBs. Although $\hat{R}_{\text{GC}}/\hat{R}_{\text{TPB}}$ keeps growing, it would be impractical to execute GC circuits on a quantum computer with a restricted hardware connectivity (see Tab. III). It would be highly interesting to explore whether a two-dimensional hardware connectivity is sufficient for a continuous growth of $\hat{R}_{\text{HT}}/\hat{R}_{\text{TPB}}$. Since the number of available readout circuit templates scales exponentially in the

number of edges of the connectivity graph, we leave this question for future work.

Finally, let us mention a related problem for which we expect that the measurement process would greatly benefit from our HT readout circuits. It was recently recognized that a transcorrelated formulation of the Hubbard model can enable more accurate quantum simulations than a naive approach [56–58]. Since effective 3-body interactions occur in the transcorrelated Hamiltonians, the number M of Pauli operators is much larger than for the here-discussed non-transcorrelated Hamiltonians. It is worth exploring whether this increase in M leads to a better value of $\hat{R}_{\text{HT}}/\hat{R}_{\text{TPB}}$, as it does, e.g., for random Hamiltonians (recall Fig. 2).

C. Selected Molecules

In this section, we showcase the applicability of our techniques to the solution of electronic structure problems. Moreover, we explore how the choice of its hyperparameters influences the performance of Algorithm 1 from Sec. V. To this end, we consider the following selection of molecules:

- LiH with an interatomic distance of 1.545 Å.
- H₄ on a 1.7380 Å × 1.5148 Å rectangular geometry.
- N₂ with an interatomic distance of 1.25 Å.
- H₂O with oxygen at the origin and the two hydrogen nuclei on the $z = 0$ plane with coordinates $x_1 = 0$, $y_1 = 0.591$ Å and $x_2 = 0.572144$ Å, $y_2 = -0.148094$ Å.
- HCN on a linear arrangement along the x -axis with $x_{\text{H}} = -1.10$ Å, $x_{\text{C}} = 0$, and $x_{\text{N}} = 1.15$ Å.

For LiH, we can take the Pauli decomposition of the second-quantized molecular Hamiltonian

$$\hat{H} = \sum_{p,q} h_{p,q} \hat{a}_p^\dagger \hat{a}_q + \frac{1}{2} \sum_{p,q,r,s} h_{p,q,r,s} \hat{a}_p^\dagger \hat{a}_q^\dagger \hat{a}_r \hat{a}_s, \quad (86)$$

directly from Table S2 of Ref. [4]. Note that both sums in Eq. (86) run over all combinations of considered molecular orbitals ϕ_p with creation operator \hat{a}_p^\dagger [3]. For the other molecules, we perform restricted Hartree-Fock calculations using PySCF [59], which yields the one-body integrals

$$h_{p,q} = \int d\mathbf{x} \phi_p^*(\mathbf{x}) \left(-\frac{\nabla^2}{2} - \sum_I \frac{Z_I}{|\mathbf{r} - \mathbf{R}_I|} \right) \phi_q(\mathbf{x}), \quad (87)$$

(where $\mathbf{x} = (\mathbf{r}, \sigma)$ denotes position \mathbf{r} and spin σ of an electron, and Z_I and \mathbf{R}_I are atomic number and position of the I -th nucleus), as well as the two-body integrals

$$h_{p,q,r,s} = \int d\mathbf{x}_1 d\mathbf{x}_2 \frac{\phi_p^*(\mathbf{x}_1) \phi_q^*(\mathbf{x}_2) \phi_r(\mathbf{x}_2) \phi_s(\mathbf{x}_1)}{|\mathbf{r}_1 - \mathbf{r}_2|}. \quad (88)$$

TABLE IV. Estimated shot reduction \hat{R} for different Pauli groupings of molecular Hamiltonians with n qubits and M Pauli operators. TPB and GC groupings are obtained with the SI-QWC and SI algorithm, respectively [9]. For HT groupings, diagonalization circuits are tailored to the hardware connectivity^a of *ibmq-guadalupe* using two variants of our algorithm, which differ by the objective function: *size only* as in Eq. (65) and *with coefficients* as in Eq. (66). Here, we use the algebraic solver from Sec. IIB in combination with an exhaustive search over all subgraphs. For N₂ and HCN, we speed up computations by exploiting cutoffs $c_{\text{N}_2} = 5$ and $c_{\text{HCN}} = 3$ as in Sec. IIC. All computations were carried out on an 18 core Intel Xeon CPU E5-2697 v4 @2.30GHz device.

name	n	M	\hat{R}_{TPB}	$\hat{R}_{\text{HT}}^{(65)}$	$\hat{R}_{\text{HT}}^{(66)}$	\hat{R}_{GC}
LiH	4	99	6.57	7.78	8.86	8.75
H ₄	5	120	6.76	10.69	10.39	14.65
H ₂ O	9	753	12.20	18.60	19.87	25.15
N ₂	12	1210	18.85	29.48	31.35	60.64
HCN	15	3771	16.91	24.41	25.44	67.89

^a Digital feature: Clicking on the name of any molecule redirects to a web-page showing the assumed connectivity graph [64].

For simplicity, we consider the STO-3G minimal basis set $\{\phi_p\}$. The fermionic operators are mapped to Pauli operators using the parity encoding [60], where we make use of precision-preserving qubit-reduction methods as proposed in Refs. [61–63] and implemented in Qiskit [36]. This leads to Hamiltonians whose numbers n and M of qubits and Pauli operators, respectively, are provided in Tab. IV. We then apply SI, SI-QWC, as well as our own algorithm to obtain GC, TPB, and HT Pauli groupings of these Hamiltonians. As we show in Tab. IV, this yields the expected relationship $\hat{R}_{\text{TPB}} < \hat{R}_{\text{HT}} < \hat{R}_{\text{GC}}$, which demonstrates the applicability of our method to the electronic structure problem.

Recall that, in every step of our algorithm, we construct one collection $\{P_{i_1}, \dots, P_{i_m}\}$ for every subgraph under consideration. Then, we select the “best” collection and assign its Pauli operators to the corresponding diagonalization circuit. In Sec. V, we propose two different objective functions for quantifying the value of a collection: (65) *the number of elements it contains*, and (66) *a function that also takes coefficients into account*. A priori, it is unclear which objective function will lead to a better result. In Tab. IV, we see $\hat{R}_{\text{HT}}^{(65)} < \hat{R}_{\text{HT}}^{(66)}$ for all examples except for H₄, where $\hat{R}_{\text{HT}}^{(65)} \gtrsim \hat{R}_{\text{HT}}^{(66)}$ holds. Because of this, we find it more promising to use the value function defined in Eq. (66). Thus, this option is used throughout this paper as a default.

In addition to Tab. IV, where the algebraic solver with a cutoff is used, we apply the numerical solver from Sec. IID in order to construct near-optimal HT Pauli groupings for the two largest molecules under consideration. While the search requires about four hours to find $\hat{R}_{\text{HT,N}_2}^{\text{num}} \approx 35.33$, it takes an entire week to obtain $\hat{R}_{\text{HT,HCN}}^{\text{num}} \approx 32.50$. In comparison, finding the subopti-

TABLE V. Balancing the hyperparameters of our algorithm at the example of a molecular Hamiltonian for HCN with $n = 15$ qubits. The choice of the cutoff from Sec. IIC and the considered number of randomly selected subgraphs influences the obtained grouping of the $M = 3,771$ Pauli operators into N_{HT} jointly-measurable collections, the estimated shot reduction \hat{R}_{HT} , and the pre-processing time t . We tailor the diagonalization circuits to the hardware connectivity of *ibmq-guadalupe* for which $2^{15} = 32,768$ subgraphs exist. All computations were carried out on an 18 core Intel Xeon CPU E5-2697 v4 @2.30GHz device.

cutoff	subgraphs	N_{HT}	\hat{R}_{HT}	$\frac{\hat{R}_{\text{HT}}}{\hat{R}_{\text{TPB}}}$	t [h]
0	1,000	701	20.15	1.19	0.9
	5,000	637	22.25	1.32	2.0
	all	615	23.26	1.38	22
2	1,000	648	21.44	1.27	1.0
	10,000	584	24.05	1.42	4.9
3	1,000	607	22.91	1.35	1.3
	5,000	560	24.23	1.43	3.6
	all	532	25.44	1.50	30
5	1,000	534	24.52	1.45	5.1
	5,000	486	26.50	1.57	14
7	100	600	21.89	1.29	43

mal grouping with $\hat{R}_{\text{HT,HCN}}^{(66)} \approx 25.44$ from Tab. IV requires thirty hours. By modifying both the cutoff and the number of considered subgraphs, it is possible to balance \hat{R}_{HT} and the pre-processing time t (see Tab. V). With cutoff = 5 and a subset of 5,000 randomly selected subgraphs, we can construct a HT Pauli grouping for HCN with $\hat{R}_{\text{HT}} \approx 26.50$ in only fourteen hours. This is faster and better than, e.g., cutoff = 3 and all subgraphs, or cutoff = 7 and only 100 subgraphs. If the number of subgraphs is too small, we are neglecting well-suited read-out circuit templates, which leads to a suboptimal value of \hat{R} . On the other hand, if it is too large, we are redundantly constructing circuits (for multiple subgraph) for Pauli operators for which a good circuit has already been found, which leads to an increase of t without improving \hat{R} . Similarly, if the cutoff is too large, we are redundantly constructing circuits by computing multiple single-qubit Clifford-gate layers (for every single subgraph, where this is possible), which also increases t without improving \hat{R} . Conversely, if the cutoff is too small, we are skipping valuable circuit templates; even if they are included in the list of considered subgraphs. The latter is not as prohibitive as one could believe naively, having the discussion of Fig. 4 in mind: even for cutoff = 0, we obtain HT Pauli groupings that notably outperform $\hat{R}_{\text{TPB}} \approx 16.91$ (see Tab. V). In conclusion, our algorithm can greatly benefit from a suitable choice of its hyperparameters. The study of the optimal strategy for selecting hyperparameters is beyond the scope of this work and requires further investigation.

D. Hydrogen Chains

As its name suggests, a *hydrogen chain* of length L is a molecule consisting of L hydrogen atoms arranged on a line. For simplicity, we assume that the interatomic distance Δ between two adjacent hydrogen nuclei is constant throughout the chain. In contrast to the Hubbard Hamiltonian, the molecular Hamiltonian [see Eq. (86)] of a hydrogen chain includes long-range Coulomb interactions as well as the possibility to occupy a given “lattice site” with more than two electrons. While these features enable new (for 1D systems) effects, e.g., antiferromagnetic correlations and dimerization for large Δ as well as an insulator-to-metal transition at $\Delta \approx 0.9 \text{ \AA}$ [65], it is practically impossible to analytically solve the Schrödinger equation for these systems. However, sophisticated numerical studies for computing the energy [66] and other physical properties [65] of its ground state have been carried out.

For the purpose of benchmarking quantum simulations, hydrogen chains and the Hubbard model share the similarities of a variability of the problem size, the possibility of comparing results to a classical solution, and the prospect for an eventual generalization to the two- and three-dimensional cases, which are classically intractable. The absence of an analytical solution for hydrogen chains, however, makes them more interesting for near-term quantum experiments than the Hubbard model. This is the reason why we choose to experimentally demonstrate the practicality of our HT Pauli groupings with an example of a hydrogen chain (see Sec. X).

In this section, we apply Pauli grouping algorithms to hydrogen chains with $L \in \{4, 6, 8, 10, 12, 14\}$ atoms and an interatomic spacing of $\Delta = 1.0 \text{ \AA}$. Similarly to Sec. VIC, we generate the Hamiltonians using Qiskit nature [36] in combination with pyquante [67]. Again, we make use of the STO-3G minimal basis set and the parity encoding to obtain a Hamiltonian in the form of Eq. (1) with $n = 2L - 2$ qubits and $M \approx 0.17 \times n^{3.68}$ Pauli operators, e.g., $M = 27734$ for $n = 26$. First, we group the Pauli operators into general commuting (GC) sets using the SI algorithm of Ref. [9] and obtain an estimated shot reduction of $\hat{R}_{\text{GC}} \approx 4n$. Likewise, we find $\hat{R}_{\text{TPB}} \in [12.3, 14.6]$ by grouping the Pauli operators into tensor product bases (TPBs) using SI-QWC. Next, we apply our HT Pauli grouping algorithm from Sec. V assuming a linear hardware connectivity. In the upper panel of Fig. 11, we show the ratio $\hat{R}_{\text{HT}}/\hat{R}_{\text{TPB}}$ as this quantifies the estimated shot savings of our method compared to the best previously available approach of practical interest. For $n \in \{6, 10, 14\}$, we can afford to carry out an exhaustive search over all 2^{n-1} read-out circuit templates using the numerical solver from Sec. IID (red stars). To obtain HT Pauli groupings for even larger Hamiltonians, we apply the algebraic solver from Sec. IIC for two choices of constant hyperparameters: cutoff=5 and 2000 subgraphs (blue squares), and cutoff=3 and 1000 subgraphs (black circles). Note that

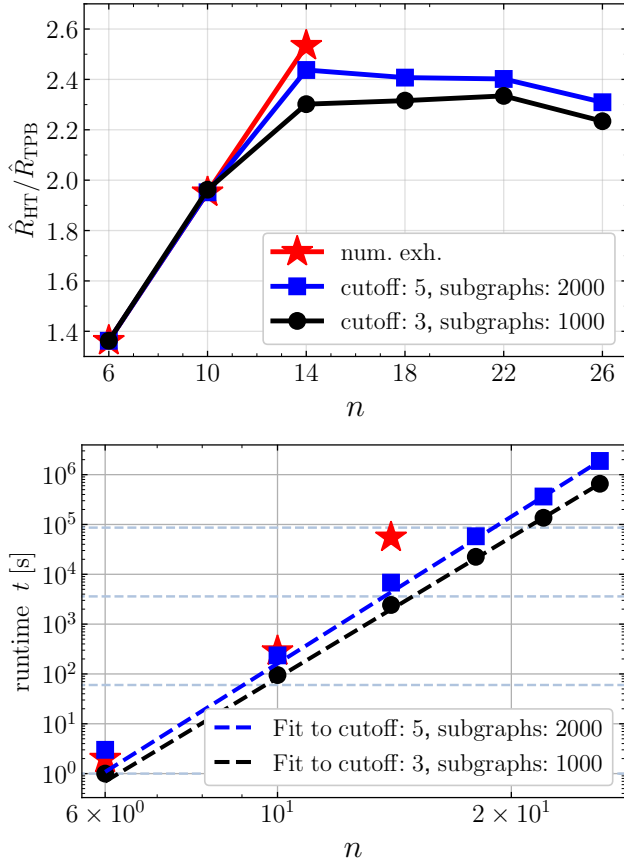


FIG. 11. Ratio $\hat{R}_{\text{HT}}/\hat{R}_{\text{TPB}}$ of estimated shot savings (top) and classical pre-processing time t (bottom) as a function of the number n of parity-encoded qubits for different Pauli groupings of hydrogen chains with $L = \frac{n}{2} + 1$ nuclei and an interatomic spacing of $\Delta = 1 \text{ \AA}$. For the hardware-tailored (HT) Pauli groupings, we either use an exhaustive numerical search (num. exh.) or the restricted algebraic approach from Sec. II C with cutoff and number of subgraphs as indicated in the legend. Throughout, we assume a linear hardware connectivity. All computations were carried out on an 18 core Intel Xeon CPU E5-2697 v4 @2.30GHz device.

the subgraph restriction is only applicable for $n \geq 14$ because the number of subgraphs does not exceed these limits for $n = 6$ and $n = 10$. In the latter case, the results of all three methods nearly coincide, which is interesting because one could expect that introducing a cutoff for the algebraic solver would lead to worse results than in the exhaustive, numerical one. For all cases considered in Fig. 11, we clearly observe $\hat{R}_{\text{HT}}/\hat{R}_{\text{TPB}} > 1$, i.e., our HT approach consistently outperforms TPBs. Initially, this advantage becomes more pronounced with increasing n . But starting from $n = 18$ qubits, we observe a saturation of $\hat{R}_{\text{HT}}/\hat{R}_{\text{TPB}}$. We attribute this behavior to the limited (one-dimensional) hardware connectivity under consideration since the ratio $\hat{R}_{\text{GC}}/\hat{R}_{\text{TPB}}$ continues its growth (not shown). In the lower panel of Fig. 11, we depict the time t that is needed to construct the above HT Pauli groupings. By design of our algorithm, t scales

TABLE VI. Influence of frequent renewal of the random selection of subgraphs on $\hat{R}_{\text{HT}}/\hat{R}_{\text{TPB}}$ for the example of two hydrogen chains with eight ($n = 14$ qubits) and ten ($n = 18$) sites at an interatomic distance of $\Delta = 1 \text{ \AA}$. Assuming linearly-connected qubits, we construct hardware-tailored (HT) Pauli groupings in two different ways. **(normal)** original form of Algorithm 1. **(modified)** after a collection of jointly-HT-diagonalizable Pauli operators is assigned (line 21 in Alg. 1), we replace **subgraphs** with a newly-sampled random list.

n	cutoff	subgraphs	$\hat{R}_{\text{HT}}^{\text{normal}}/\hat{R}_{\text{TPB}}$	$\hat{R}_{\text{HT}}^{\text{modified}}/\hat{R}_{\text{TPB}}$
14	3	300	2.15	2.06
	3	500	2.21	2.12
	3	1,000	2.30	2.20
	3	2,000	2.35	2.34
	5	300	2.15	2.32
	5	2,000	2.44	2.34
18	3	500	2.24	2.30
	5	300	2.23	2.26
	5	2,000	2.41	2.20

polynomially in n when we restrict to constant hyperparameters. This is testified by two power-law fits (dashed lines) $t_{\text{fit,blue}} \approx 10^{-8} \times n^{9.8} \text{ s}$ and $t_{\text{fit,black}} \approx 10^{-8} \times n^{9.4} \text{ s}$. The second method is faster because its hyperparameters are smaller, which leads to a more restricted search space. All these observations are very similar to the momentum-space Hubbard model, which is discussed in Sec. VI B. These similarities strongly indicate that, across different problem classes, our approach performs qualitatively the same.

Finally, we test a possible modification of Algorithm 1 based on the possibility of resampling the set of random subgraphs every time a set of jointly-HT-diagonalizable Pauli operators is assigned. Although in this way the diversity of circuit templates is increased, we do not observe clear benefits compared to the original method (see Tab. VI). Only if the number of subgraphs is very small, we sometimes obtain a small advantage of the modified redrawing method. In practice, however, it is impractical to restrict to a very small number of subgraphs as this can easily lead to suboptimal HT Pauli groupings (also see Tab. V). Further investigation is needed to better understand why changing the selection of subgraphs during the computation often leads to slightly worse Pauli groupings in Tab. VI.

VII. REUSABILITY OF PAULI GROUPINGS

Our theoretical framework enables the construction of hardware-tailored (HT) readout circuits. A direct application of the HT Pauli grouping algorithm introduced in Sec. V is feasible as long as the number e of edges in the connectivity graph, to which the HT circuits are tailored, stays below $e_{\text{max}} \approx 15$ (see Sec. VI). For larger problem sizes, we can adjust the hyperparameters (cutoff, number of subgraphs) of our algorithm to keep the runtime

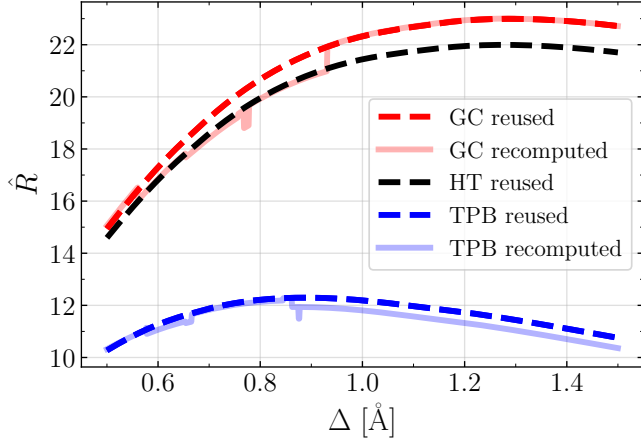


FIG. 12. Estimated shot reduction \hat{R} of Pauli groupings of a molecular Hamiltonian into general commuting (GC) sets, jointly-HT-measurable sets, and tensor product bases (TPB). The considered molecule, for which we compute the relevant integrals in the STO-3G basis using Qiskit nature [36] in combination with pyquante [67], is a four-atomic hydrogen chain with an interatomic distance of Δ . Using the Bravyi-Kitaev encoding, the Hamiltonian is mapped to $n = 8$ qubits. For the HT readout circuits, we assume a linear hardware connectivity.

practical while still achieving $\hat{R}_{\text{HT}} > \hat{R}_{\text{TPB}}$. For example we are able to reduce the preprocessing time for grouping the Pauli operators of an exemplary Hubbard Hamiltonian (\star , $n = 14$) from 5 hours to 11 minutes, without any sacrifice in \hat{R} (see Fig. 10 in Sec. VIB). Carefully balancing the hyperparameters of our algorithm can be tedious. Thus, it is important to know under which circumstances an existing HT Pauli grouping can be reused in a different context.

Consider two observables O and O' with the same Pauli operators P_1, \dots, P_M , in Eq. (1), but different coefficients $(c_1, \dots, c_M) \neq (c'_1, \dots, c'_M)$. When a HT Pauli grouping of O with a satisfactory large value of \hat{R}_{HT} has been constructed, it can be reused for O' as well. Note that \hat{R}'_{HT} for O' will have a similarly large value to \hat{R}_{HT} if, for example, both O and O' are molecular Hamiltonians of the same molecule at slightly different nuclear configurations. The reason for this is that the molecular integrals $h_{p,q}$ and $h_{p,q,r,s}$ in Eqs. (87)–(88) continuously depend on the coordinates of the nuclei. Indeed, after mapping the fermionic operators to a linear combination of Pauli operators, e.g., with Jordan-Wigner or Bravyi-Kitaev encoding, the coefficients c_i in Eq. (1) arise as linear, and thus continuous functions of the molecular integrals [3]. Finally, recall from Eq. (67) that \hat{R} continuously depends on the coefficients c_i . This establishes our claim that, *for a given HT Pauli grouping of a molecular Hamiltonian, \hat{R}_{HT} continuously depends on the nuclear coordinates*. In Fig. 12, we visualize this result at the example of a hydrogen chain. For this, we compute one GC, HT, and

TPB Pauli grouping for the molecular Hamiltonian with interatomic distances of $\Delta_{\text{GC}} = 1.5 \text{ \AA}$, $\Delta_{\text{HT}} = 1.0 \text{ \AA}$, and $\Delta_{\text{TPB}} = 0.85 \text{ \AA}$, respectively. Then, we reuse each of these Pauli groupings to compute \hat{R} for every value of $\Delta \in [0.5 \text{ \AA}, 1.5 \text{ \AA}]$ and in steps of 1 m\AA . Needless to say, the resulting (dashed) curves are continuous in Δ . In addition to this, we recompute the GC and TPB Pauli grouping for every value of Δ , which results in piecewise-continuous (bright, solid) curves. Note that the branch jumps of these curves occur at values of Δ at which the Pauli groupings produced by SI and SI-QWC [9], respectively, undergo a modification. It is worth noting that \hat{R}_{HT} (black) is not much smaller than \hat{R}_{GC} (red), i.e., here it is not a severe restriction to only allow readout circuits that match the assumed linear hardware connectivity. Furthermore, the gap between \hat{R}_{HT} and \hat{R}_{TPB} (blue) remains clearly open across the entire plotted range of Δ . Therefore, the advantage of our HT readout circuits over TPBs is compatible with reusing a given HT Pauli grouping, as desired.

So far, we have based reusability on the assumption that both observables O and O' contain the same Pauli operators in their respective decompositions. For particularly symmetric configurations of the nuclei, however, it can happen that some of the molecular integrals in Eqs. (87) and (88) vanish. If such a symmetry is present during the construction of a HT Pauli grouping, a new HT Pauli grouping has to be constructed for Hamiltonians which break the symmetry. Also here one can reuse the original HT Pauli grouping because only the new Pauli operators require the construction of additional HT readout circuits.

Let us conclude by pointing out a research direction of high practical interest. Our framework provides a suitable toolkit for tackling the problem of constructing HT Pauli groupings of a *general* molecular Hamiltonian for which all of the terms in Eq. (86) are non-zero. The resulting set of Pauli operators in Eq. (1) only depends on the fermion-to-qubit mapper. Therefore, our techniques could find widespread use in the field of quantum simulation after setting up a digital library of readily available HT Pauli groupings with the following keywords:

- Number of molecular orbitals
- Fermion-to-qubit mapper
- Hardware connectivity

For an account of important fermion-to-qubit mappers, see Ref. [68] and references therein. Important hardware connectivities include linear, square-lattice, and heavy-hexagonal connectivity [26]. Obtaining such HT Pauli groupings for problem sizes that exceed the capabilities of classical simulations will require further research. For a first step in this direction see Sec. VIII.

VIII. PRE-PROCESSING TIME VS. RUNTIME SAVINGS FOR A 52-QUBIT EXAMPLE

In this section, we demonstrate the possibility to scale up the construction of hardware-tailored (HT) readout circuits to problem sizes that are beyond the border of classical simulatability. Furthermore, we argue that the costs for classically pre-computing these circuits can be small compared to the enabled quantum runtime savings. We consider a linear chain with $L = 26$ hydrogen atoms at an interatomic distance of $\Delta = 1.0 \text{ \AA}$ as in Sec. VID. Here, we express this molecule in the STO-3G basis set and use the Bravyi-Kitaev (BK) mapping to obtain a Hamiltonian $O = \sum_{i=1}^M c_i P_i$ with $M = 443,715$ Pauli operators on $n = 52$ qubits. First, we apply SI-QWC to group P_1, \dots, P_M into $N_{\text{TPB}} = 136,325$ tensor product bases (TPBs) as this represents the prior state of the art upon which we will improve. While the average number of $M/N_{\text{TPB}} \approx 3.25$ Pauli operators per TPB is consistent with previous observations [5], we stress that the operators are far from being evenly distributed among the TPBs. In Fig. 13, we show that the number of TPBs containing a given number m_i of Pauli operators follows a distribution (green dots) which is well-approximated by a power-law decay of $10^5 \times m_i^{-2}$ (gray line). Importantly, there are 70,579 Pauli operators with $m_i = 1$, which are mutually non-QWC. Hence, each of them requires its own TPB, i.e., if we want to group these “ungrouped” operators into jointly-measurable sets, we need to permit two-qubit gates in the readout circuits. Note that for BK Hamiltonians the weight (size of the support) of the involved Pauli operators P_i only grows logarithmically in n [60]. We exploit this fact in Algorithm 2.

The underlying principle of Algorithm 2 is the same as that of Algorithm 1 from Sec. V: in every iteration of the outer loop (lines 3-26), we construct a HT readout circuit for P_{main} , which is leading the list \mathcal{P}_{rem} of remaining Pauli operators. This time, we remove all operators from \mathcal{P}_{rem} that do not commute with P_{main} because none of them is jointly-HT-measurable with P_{main} ; the resulting selection is denoted by $\mathcal{P}_{\text{sel}} = f_1(\mathcal{P}_{\text{rem}}, P_{\text{main}})$ (line 5). Our new idea is to restrict to subgraphs of $\Gamma|_{\text{supp}(P_{\text{main}})}$, i.e., only two-qubit gates within the support of P_{main} are allowed. In this way, the efficiency of Algorithm 2 is ensured because of $|\text{supp}(P_i)| = \mathcal{O}(\log(n))$ for all $i \in \{1, \dots, M\}$. Naively, one might try to proceed by only taking the operators $P_i \in \mathcal{P}_{\text{sel}}$ with $\text{supp}(P_i) \subset \text{supp}(P_{\text{main}})$ into account as this would render the measurements outside of the support of P_{main} irrelevant and consequently speed up the construction of readout circuits; however, such operators are prohibitively rare. As a more sophisticated approach, we instead guess a suitable single-qubit measurement basis for every qubit $j \in \{1, \dots, n\} \setminus \text{supp}(P_{\text{main}})$. Our guess is the single-qubit Pauli operator $P_{\text{mf}}^{(j)} \in \{X, Y, Z\}$ that occurs *most frequently* among the n -qubit Pauli operators $P = P^{(1)} \otimes \dots \otimes P^{(n)} \in \mathcal{P}_{\text{sel}}$ on qubit j , i.e.,

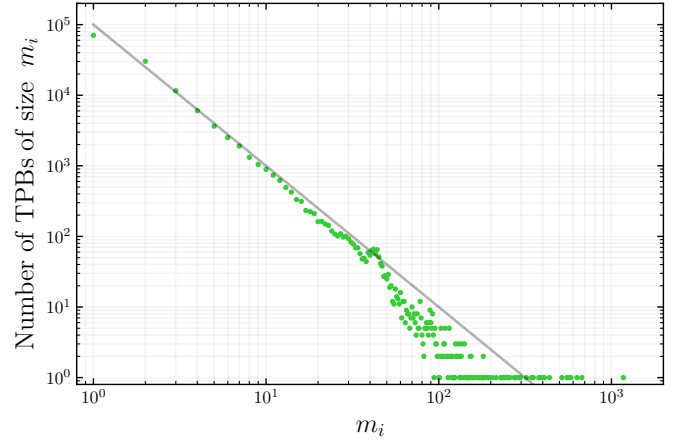


FIG. 13. Size distribution of the $N_{\text{TPB}} = 136,325$ tensor product bases (TPBs) into which the $M = 443,715$ Pauli operators of a Bravyi-Kitaev Hamiltonian with $n = 52$ qubits can be grouped. The Hamiltonian describes a linear hydrogen chain with $L = 26$ sites. Whereas there exists only one TPB that contains as many as $m_i = 1172$ operators, most TPBs (70,579 in total) only contain a single Pauli operator.

Algorithm 2

Modification of Algorithm 1 from Sec. V. This variant is efficient if the support of the operators in `paulis` only grows logarithmically in the number n of qubits, e.g., for Bravyi-Kitaev Hamiltonians.

```

1: out  $\leftarrow \emptyset$ ;
2: remaining_paulis  $\leftarrow$  paulis;
3: while remaining_paulis  $\neq \emptyset$  do
4:   main_pauli  $\leftarrow$  remaining_paulis[0];
5:   selection  $\leftarrow$  f1(remaining_paulis, main_pauli);
6:   main_support  $\leftarrow$  support(main_pauli);
7:   selection  $\leftarrow$  f2(selection, main_support);
8:   subgraphs  $\leftarrow$  select_subgraphs(main_support);
9:   s  $\leftarrow$  length(subgraphs);
10:  temp_collections  $\leftarrow [\emptyset, \dots, \emptyset]$ ;  $\triangleright$  list of length s
11:  for i in [0, ..., s-1] do  $\triangleright$  parallel loop
12:     $\Gamma \leftarrow$  subgraphs[i];
13:    if ht_measurable([main_pauli],  $\Gamma$ ) then
14:      col  $\leftarrow$  [main_pauli];
15:      for pauli in selection do
16:        if ht_measurable(col  $\cup$  [pauli],  $\Gamma$ ) then
17:          col  $\leftarrow$  col  $\cup$  [pauli];
18:        end if
19:      end for
20:      temp_collections[i]  $\leftarrow$  col;
21:    end if
22:  end for
23:  best_collection  $\leftarrow$  best(temp_collections);
24:  remaining_paulis.remove(best_collection);
25:  out.append(best_collection);
26: end while
27: return out;
```

$$P_{\text{mf}}^{(j)} = \arg \max_{p \in \{X, Y, Z\}} \left| \left\{ P \in \mathcal{P}_{\text{sel}} \mid P^{(j)} = p \right\} \right|. \quad (89)$$

Next, we refine our selection \mathcal{P}_{sel} of considered Pauli operators by filtering out all of those that cannot be measured for this guess (line 7), which results in the set

$$f_2(\mathcal{P}_{\text{sel}}, J) = \left\{ P \in \mathcal{P}_{\text{sel}} \mid \forall j \in J^C : P^{(j)} \in \{I, P_{\text{mf}}^{(j)}\} \right\}, \quad (90)$$

where $J^C = \{1, \dots, n\} \setminus J$ denotes the complement of $J = \text{supp}(P_{\text{main}})$. Note that for our purposes $f_2(\mathcal{P}_{\text{sel}}, J)$ is sufficiently large, e.g., in the first iteration of Algorithm 2 applied to the set of $|\mathcal{P}_{\text{rem}}| = 70,579$ operators that remained “ungrouped” after applying SI-QWC to the 52-qubit hydrogen-chain Hamiltonian, we still have $|f_2(\mathcal{P}_{\text{sel}}, J)| = 31$ operators remaining (for $m_1^{\text{HT}} = 5$ of them, Algorithm 2 is able to construct a common HT readout circuit). Then, we proceed by making a selection of subgraphs $\Gamma \subset \Gamma|_{\text{supp}(P_{\text{main}})}$ that will be considered as circuit templates (line 8). Hereby, one can use either all such subgraphs or a random selection of not more than s_{max} (hyperparameter) of them. The remaining steps are the same as for Algorithm 1, with the exception that this time we only attempt to include operators from our filtered selection $f_2(\mathcal{P}_{\text{sel}}, J)$ (line 15).

We apply Algorithm 2 to the aforementioned set of 70,579 “ungrouped” 52-qubit Pauli operators and keep track of its performance over a period of two and a half weeks, see Fig. 14. In total, we group 8231 Pauli operators into 3935 jointly-HT-measurable sets, where a two-dimensional hardware connectivity with up to four nearest neighbors is assumed. For every $N \in \{1, \dots, 3935\}$ when the algorithm identifies the N -th set of jointly-HT-measurable Pauli operators (line 25) we extract: the current average number $\bar{m}_N^{\text{HT}} = (m_1^{\text{HT}} + \dots + m_N^{\text{HT}})/N$ of operators per readout circuit (red squares), the estimated reduction \hat{R}_{HT} in the number of shoots needed to measure the current partial energy $\sum_{i=1}^N \sum_{j=1}^{m_i} c_{i,j} P_{i,j}$ as in Eqs. (67)–(68) from Sec. VI (green triangles), and the current pre-processing speed $(m_1^{\text{HT}} + \dots + m_N^{\text{HT}})/t_N$ at which the Pauli operators are being grouped (blue circles). Then, we plot these three quantities as a function of the time t_N after which the N -th readout circuit has been assigned (line 25). On average, we find $\bar{m}_N^{\text{HT}} \approx 2$ Pauli operators per jointly-HT-measurable collection (min $m_N^{\text{HT}} = 1$, max $m_N^{\text{HT}} = 11$) and an associated shot reduction of $\hat{R}_{\text{HT}} \approx 1.5$. Note that $\hat{R}_{\text{TPB}} = 1$ for the considered problem. The observed average speed of the grouping algorithm is equal to almost one Pauli operator every two minutes; note that we did not parallelize the loop over the subgraphs (lines 11–22) to reduce our implementation efforts for this proof-of-principle demonstration. For practical applications, however, we highly recommend a parallel implementation as this would significantly enhance the pre-processing speed. Our most

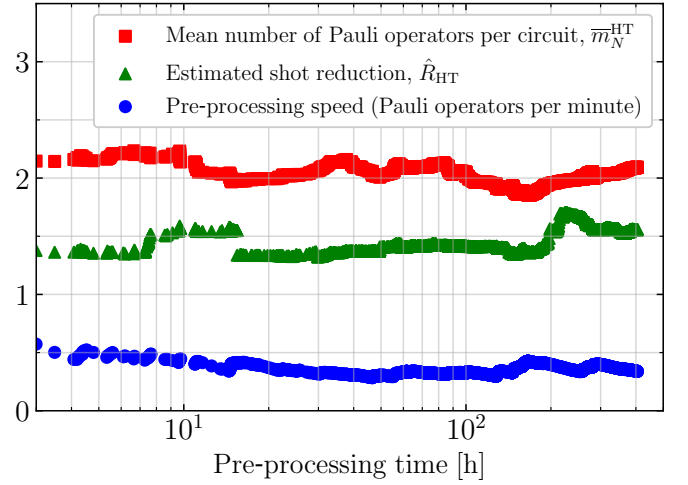


FIG. 14. Performance of Algorithm 2 when being applied to the list of 70,579 Pauli operators from Fig. 13 with $m_i = 1$. We use the algebraic solver with a cutoff of 5 from Sec. II C and tailor the readout circuits to a 2D square-lattice connectivity, taking up to $s_{\text{max}} = 5000$ subgraphs into account (here: not in parallel). All computations were carried out on an 18 core Intel Xeon CPU E5-2697 v4 @2.30GHz device.

important insight from Fig. 14 is that the performance of Algorithm 2 stays stable over long time periods. Even if this performance would suddenly deteriorate, one could simply terminate Algorithm 2 at any time and decide to individually measure the remaining Pauli operators in their respective TPBs. Next, we show that for performances as in Fig. 14, it is cost effective to execute Algorithm 2.

For a given observable $O = \sum_{i=1}^M c_i P_i$, the runtime that is saved on the quantum computer through the availability of a HT Pauli grouping of any *subset* of the set $\{P_1, \dots, P_M\}$ can be assessed as

$$T_{\text{saved}} = T_{\text{shot}} \times N_{\text{saved shots/est.}} \times N_{\text{est.}}, \quad (91)$$

where T_{shot} is the time needed for the execution of a single quantum circuit (“1 shot”), $N_{\text{est.}}$ is the number of experimental trial states ρ for which the expectation value $\text{Tr}[O\rho]$ is estimated, and $N_{\text{saved shots/est.}}$ denotes the number of quantum circuit executions that can be avoided (whilst maintaining a given accuracy) for such an estimation if the grouped Pauli operators are measured with HT readout circuits instead of TPBs. On current IBM quantum processors, the duration of a two-qubit gate is on the order of 500 ns, see Tab. XII in Sec. X. If the ansatz quantum circuit for the preparation of ρ relies on the implementation of gates of the form $\exp(icP)$ with $c \in \mathbb{R}$, $P \in \{I, X, Y, Z\}^{\otimes n}$ as in Sec. III, the required number of two-qubit gate layers (circuit depth) can be well above 100. In this case we find

$$T_{\text{shot}} > 50 \mu\text{s}, \quad (92)$$

which is within the window of coherence times reported in Tab. XII. Assume that we have grouped the first $M' < M$

Pauli operators into jointly-HT-measurable subsets. The estimated relative number of saved shots (assumed to be allocated optimally, see Sec. IV) for measuring the partial observable $O' = \sum_{i=1}^{M'} c_i P_i$ with HT readout circuits instead of TPBs is given by $\hat{R}'_{\text{HT}}/\hat{R}'_{\text{TPB}}$ [9]. Hence, the total number of shots saved per estimation of $\text{Tr}[O'\rho]$ follows as

$$N_{\text{saved shots/est.}} = \left(1 - \hat{R}'_{\text{TPB}}/\hat{R}'_{\text{HT}}\right) N'_{\text{alloc.shots}}, \quad (93)$$

where $N'_{\text{alloc.shots}}$ denotes the number of shots that we would have allocated to the measurement of $P_1, \dots, P_{M'}$ in a TPB approach. The number of iterations that are needed before the variational quantum eigensolver (VQE) algorithm starts to converge can be on the order of $N_{\text{conv.}} = 100$ [4]. By running the VQE algorithm once for each of N_{pos} positions of the nuclei of a molecule, one can map out its dissociation curve without the need to reconstruct any HT readout circuits, see Sec. VII. This can be repeated for the first N_{bands} excited states, still exploiting the same HT readout circuits. Finally, one might want to compare the results for $N_{\text{ansätze}}$ differently parameterized ansatz circuit architectures. Assuming $N_{\text{pos.}} = 100$, $N_{\text{bands}} = 10$, and $N_{\text{ansätze}} = 10$, the number of different states ρ for which $\text{Tr}[O\rho]$ needs to be estimated in such a scenario is given by

$$N_{\text{est.}} = N_{\text{conv.}} \times N_{\text{pos.}} \times N_{\text{bands}} \times N_{\text{ansätze}} \quad (94)$$

$$= 1,000,000.$$

Other use cases that require an enormously large number $N_{\text{est.}}$ of estimations include the simulation of quantum dynamics, where $\text{Tr}[O\rho(t)]$ is mapped out for a time-series of quantum states $\rho(t)$, as well as simulations of chemical reactions.

Let us derive an estimate of how large $N_{\text{est.}}$ needs to be before the construction of the 3935 HT readout circuits for the $M' = 8231$ Pauli operators from Fig. 14 pays off. For concreteness, we assume $N'_{\text{alloc.shots}} = 823,100$, i.e., every Pauli expectation value is estimated with an average number of 100 shots. Inserting this together with $\hat{R}'_{\text{HT}} = 1.56$ and $\hat{R}'_{\text{TPB}} = 1$ into Eq. (93) yields

$$N_{\text{saved shots/est.}} \approx 300,000. \quad (95)$$

Combining this with Eq. (92) shows that we would save about 1.5 seconds for every state ρ for which we estimate $\text{Tr}[O\rho]$. On the other hand, the pre-processing time needed on the classical computer for constructing the HT circuits was slightly less than $T_{\text{proc.}} = 1.5 \times 10^6$ seconds. In the extensive scenario described in Eq. (94), we would thus save as much time on the quantum computer (neglecting times waiting in the queue before the quantum circuits are executed) as we need to invest on the classical computer (in principle, in parallel). However, time is not the only resource that should be taken into consideration. Accessing one of IBM's 27-qubit Falcon R5 quantum processors is commercially available for

\$1.60 per runtime second. In view of the modest current CPU hourly rates of about \$0.10, the construction of HT readout circuits already pays off (in terms of money) after as little as $N_{\text{est.}} \approx 200$ usages. Again, let us stress the importance of the reusability potential of HT Pauli groupings, recall Sec. VII.

While this side-by-side comparison already demonstrates the financial viability of our method in its current form, we expect that upcoming theoretical improvements will further enhance the advantage of HT readout circuits over TPBs in the future.

IX. ANTICIPATED USE CASES

In this section, we discuss near-term applications for our hardware-tailored (HT) Pauli groupings that are promising, even in the presence of noise. An important example of a quantum algorithm that will likely benefit from HT readout circuits is the variational quantum eigensolver (VQE) algorithm, whose goal is computing the ground state energy $E_0 = \langle \Psi_0 | O | \Psi_0 \rangle$ of a quantum system with Hamiltonian O [1]. This is attempted by preparing a parameterized trial state $|\psi(\theta)\rangle$, and updating the parameters θ until $\langle O \rangle_{\theta} = \langle \psi(\theta) | O | \psi(\theta) \rangle$ is minimized. The information about how θ should be updated is obtained from measuring $\langle O \rangle_{\theta}$ (or its gradient). To reduce the sampling overhead, one can group the set $\{P_1, \dots, P_M\}$ of Pauli operators occurring in O (or its gradient) into jointly-measurable subsets. Here, one has three choices:

- Group $\{P_1, \dots, P_M\}$ into general commuting (GC) subsets using Sorted Insertion (SI) [9].
- Group $\{P_1, \dots, P_M\}$ into qubit-wise commuting (QWC) subsets using SI-QWC.
- Group $\{P_1, \dots, P_M\}$ into jointly-HT-measurable subsets using Algorithm 1 or Algorithm 2.

Each option has its up- and downsides that determine which one should be used under which circumstances. While GC groupings have the advantage of optimal estimated shot reductions \hat{R} , they have the disadvantage of unconstrained readout circuits. For QWC groupings, the situation is reversed: they feature extremely simple readout circuits but have the drawback of much smaller values of \hat{R} than for GC groupings. Finally, HT groupings interpolate between these two cases, at the expense of a higher pre-processing cost (which can be a worthwhile investment, see Sec. VIII).

An optimistic long-term vision is that fully-fledged quantum error correction will eventually render the cost of (logical) linear-depth Clifford circuits negligible, including potentially required (logical) SWAP-gates. Once such a stage is reached, GC groupings would be the optimal choice. At present and in the foreseeable future, however, it is crucial to keep quantum circuits short, which only leaves QWC and HT groupings as options.

In Fig. 3 of the main text, we compare the performance of (QWC) tensor product bases (TPBs) and HT readout circuits for a proof-of-principle experiment. In the plot, we identify two important regions: the low-shot (or high-error) regime and the high-shot (or low-error) regime. While HT circuits outperform TPBs in the low-shot regime, the opposite is true in the high-shot regime. This crossover is due to the bias (noise floor) being larger for HT than for TPB. Here, a few comments are in order: the difference between the two noise floors stems from the CZ-gates (at most 4, see Tab. IX in Sec. X) in the HT readout circuits. This difference is only visible because we measure a *separable* state for which preparation errors have a very small impact on the noise floor. For practical applications, one needs to prepare highly *entangled* quantum states using hundreds of two-qubit gates. In such a case, we expect that the noise stemming from the few extra gates in the readout circuits can be neglected (also note that one can fully control the number and instances of two-qubit gates that are allowed in the HT readout circuits), and we would recommend the use of HT readout circuits over TPBs.

Nevertheless, let us also discuss a VQE scenario where ultimate precision is needed, i.e., not a single two-qubit gate is permitted in any of the readout circuits with which the ground state energy is estimated. Even in this case, one can train the VQE using HT readout circuits and, after the VQE has converged, one can still switch to TPBs (with no two-qubit gates) to slightly improve the final energy estimate. Here, it is important to note that the bias is negligible in the low-shot regime because sampling errors dominate, which is demonstrated by the perfect agreement (in this regime) of the experimental data with the noiseless simulations in Fig. 3 of the main text.

Finally, let us mention that the bias due to noisy CZ-gates in the HT readout circuits could be potentially reduced by adapting common error mitigation techniques [69–71]. We leave this as an open problem.

X. DETAILS ABOUT THE EXPERIMENT

In the main text, we report on an experiment in which hardware-tailored (HT) readout circuits outperform conventional tensor product bases (TPBs) measurements. Here, we provide more information about the experiment.

We start by constructing an eight-qubit molecular Hamiltonian O representing four hydrogen atoms on a linear chain with equal interatomic distances of $\Delta = 1.0 \text{ \AA}$. Then, we harness the SI-QWC algorithm [9] to group the $M = 184$ operators in the Pauli decomposition of O into $N_{\text{TPB}} = 35$ TPBs (see Tab. VII). As expected, the number of operators in the different TPBs is far from uniformly distributed [4, 6, 7]. This is undesirable because it leads to suboptimal shot reductions. The uneven distribution is due to Pauli operators with a low weight (number of non-identity tensor factors) running

out first during the execution of the SI-QWC algorithm, which results in increasingly smaller TPBs, e.g., the last five TPBs only contain a single Pauli operator. For larger Hamiltonians, these effects are even stronger, see Fig. 13 in Sec. VIII.

In theory, general commuting (GC) Pauli groupings would solve this problem. Applying the Sorted Insertion algorithm [9] to O results in only $N_{\text{GC}} = 9$ GC collections (see Tab. VIII). Note that GC collection 1 and 2 coincide with TPB 1 ($Z^{\otimes 8}$) and 2 [$(Z \otimes X)^{\otimes 4}$] from Tab. VII. The other GC collections, however, contain pairs of Pauli operators that are not qubit-wise commuting. Their corresponding GC readout circuits contain a substantial amount of two-qubit gates and require a large SWAP-gate overhead on a linear hardware connectivity (see Tab. VIII). As an illustrative example, we depict the readout circuit of the third GC collection in Fig. 15.

Finally, we compute a HT Pauli grouping by applying Algorithm 1 from Sec. V (see Tab. IX for the resulting HT collections and their diagonalization circuits). The result is impressive: compared to TPBs, the number of required readout circuits is reduced by a factor of 3.5, at a moderate increase in the average number of CZ-gates from zero to two. Compared to GC circuits, the average number of two-qubit gates is reduced by a factor of 13 and we avoid all 411 SWAP-gates, at a moderate increase from $N_{\text{GC}} = 9$ to $N_{\text{HT}} = 10$. Thus, even for trapped-ion quantum computers which feature all-to-all connectivity our HT Pauli groupings offer advantages over GC Pauli groupings.

Note that all three Pauli groupings start with $Z^{\otimes 8}$ and $(Z \otimes X)^{\otimes 4}$. In particular, we have $O_1^{\text{TPB}} = O_1^{\text{HT}}$ and $O_2^{\text{TPB}} = O_2^{\text{HT}}$ [recall Eq. (68)]. Since it is the purpose of our experiment to unveil the performance differences between TPBs and HT readout circuits, we consider a hypothetical scenario, where $\langle O_1 \rangle$ and $\langle O_2 \rangle$ are already determined. Thus, we only concern ourselves with experimentally measuring the expectation value of the observable

$$O' = \sum_{i=3}^{35} O_i^{\text{TPB}} = \sum_{i=3}^{10} O_i^{\text{HT}}, \quad (96)$$

which only contains the $M' = 124$ Pauli operators that are distributed differently for TPB and HT. For O' , the estimated shot reductions over individual Pauli measurements (IPMs) are given by $\hat{R}_{\text{TPB}} \approx 3.52$, $\hat{R}_{\text{GC}} \approx 14.41$, and $\hat{R}_{\text{HT}} \approx 12.90$ [recall Eq. (67)]. The effective shot reductions, however, depend on the measured state. For simplicity, we initialize each of the $n = 8$ qubits in a random state by applying a gate of the form

$$U_3(\theta, \phi, \lambda) = \begin{pmatrix} \cos\left(\frac{\theta}{2}\right) & -e^{i\lambda} \sin\left(\frac{\theta}{2}\right) \\ e^{i\phi} \sin\left(\frac{\theta}{2}\right) & e^{i(\phi+\lambda)} \cos\left(\frac{\theta}{2}\right) \end{pmatrix}. \quad (97)$$

For $|\psi\rangle = \bigotimes_{j=1}^8 U_3(\theta_j, \phi_j, \lambda_j) |0\rangle$ (see Tab. X) and O' , the state-dependent shot savings over IPMs are in good agreement with \hat{R} , and they are given by $R_{\text{TPB}} \approx 3.62$,

$R_{\text{GC}} \approx 16.23$, and $R_{\text{HT}} \approx 14.54$ [9]. Note that these theoretical shot savings assume optimal shot allocations (see Tab. XI) and ideal operations.

Now, we report how the experimental data in Fig. 3 of the main text is obtained. We first prepare eight linearly connected qubits on the superconducting quantum processor *imbq_washington* (see Tab. XII for the device specifications) in the state $|\psi\rangle$, then we execute one of the diagonalization circuits, and finally we read out all qubits in the computational basis. For each measurement basis in Eq. (96) (33 TPBs and 7 HT bases), we collect the measurement data from 10 million (10M) circuit executions. After applying readout error mitigation [70], the prevalent errors in the processed measurement results are likely due to imperfect gate operations in the diagonalization circuits. For a given shot budget N^{shots} , we compute the error $\epsilon = |E'_{\text{exp}}(N^{\text{shots}}) - E'_{\text{theo}}|$, where $E' = \langle \psi | O' | \psi \rangle$ is the partial energy. Hereby, we split a total amount of 50M shots into $\lfloor 50\text{M}/N^{\text{shots}} \rfloor$ subsets, where the ratios in Tab. XI are obeyed. For small values of N^{shot} , the number of repetitions is so large that the

error on the mean of ϵ becomes negligible.

Finally, let us point out an important technical detail. Any diagonalization circuits for a list of Pauli operators $P_1, \dots, P_m \in \{I, X, Y, Z\}^{\otimes n}$ brings each P_i into the form $\pm Z^{\mathbf{k}_i}$ for some $\mathbf{k}_i \in \mathbb{F}_2^n$. For a correct interpretation of the measurement results it is crucial to know the correct sign of $\pm Z^{\mathbf{k}_i}$; it can be reconstructed from P_1, \dots, P_m via the prefactor map $\alpha : \mathbb{F}_2^{2n} \rightarrow \mathbb{Z}/4\mathbb{Z} = \{0, 1, 2, 3\}$ for the layer of single-qubit Clifford gates represented by $A \in GL(\mathbb{F}_2^{2n})$, which arises as

$$\alpha(\mathbf{r}, \mathbf{s}) = \sum_{j=1}^n \alpha_j(r_j, s_j) \quad (98)$$

from the single-qubit prefactor maps $\alpha_j : \mathbb{F}_2^2 \rightarrow \mathbb{Z}/4\mathbb{Z}$, represented by $A_j \in GL(\mathbb{F}_2^2)$ (see main text, Tab. I). Note that $\alpha_j(1, 1) = \alpha_j(1, 0) + \alpha_j(0, 1) + 2a_j^{xz}a_j^{zx}$. For the HT circuits used in this experiment, we provide the signs in Tab. IX.

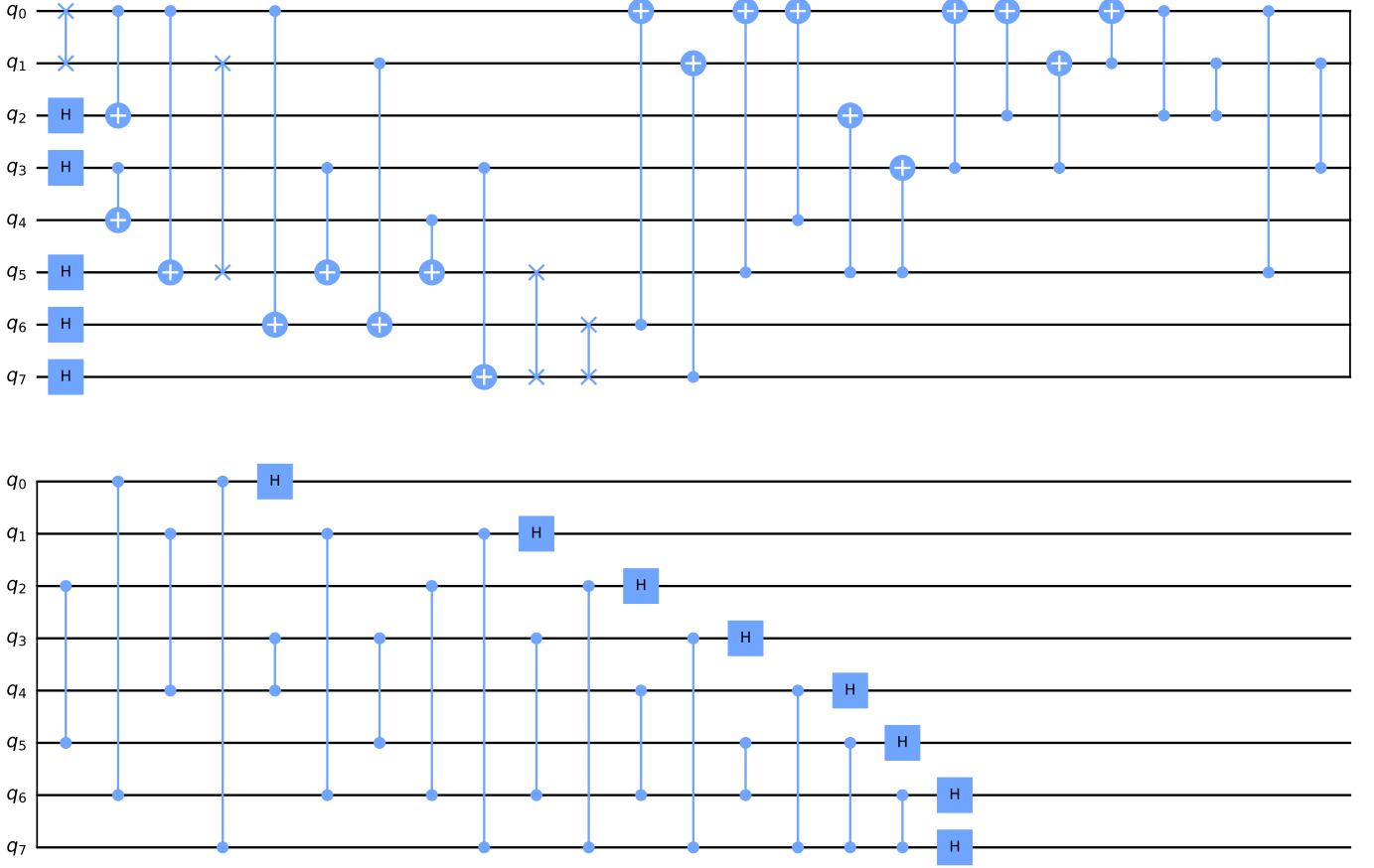


FIG. 15. GC readout circuit no. 3, which diagonalizes $IXXIIXXI$, $IYYZIXXI$, $IXXIYYZ$, $IYYZIIYYZ$, $ZIXXIIXX$, $IZYYZIXX$, $IZYYIZYY$, $ZIXXZZYY$, $IZYYIXXI$, $ZIXXZXXI$, $IZYYIYYZ$, $ZIXXZYYZ$, $IXXIIZIXX$, $IYYZZIXX$, $IXXIIZYY$, $IYYZIZYY$, $IYZYIIII$, $ZYZYZIII$, $IIIIYZZY$, and $IIIIZYZY$ [6]. After being transpiled to a linear connectivity, this circuit contains 13 Hadamard-, 18 CNOT-, 21 CPHASE-, and 66 SWAP-gates.

TABLE VIII. Pauli grouping of the H_4 -Hamiltonian from Tab. VII into nine general commuting (GC) collections. In accordance with Eq. (68), the first Pauli operator and the total number of operators in collection i are denoted by $P_{i,1}$ and m_i , respectively. For every GC collection, we compute a readout circuit (see Fig. 15 for an example) using the algorithm provided in Ref. [6] in combination with Sec. I. Then, we use Qiskit to transpile the GC circuits to a linear connectivity by introducing SWAP-gates [36]. The final number of two-qubit gates and SWAP-gates in the transpiled circuits is presented.

i	$P_{i,1}$	m_i	#CNOT + #CPHASE	#SWAP
1	$ZZZIZIII$	36	0	0
2	$IXIIIXII$	24	0	0
3	$IXXIIXXI$	20	39	66
4	$IYYXIYYX$	24	32	54
5	$IIXIIIII$	16	27	45
6	$IXXIIXII$	16	34	59
7	$IXIIIXXI$	16	31	55
8	$ZIXZIZZI$	16	45	78
9	$IYYXZZZI$	16	34	54

TABLE IX. Nine of the $N_{\text{HT}} = 10$ hardware-tailored (HT) diagonalization circuits for the H_4 -Hamiltonian from Tab. VII. For visual reasons, we do not depict the trivial circuit which “diagonalizes” the TPB $Z^{\otimes 8}$. The circuits are tailored to a linear connectivity. Note that only 4 different circuit templates are selected by Algorithm 1, even though we considered the exhaustive list of all 128 subgraphs of the 8-vertex path graph. Thus, it might be possible to analytically construct HT diagonalization circuits for certain types of Hamiltonians.

[illegible]

TABLE X. Random choice of parameters $\theta_j, \phi_j, \lambda_j \in [0, 2\pi]$. This defines the state $|\psi\rangle = \bigotimes_{j=1}^8 U_3(\theta_j, \phi_j, \lambda_j) |0\rangle$ that is prepared and measured in our experiment.

j	1	2	3	4	5	6	7	8
θ_j	1.203	4.935	1.737	5.504	4.294	3.526	4.856	3.867
ϕ_j	3.909	4.901	5.038	2.248	4.478	3.161	5.546	0.474
λ_j	2.750	1.713	6.020	3.148	2.326	0.087	2.293	2.317

TABLE XI. Optimal shot-allocation ratios for Pauli groupings of \mathcal{O}' as defined in Eq. (96) into TPBs (Tab. VII), GC (Tab. VIII), and HT collections (Tab. IX). The variances $\text{Var}[O_i] = \langle \psi | O_i^2 | \psi \rangle - \langle \psi | O_i | \psi \rangle^2$ that enter Eq. (61) are computed for the target state $|\psi\rangle$ defined in Tab. X.

Collection	TPB	GC	HT
3	0.05740	0.17765	0.16813
4	0.03694	0.16239	0.15369
5	0.05806	0.14073	0.13834
6	0.03158	0.14689	0.13081
7	0.02765	0.15326	0.10295
8	0.02534	0.10598	0.09936
9	0.02721	0.11309	0.10090
10	0.02481		0.10583
11	0.05838		
12	0.04098		
13	0.03062		
14	0.04453		
15	0.03192		
16	0.03092		
17	0.03098		
18	0.03897		
19	0.03895		
20	0.02919		
21	0.03589		
22	0.02233		
23	0.02746		
24	0.03038		
25	0.03441		
26	0.03543		
27	0.02051		
28	0.02051		
29	0.01994		
30	0.01994		
31	0.01218		
32	0.01210		
33	0.01782		
34	0.01305		
35	0.01360		

TABLE XII. Device specification of the 127-qubit quantum processor *ibm_washington*. The experiment was carried out on a linear chain of eight qubits (42, 43, 44, 45, 54, 64, 63, and 62). For every qubit, we provide the relaxation time T_1 , coherence time T_2 , error rates of the \sqrt{X} -gate, and the readout error probability $P(m|p)$ for preparing $|p\rangle$ but measuring $|m\rangle$. Note that every single-qubit gate is a sequence of \sqrt{X} -gates and virtual z -rotations, which have a duration of 36 ns and 0 ns, respectively [42]. Readout pulses have a duration of 864 ns. Finally, we provide the error rate and duration of a CNOT-gate with control qubit i and target qubit j , where $(i, j) \in \{(42, 43), (43, 44), (44, 45), (45, 54), (54, 64), (64, 63), (63, 62)\}$.

Qubit	T_1 [μ s]	T_2 [μ s]	$P(0 1)$	$P(1 0)$	\sqrt{X} -gate error	CNOT-gate error	CNOT-gate duration [ns]
42	108.62	255.06	0.012	0.009	0.000139	0.014673	804
43	128.82	195.74	0.025	0.025	0.000299	0.012446	427
44	89.34	123.60	0.019	0.015	0.000299	0.014925	1074
45	107.16	158.24	0.042	0.025	0.000215	0.033060	597
54	111.27	117.25	0.015	0.010	0.000265	0.009645	377
64	99.75	90.05	0.011	0.012	0.000345	0.014083	405
63	83.30	174.79	0.013	0.004	0.000663	0.011548	548
62	81.93	142.67	0.052	0.007	0.000180		